ABSTRACT

Title of Thesis: DESIGN AND HIERARCHICAL ASSEMBLY OF AMPHIPHILIC SUPRACOLLOIDS THAT MIMIC BIMOLECULAR COMPOUNDS

Shaoyi Zhang, Doctor of Philosophy, 2018

Thesis Directed By: Professor Zhihong Nie,
Department of Chemistry and Biochemistry

Self-assembly of nanoparticles (NPs) into desired structures with precisely controlled NP organization is crucial to the property discovery and application of inorganic NPs. Despite tremendous efforts made in the past decades, little progress has been achieved in controlled hierarchical assembly of NPs. My dissertation is focused on the multi-level assembly of inorganic NPs into various hierarchical structures by tethering NPs with functional block copolymers (BCPs).

First, one versatile strategy was developed to design monodisperse amphiphilic supracolloids with defined valence and chemical patches by co-assembly of binary disparate hybrid building blocks composed of BCP-functionalized NPs. The binary BCP is composed of a hydrophilic/hydrophobic block and a Lewis base-containing/Lewis acid-containing block. The resulting supracolloids consist of two different types of inorganic NPs precisely arranged in space, which mimics the geometric shape and valence of bimolecular compounds containing two elements. By varying the size, chemical composition and feeding ratio of NPs, as well as the length of BCP

combinations, supracolloids with different valences, compositions and localized chemical patches (which are determined by the BCP tethers) were produced in high yield.

Second, the amphiphilic supracolloids were demonstrated to assemble into a range of two-dimensional (2D) hierarchical structures at the liquid/liquid interface. Depending on the quality of solvent, amphiphilic dimers were found to assemble into petal-like structures with different numbers of dimers. Moreover, amphiphilic trimers underwent side-by-side or end-to-end association to form ribbon or chain structures, depending on the arrangement of hydrophilic and hydrophobic domains (chemical patches).

Third, the effect of polymer length of BCP tethers within supracolloids was systematically studied on the ribbon formation of trimer-like supracolloids with hydrophobic center and hydrophilic ends. It was found that longer hydrophobic block and shorter hydrophilic BCP tethers facilitate the formation of ribbon. The results were summarized in a product diagram.

Finally, the pH effect on the assembly of amphiphilic supracolloidal trimers was investigated. A transition of assembly morphologies from ribbons to chains was observed, with changing pH of the water phase. This can be attributed to the change on the amphiphilicity of supracolloidal trimers upon the addition of acid or base.

DESIGN AND HIERARCHICAL ASSEMBLY OF AMPHIPHILIC SUPRACOLLOIDS THAT MIMIC BIMOLECULAR COMPOUNDS

by

Shaoyi Zhang

Thesis submitted to the Faculty of the Graduate School of the
University of Maryland, College Park, in partial fulfillment
of the requirements for the degree of
Doctor of Philosophy
2018

Advisory Committee:
Professor Zhihong Nie, Chair
Prof. Bryan Eichhorn
Prof. Sang Bok Lee
Prof. Efrain Rodriguez
Prof. Robert M. Briber, Dean's representative

Dedication

To my parents and my husband, thanks for always be my support, and I will always be there for you, too.

Acknowledgements

This work presents the record for the last six years I spent in this beautiful university. It will be always in a significant position in my memory, not only because this is the best academic achievement so far that I am truly proud of, but also because I always feel gratitude for the love and support I experienced during the whole process.

Firstly, I would like to express my sincere gratitude to my advisor Prof. Zhihong Nie, who interviewed me and positively commented me when I applied University of Maryland, so I could have the chance to step into this wonderful university; who also encouraged me and totally trusted me when I failed again and again and even wanted to give up the research; who always respect me and patiently guide my research and career in the way that I feel most supportive. I could not image how to finish all work without my awesome mentor.

Besides my advisor, I would like to thank the rest of my thesis committee: Prof. Bryan Eichhorn, Prof. Sang Bok Lee, Prof. Efrain Rodriguez and Prof. Robert M. Briber, for their perceptive comment and generous support, and for their questions that inspire me to understand the project from a wider viewpoint.

I also want to thank all the group members in Prof. Nie's group. My sincere thanks goes to my senior partner Dr. Chenglin Yi in this project, without whom I can never go this far. We worked together to make progress on this project, he is the one knows the best how difficult it is to overcome the hundreds of problems, and how valuable our insistence is so that we can finally work out some amazing results. I would like to thank Dr. Yang Yang, who not only mentored me in the research, but

also cares me like a big sister. My thanks goes to Dr. Maria Teresa Perez-Cardenas, who is like an angle always warms my heart, and keep reminding me that I want to become a brave and caring woman just like her. My thanks also goes to Prof. Jie He, the formal post doc in our group, who always patiently answer my (sometimes silly) questions. I would like to sincerely thank Marcus Carter, Kuikun Yang, Hongyu Guo, and Xiaoying Lin, Qian Zhang, Kyle Thomas Webb and all the rest labmates. Having friends like them in the lab, doing research becomes even more joyful.

Last but not least, I would like to thank my family, my dear husband Yixiu Wang, who always knows me, respects me, supports me, loves me and brings happiness to my life like sunshine every single day. Maybe I've said it too much, but it's my greatest pleasure to spend every day in the rest of my life with you together. I also want to thank my parents, especially my mom, who came to this country where people speak a language she doesn't know, just to support me in my defense; who doesn't understand at all what my project is but always think it's the greatest work in the world. And I thank God every day for every beautiful thing I have and every difficulty I experienced and overcame in my life.

Table of Contents

List of Tables

List of Figures

List of Abbreviations

1D	One dimensional
2D	Two dimensional
3D	Three dimensional
AAO	Anodic aluminum oxide
AC	Alternating current
$AgNO_3$	Silver nitrate
AIBN	Azobis(isobutyronitrile)
BCPs	Block copolymers
CG	Coarse-grained
CH_2Cl_2	Dichloromethane
CNT	Carbon nanotube
CPPA	4-cyano-4-(phenylcarbonothioylthio) pentanoic acid
CTAB	Hexadecyltrimethylammonium bromide
DC	Direct current
DEG	Diethyleneglycol
DLS	Dynamic Light Scattering
DMAET	2-(dimethylamino)ethanethiol hydrochloride
DMF	N,N-Dimethylformamide
DPD	Dissipative particle dynamics
DTAB	Dodecyltrimethylammonium bromide
$FeCl_3 \cdot 6H_2O$	Iron(III) chloride hexahydrate
GPC	Gel Permeation Chromatography
$HAuCl_4$	Gold (III) chloride trihydrate

HOPG Highly oriented pyrolytic graphite

LB Langmuir-Blodgett

LSPR Localized surface plasmon resonance

NaOL Sodium oleate

NBB Nanoscale Building Block

NCs Nanocubes

NPs Nanoparticles

NRs Nanorods

NSs Nanospheres

NWs Nanowires

ODPA Octadecylphosphonic acid

PDMS Polydimethylsiloxane

PDP 3-n-pentadecylphenol

PEP Poly(ethylene propylene)

PEO Poly(ethylene oxide)

PEO-b-P(DMAEMA-r-St)-SH

Poly(ethylene oxide)-*block*-poly(N, N-dimethylaminoethyl methacrylate-*r*-styrene)

PEP Poly(ethylene propylene)

PMMA Poly(methyl methacrylate)

PS-b-P(AA-r-St)-SH

Polystyrene-*block*-poly(acrylic acid-r-styrene)

PVP Poly(vinylpyrrolidone)

P2VP Poly-2-vinylpyridine

P4VP	Poly(4-vinylpyridine)
RAFT	Reversible addition-fragmentation chain transfer
SEM	Scanning electron microscope
SERS	Surface-enhanced Raman scattering
TEM	Transmission electron microscope
THF	Tetrahydrofuran
TGA	Thermogravimetric Analysis
TOPO	Trioctylphosphine oxide

Chapter 1: Introduction

Part of this chapter is adapted from the manuscript published in the following book: Functional Organic and Hybrid Nanostructured Materials: Fabrication, Properties and Applications; chapter 1: Zhang, S.; Yang, Y.; Nie, Z., Controllable Self-Assembly of One-Dimensional Nanocrystals, Wiley publishing, 2018; and the article: Yi, C.; Zhang, S.; Webb, T. K.; Nie, Z., Anisotropic Self-Assembly of Hairy Inorganic Nanoparticles, *Acc. Chem. Res.*, **2017**, 50, 12–21.

In the past decades, controlled assembly of nanoscale building blocks (NBBs) has continuously been a prevailing topic. The tremendous interest in organizing NBBs is mainly stemmed from the potential applications of NBBs in diverse areas, including chemical and biological sensing, energy storage and production, and optoelectronic devices.[1] For instance, the strong shifted absorption peak in the optical spectrum brought about by the close interactions between metallic NPs is very robust, and can be used in plasmon rulers, localized surface plasmon resonance (LSPR) sensors, surface-enhanced Raman scattering (SERS) sensing, etc.[2] In addition, recent advances at this frontier are also partially driven by the rapid development in the synthesis of relatively monodisperse NBB with controlled size, shape and composition.[3] Recently, various methods have been developed for the organization of NBBs into functional structures. In particular, bottom-up self-assembly approach offers a more robust, scalable and cost-effective way to fabricate arrays of NBBs in a controlled manner, compared with top-down techniques such as electron-beam and focused-ion beam lithography.[4] In this chapter, we classified current self-assembly methods into four major categories, namely, templated assembly, field-driven assembly, assembly at interfaces and ligand-guided assembly.

1.1 Templated Assembly

Templated assembly, fittingly, is the assembly directed by a predesigned template, which governs the anchoring of NBBs on (or within) the template. As a straightforward method, the geometry and patterning of templates or the distribution of functional groups on templates dictates the location, orientation, or alignment of NBBs as well as the association state of NBBs. Typically, the templating effect arises from physical confinement of the template, differential affinity of NBBs towards template surface, or chemical bonding between ligands on NBBs and templates. Recent progress at this frontier has allowed one to assemble NBBs in various dimensions into long-range ordered structures with high yield, and to obtain well-defined orientation of NBBs at single particle resolution. This largely fulfills the requirement of assemblies on substrates for the applications including biosensors, optical devices, metamaterials, etc.[5] In this section, we discuss several categories of assembly systems, classified based on the characteristics of templates.

1.1.1 Geometrically patterned template

Assembly based on geometrically patterned template utilizes topographical patterns on a substrate to direct the interaction and shape selective organization of NBBs within the patterns. Representative topographical patterns include periodic polygonal grooves, discrete spherical poles, parallel channels, etc. These templates are usually fabricated by top-down approaches such as, photolithography, chemical vapor deposition, inkjet printing, and focused beam (electrons, ions, laser etc.) etching.[6] To achieve desired assembly structures of NBBs, the geometric parameters (e.g., size, depth and geometry of patterns) have to be carefully tuned. By using this

method, various types of assemblies have been produced, such as discrete clusters, one dimensional (1D) arrays, two dimensional (2D) monolayers, and three dimensional (3D) supercrystals.

Toward the end of last century, Blaaderen *et al.* reported the crystallization of bulk colloidal crystals through slow sedimentation of silica spheres onto a pole-patterned poly(methyl methacrylate) (PMMA) layer.[7] Xia et al. fabricated a series complex aggregates of polystyrene (PS) beads including polygonal or polyhedral clusters, linear or zigzag chains and circular rings by combing physical tempalting and capillary forces.[8] Thanks to the development on pattern design, great progress has been achieved in fabricating diverse arrays of NBBs on patterned substrate with high yield, good scalability and superior morphology control.[9] Recently, Brugger *et al.* realized the capillary assembly of Au nanorods (NRs) into large-area ordered structures on substrates with predetermined surface patterns.[10] In this work, the precise control over the organization of Au NRs on the substrate was accomplished by subtlety design the geometry of traps. As shown in Figure 1.1, funneled traps with auxiliary sidewalls were fabricated to effectively prevent the removal of NRs after insertion into traps. With the introduction of the sidewalls, the assembly yield goes up to 100%. The positional control of Au NRs goes down to nanometer scale. As shown in Figure 1.1b, Au NRs can be selectively placed onto substrate with arbitrary patterns by using this method.

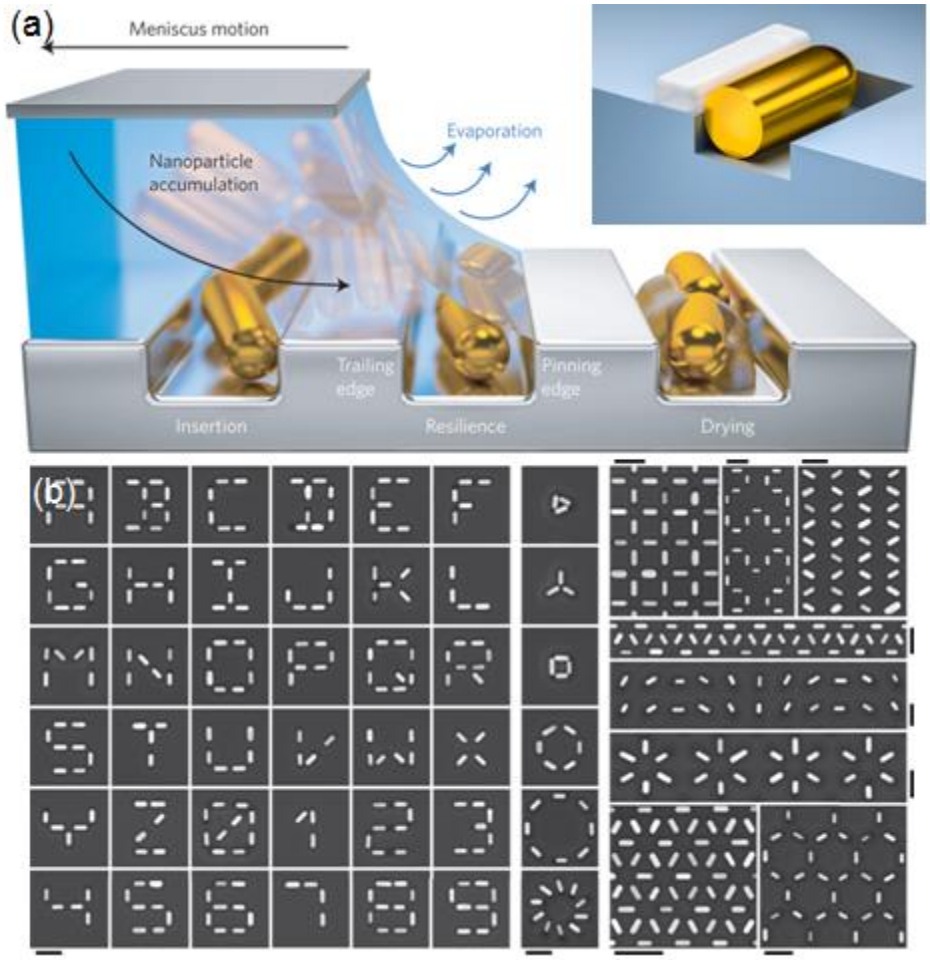

Figure 1.1 Assembly of Au NRs on patterned solid substrate. (a) Scheme of capillary assembly of Au NRs onto substrates with geometrical patterns. (b) SEM images of Au NRs patterns by topographically template capillary assembly. Scale bar: 250 nm. (Adapted with permission.[10] Copyright 2016, Nature publishing Group.)

Apart from directly modulating patterns on a substrate, confinement can be used to control the organization of NBBs. Typically, a suspension of NBBs is confined between a topologically patterned template at the top and a smooth substrate at the bottom. The subsequent evaporation of solvent in a controlled manner drives the formation of orientated array of NBBs. The above templates function as both

regulating the solvent evaporation and controlling the deposition of NBBs at given locations on the substrate. Typical templates such as elastomeric polydimethylsiloxane (PDMS) stamp and highly oriented pyrolytic graphite (HOPG) have been employed to provide confinement effect to facilitate the formation of closely packed arrays of NBBs.[11] In this case, the templates can be easily removed and recycled, while the assemblies are left on flat substrates. As an example, Ahmed *et al.* reported the formation of perpendicular superlattices of hexagonally oriented CdS NRs using HOPG template.[12] A dispersion of CdS NRs in toluene was trapped between a block of HOPG and a smooth silicon wafer. Upon the slow evaporation of solvent, a large-area (~2 μm^2) monolayer of perpendicularly oriented NRs was formed on the substrate. Another practical confinement comes from the porous membrane using anodic aluminum oxide (AAO) template. By functionalizing the walls, NBBs are able to anchor onto the walls via either chemically binding (such as covalent bond) or physically binding (such as electrostatic attraction). Rubinstein and co-workers fabricated the freestanding "nanoparticle nanotubes" by passing Au colloids solution through a silanized alumina membrane, followed by membrane dissolution with base solution.[13]

In addition to templates with defined shapes, fluid-like assemblies of liquid crystals can be used to guide the assembly of NBBs. Liquid crystal molecules are known to assemble into a range of liquid crystal phases such as nematic phase, smectic phase, chiral nematic or cholesteric phase, cubic blue phase. These phases can serve as "soft" scaffolds to organize NBBs into long-range ordered structures.[14] For example, Smalyukh and coworkers demonstrated the self-alignment of Au NRs in

the anisotropic fluids of liquid crystals.[15] Nematic and hexagonal liquid crystalline phases of a tertiary mixture composed of hexadecyltrimethylammonium bromide (CTAB), benzyl alcohol, and water were used to guide the alignment of Au NRs along the liquid crystal director. When a magnetic field or shearing force is applied, the orientation of Au NRs can be switched, owing to the realignment of liquid crystals under external field. This method allows for unidirectional alignment of NRs in liquid crystal matrix over large areas (up to millimeters), thus facilitating their applications as bulk optical metamaterials. Defects in liquid crystal superstructures can be also used to assemble NBBs, for example, the topological defect cores within the self-organized blue phase of 3D cubic nanostructures can provide natural templates to trap colloidal NBBs.[16] However, to date only few types of NPs have been assembled by using these 3D topological templates.[17]

The assembly strategy using geometrically patterned templates allows for the fabrication of large-area predetermined assembly structures with controlled geometric parameters. These assemblies of NBBs can be readily integrated in a device supported on a substrate and tailored for a broad range of applications in such as sensors and optoelectronics by designing the templates. To facilitate the interaction between template and NBBs, this method often requires the surface modification of NBBs with designed small or large molecules via such as ligand exchange.

1.1.2. Chemically patterned template

Chemically patterned templates such as carbon nanotube (CNT), polymer matrix and peptide nanostructures have been extensively explored for guiding the assembly of NBBs. In this method, the organization of NBBs is determined by the

spatial arrangement of chemical functional groups that have strong affinity towards NBBs. This approach enables one to control not only the position and orientation of NBBs with single-particle precision, but also the formation of NBB arrays in a three-dimensional space. Here we exclude assembly templated by DNA nanostructures in this section and leave this topic in the section of ligand-guided assembly.

In a simplest scenario, 1D nano- or micro-structures (e.g., CNT, nanofibers, etc.) can be used to template the linear organization of NBBs. For example, CNTs are attractive for templating the 1D ordering of NBBs due to their intrinsic mechanical, optical and electronic properties and intensively explored surface modification. An early example of CNT template self-assembly of Au NPs was reported by Fitzmaurice and coworkers, who obtained a close to monolayer coverage of 6 nm Au NPs absorbed at the surface of CNTs by mixing CNTs with tetraoctylammonium bromide stabilized Au NPs.[18] Later, CNTs were used to guide the assembly of NBBs with various shapes, the first example of CNT-templated assembly of Au NRs was reported by Liz-Marzan and coworkers.[19] In this work, Multiwall CNTs were wrapped with poly(styrenesulfonate), followed by depositing positively charged poly(diallyldimethyl)ammonium chloride on the surface of CNTs. Au NRs modified with negatively charged poly(vinylpyrrolidone) (PVP) were organized end-to-end into stripes on opposite sides of the CNTs, as a result of the electrostatic attraction between NRs and CNTs. The end-to-end organization of Au NRs was attributed to the anisotropic surface of NRs and a higher electric potential reduction at the NR tips with high curvature than that at the side of NRs. The organization of NRs is not necessary to be end-to-end to form simple chains, when the template possesses more

complex structures. As an interesting example, chiral ribbons assembled from peptide were used to template the side-by-side arrangement of Au NRs into single helices chiral arrays.[20] At the early stage of assembly, spherical NPs were bound to the outer face of the helical ribbon, the *in situ* one dimensional growth of NPs in the presence of peptide conjugates was limited by the width of the helical ribbon, leading to the formation of parallel array of rod-like particles.

Polymer matrix such as phase-separated BCP films presents a typical class of versatile organic template for the assembly of NBBs.[21] For assembly in homopolymer matrix, the dispersion and assembly of NBBs can be mediated by a series of parameters, such as volume content of NBBs, the type and length of ligands on NBBs, and the length and compatibility of matrix polymer.[22] With increasing complexity, the majority of these polymeric templates are fulfilled with BCPs that are capable of assembling into a rich variety of nanoscale morphologies in both solutions and films. By mixing NBBs with BCPs in appropriate ratio, NBBs can be selectively incorporated into one of the phase-segregated nanoscale domains, depending on the miscibility between the NBBs (or ligands on NBBs) and BCP block of the host phase. Generally, the spatial placement of NBBs can be realized by controlling the length and chemical moieties of each block of BCPs.[23] From the first example from Schrock and coworkers who demonstrate the generation of plasmonic NPs within lamellar or cylindrical microdomains of BCP as early as 1992,[24] a great variety of NBBs was anchored within the domains of BCPs with precise control over the particle localization and arrangement. In a classic example, Bockstaller *et al.* obtained autonomous separation and organization of binary nanocrystals within alternating

arrays in the matrix of BCPs, as shown in Figure 1.2.[25] In this work, aliphatic coated 3.5 nm Au NPs and 21.5 nm silica NPs were mixed with poly(styrene-*b*-ethylene propylene) (PS-PEP) solution. The film of BCP/particle mixture was obtained, where smaller Au NPs segregated to the intermaterial dividing surface between PS and PEP domains, and bigger silica NPs located at the center of PEP domains. The interfacial segregation of NPs is dependent on the relative size of NPs and respective domain dimensions. The sequestration of larger NPs dominants the reduction of conformational entropy of PEP subchains, and the small NPs translational entropy outweighs the decrease in entropy.

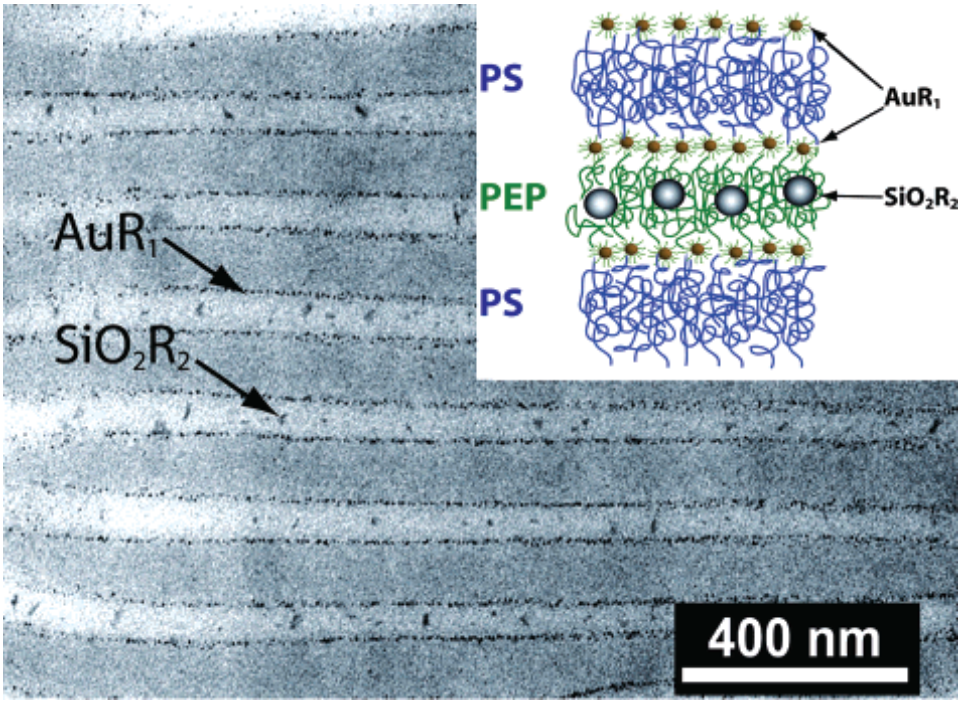

Figure 1.2 Bright field electron micrograph of a ternary BCP/Au NP/Si NP mixture with schematic illustration in the inset. (Adapted with permission.[25] Copyright 2003, American Chemical Society.)

Chemical patterns generated by pre-obtained phase-separated BCPs on a substrate can be used to selectively absorb and organize NBBs. In an early work by Russell and coworkers, PS-b-PMMA film with channels or pores on a silicon wafer was used as templates to guide the assembly of poly(ethylene oxide) (PEO) functionalized CdSe NRs.[26] The PEO ligand drove the CdSe NRs to migrate from solution to the water/air interface, facilitating the absorbing of NRs into the hydrophilic channels or poles of the BCP template. As a result, CdSe NRs were found to align along the channel walls or aggregated in the pores. Later, more advances have been achieved on manipulating the orientation and spacing of NRs by tuning the particle-template and/or particle-particle interactions.[27] For instance, Vaia *et al.* demonstrated the control over single and double-column arrangement of Au NRs with orientation parallel and perpendicular to template strips of poly-2-vinylpyridine (P2VP) regions on a substrate.[27d]

Compared with geometrically patterned templates, chemical patterns afford additional flexibility in guiding the assembly of NBBs, due to the selectivity in the interactions between NBBs and templates. Thus, this method enables one to control the spacing and orientation of NBBs. However, assembly using chemical patterns heavily relies on the chemical interactions between particles and templates. As a result, this method usually requires surface modification of NBBs and molecular design of template surface, and mostly these templates cannot be repeatedly used.

1.2 Field-driven Assembly

The intrinsic anisotropy in shape, dipole moment, and charge distribution of NBBs makes them readily to be aligned under external field (*e.g.*, electric, magnetic

field or fluidic shearing). The literature is burgeoning with research on the directed assembly of NBBs under external field. In this section, we review several types of field-driven assembly strategies, including electric or magnetic field-assisted assembly, and assembly in fluid flows.

1.2.1 Assembly under electric field

Electric field is an ideal external stimulus to drive the organization of NBBs that carry a net charge or permanent/induced electric dipole moment. Under electric field, NBBs with a net charge align their longitudinal axis along the direction of the field lines and migrate towards the electrode of applied electric field. When there is no net charge, the polarization of NBBs under electric field induces the dipole-dipole interaction between NBBs, which drives the alignment of NBBs parallel to the field lines. The dipole-dipole interactions between particles are denoted as $U = \pi\varepsilon_0\varepsilon_s |C|^2 a^3 E^2$, where ε_0 is the permittivity of free space, ε_s is the solvent dielectric constant, C is the dipole coefficient, a is the particle radius, and E is the field amplitude.[28] For anisotropic NBBs, the potential energy of orientation is related to the anisotropy in electric polarizability of NBBs, which is determined by the electric polarizabilities parallel and perpendicular to the main axis of the NBBs.[29] The key challenge of arraying NBBs from chaotic dispersion is that the dipole-dipole interaction has to be strong enough to overcome the thermal energy kT. To assemble NBBs by this method, electrodes are placed parallel or perpendicular to substrate to apply a direct current (DC) or alternating current (AC) electric filed. To ensure the orientation of NBBs, a number of parameters need to be tuned, including magnitude

of electric field, frequency of the alternating voltage, the size of NBBs, the ligand on NBBs and the solvent.[28, 30]

Most studies of electric field assisted assembly used spherical NPs as building blocks. For example, Hermanson *et al.* reported a class of microwires assembled from aqueous suspension of metallic NPs by dielectrophoresis. When AC electric field (~250 V/cm) was introduced to the suspension of Au NPs, microwires of micrometer diameter and millimeter length were obtained quickly with a growing rate up to 50 μm/s. The formation of wires was explained by the collective effect of electrostatic attraction and dielectrophoretic force.[31] Later, the same group accelerated the formation of close-packed 2D crystals from colloidal particles under AC electric field generated in a coplanar electrode system.[32] In this work, suspension of PS microsphere was placed between two planar electrodes. Within 2s after applying an electric field, the fast chaining of latex spheres was observed due to the dipolar interparticle attraction. As more chains formed, the lateral interactions between these chains induced the formation of hexagonally close-packed 2D array of particles (Figure 1.3). The above-mentioned chaining and crystallization of colloidal particles under electric field are mostly reversible: the assemblies of particles disassembled as soon as the field is turned off. The same group later developed the permanent chaining of particles by co-assembly of positive and negative particles under AC field.[33] A binary mixture of oppositely charged PS spheres was subjected to two coplanar electrodes, and a field-induced chaining of random sequence was observed. Once the electric field was switched off, the break of all chaining between equally

charged neighbors resulted in permanent alternating chains of positive and negative particles persist due to the electrostatic attraction.

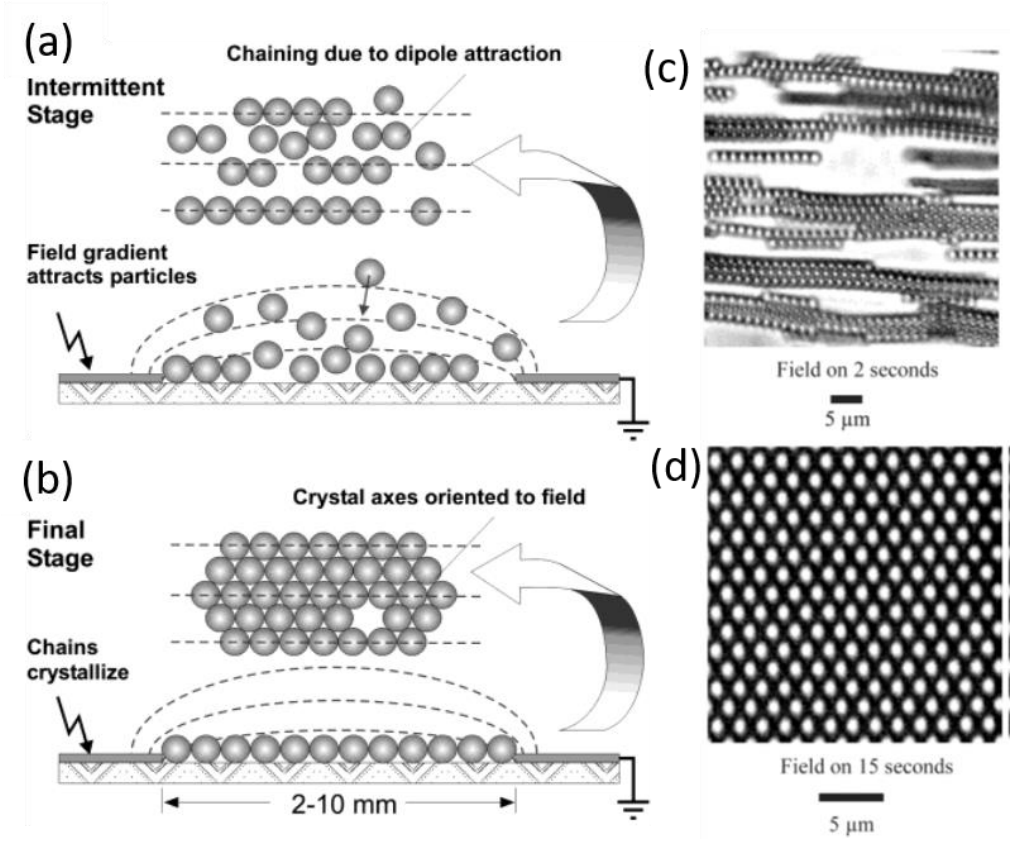

Figure 1.3 Directed assembly of polystryrene spheres under AC filed. (a-b) Schematics of two-stage mechanism of crystallization. (c) Optical microscopy image of 1D chains formed immediately after applying field. (d) Optical microscopy image of 3D hexagonal crystals aligned by the field. (Adapted with permission.[32] Copyright 2004, American Chemical Society.)

Recent work shows that the anisotropic shape of building blocks can have a powerful impact on the spatial orientation of NBBs under external field. For instance, semiconducting CdS and CdSe NRs possess induced and/or permanent dipole moment due to their noncentrosymmetric wurtzite lattice. When an external electric

field is applied, these NRs preferentially align along the direction of field line.[34] A study on the relationship between polarizability and size of TOPO-covered CdSe NRs in cyclohexane under electric field confirmed the existence of permanent dipoles as well as the correlation between dipole strength and volume of NRs.[35] The unscreened permanent dipole moments of the NRs were found to linearly increase with increasing their volume.

When electric field is combined with slow solvent evaporation, the assembly process produces structures with closely-packed NRs. For instance, upon the evaporation of toluene, CdS NRs aligned perpendicular to the substrate to form 2D hexagonal arrays under a DC electric field.[36] Additionally, the assembly process produced an AB layered 3D superlattice of NR arrays in which the upper NRs were selectively placed in the interstitial spacing between NRs in the underlying layer.

1.2.2 Magnetic field

Magnetic field has been widely used for organizing NBBs with permanent or field-induced magnetic dipole moment. Magnetic field can be generated by permanent magnets or electromagnet. The magnitude and spatial distribution of field can be tuned by changing the position of magnet relative to the building blocks. Under an external magnetic field, the dipole-dipole interactions between particles can be attractive or repulsive, depending on the angle between the magnetic field and the line connecting the dipoles of particles.[37] For 1D NRs, the dipole-dipole interactions between NRs are attractive when the NRs take head-to-end configuration, while being repulsive for side-by-side configuration. The dipole moment of NBBs aligned along the magnetic field line to form chains when the dipole-dipole interaction is at least

one order of magnitude greater than thermal energy. For example, when the NPs are close enough, a collective effect of dipole-dipole interactions and van der Waals interactions direct the chain formation of maghemite NPs by applying a magnetic field parallel to the substrate of ferrofluid solution.[38] When the concentration of NBBs increases, the individual chains may become unstable, leading to the formation of 2D arrays of NBBs. Ahniyaz *et al*. induced a magnetic field perpendicular to the substrate surface of maghemite nanocubes (NCs) during the initial stage of drying process, leading to the formation of large and defect free oriented superlattices.[39] In another work, millimeter sized assemblies of aligned cobalt NRs were obtained by drying a dispersion of the NRs under a homogenous magnetic field.[40] When the concentration of NBBs is high, 3D structures can be obtained. As an example, 3D triclinic crystal structures were produced by assembling ellipsoidal Fe_2O_3/SiO_2 core-shell particles under a magnetic field.[41]

In a recent work, Singh and coworkers reported the formation of helical superstructures by assembling magnetite NCs at liquid-air interface with application of external magnetic field.[42] The magnetocrystalline anisotropy of the magnetic NCs favors corner-to-corner interactions, however, the shape anisotropy from cubes favors face-to-face interaction. Therefore, the axes of preferential magnetization [111] do not respond to any of the direction favoring close packing. As a result of the competition between shape anisotropy and magnetocrystalline anisotropy, various types of superstructures were produced, depending on the density of NCs. When the surface concentration of the particles (χ) was around 20% of the monolayer coverage, 1D belts with high aspect ratios were obtained with the crystallographic axes of NCs

oriented parallel to the long axes of belts (Figure 1.4a). When $\chi > 1.5$, the belts folded into single-stranded helices, arising from the orientation of NCs' [111] axes along the magnetic field line (Figure 1.4b). Meanwhile, a high value of χ also led to the widening of the helices and eventually the formation of double- or even triple-stranded helices in which single-stranded helices wrapped around with each other (Figure 1.4c,d).

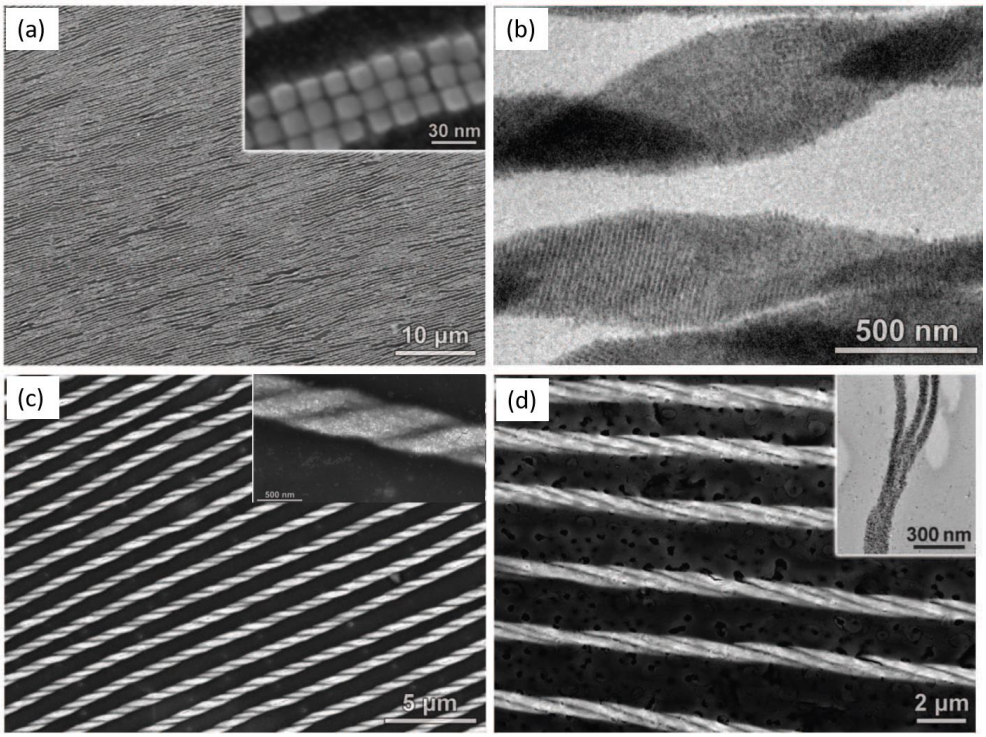

Figure 1.4 Self-assembly of magnetite NCs into helical superstructures. (a) SEM images of 1D belts. (b) TEM image of single-stranded helices. (c) SEM image of an array of double helices. (d) SEM image of an array of triple helices. Inset: the end of a triple helix. (Adapted with permission.[42] Copyright 2014, Science.)

Shape and constituent anisotropy of NBBs can be introduced to control the assembly pathways to produce new assembled structures. Granick *et al.* developed a

magnetic field-assisted assembly of magnetic Janus rods into a fascinating class of colloidal ribbons and rings.[43] Silica rods were coated with a hemicylindrical nickel layer to provide permanent dipole and anisotropic interactions. When the Janus rods were subjected to a strong magnetic field, individual rods align their short axis along the magnetic field and stack into ribbons. When the field direction was switched, the ribbons bucked into rings due to the faster response of ends of ribbon to follow the reversal field than that of the main body of ribbon. This work demonstrates the fascinating complexity that can be achieved in a non-equilibrium dynamic assembly system.

1.2.3 Flow field

As a universal directional force, flow field can be used to direct the assembly of NBBs, not restricted to NBBs with electric or magnetic dipole. The shearing force imposed by the flow can drive the NBBs to align in the direction of the flow, similar to the flow of river pushing logs parallel to the riverside. Microfluidic technique is often adopted for assembly of NBBs, in combination with confinement of selectively patterned surface. When a suspension of NBBs passes through a microfluidic channel, the NBBs preferentially aligned along the flow direction due to the shear force.[44] The alignment and organization of NBBs will be destroyed when the flow field is removed. Thus, chemically patterned surface is used to preserve the assembled structures through the chemical interactions between NBBs and substrate. A pioneer work by Lieber *et al.* showed that parallel arrays of NWs with controllable separation and complex crossed NWs array can be fabricated by using fluidic channels.[45] The scheme in Figure 1.5 illustrates the assembly process as flowing the

NW suspension inside a PDMS-based microfluidic channel. A variety of NWs with different dimensions and compositions (*e.g.*, gallium phosphide, indium phosphide and silicon NWs) were used as building blocks in this work. With controlled flow rate and duration, parallel arrays of NWs with up to millimeter length scales were fabricated. The degree of alignment could be improved by increasing the flow rate. The average separation of aligned NWs exhibited a negative correlation to the flow duration. Moreover, crossed and more complex structure was realized by sequentially assembling NW arrays with different flow directions in layer-by-layer manner.[46]

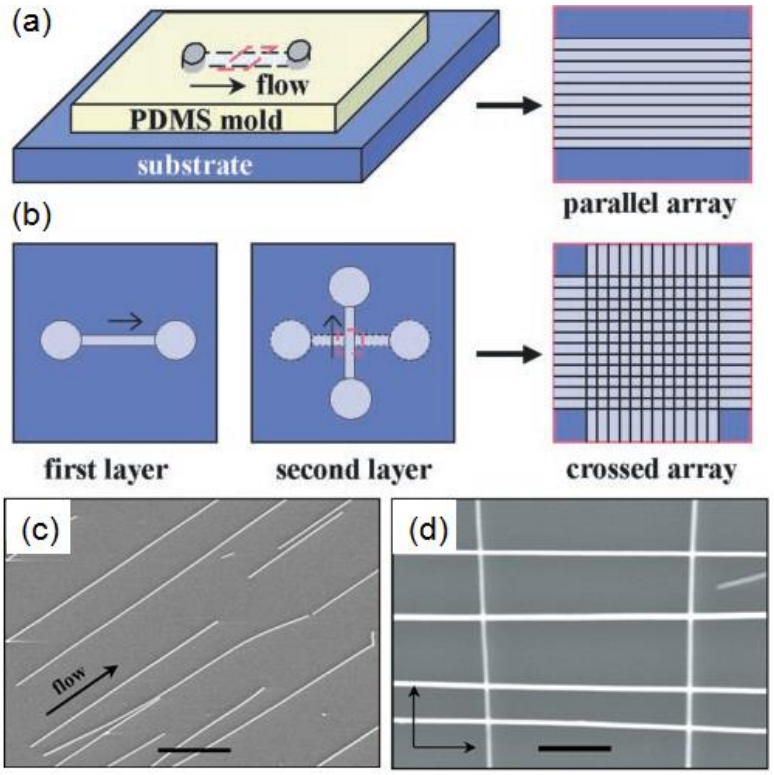

Figure 1.5 Assembly of parallel and crossed NWs using fluidic channels. (a-b) Scheme of flow assembly to form parallel NWs array (a) and multiple crossed NWs array (b) using fluidic channel. (c) SEM image of parallel arrays of indium phosphide NWs. (d) SEM image of crossed arrays of indium phosphide NW. Scale bar: 2 μm. (Adapted with permission.[45] Copyright 2001, Science.)

The assembly of NBBs can be triggered by varying the solvent composition of fluids, when the surface of NBBs is functionalized with ligands that are responsive to the quality of solvents. For instance, Nie and coworkers used a mircofluidic flow-focusing device to assemble amphiphilic BCPs tethered Au NRs and Pt NPs into Janus-like vesicles that can act as vesicular motors for controlled release.[47] In this work, PEO-*b*-PS tethered Au NRs and Pt NPs dispersed in tetrahydrofuran (THF) was introduced into the central channel, while two steams of water were introduced from two side channels. Water works as a poor solvent for PS blocks of BCP tethers. The diffusive mixing of the two fluidic flows along the transverse direction changed the quality of solvents and triggered the formation of hybrid vesicles. The diameter and phase domains of Janus vesicles are dependent on the flow rates of fluids and the relative concentration of building blocks.

As mentioned above, the field-driven assembly shows the following advantages over others. First, it allows effective control over the directionality of NBB arrays by varying the field direction. Second, the driving forces of assembly can be readily tuned by controlling the direction, magnitude and spatial distribution of field. As a result, the field-driven assembly can be designed to be reversible and switchable. Third, when electric or magnetic field is used, the assembly process is independent on experimental conditions, such as pH, temperature and solvent quality, because there is no direct contact between NBBs and resource of field. Last but not the least, it is scalable and can be used for the fabrication of large-area assembled structures. This assembly method, however, has some limitations. The electric or magnetic field-assisted assembly requires that the NCs are responsive to the field.

Additional treatment of resulting assemblies is required to retain the structures after the field is removed. Moreover, as the directionality of most fields is one dimensional, the diversity of assembly structures is limited.

1.3 Assembly at Interfaces and Surface

Interfacial assembly has been widely explored for assembling NBBs into 2D periodical arrays or 3D lattice structures. The organization of NBBs is driven by the reduction in the interfacial energy when particles are transferred from one phase to the interface. Depending on the types of interfaces, the assembly method can be classified into several categories, including liquid-liquid, liquid-air and liquid-solid assembly. Controlled solvent evaporation is commonly used to confine the particles within predetermined area.

1.3.1 Liquid-liquid interface

The self-assembly of particles at liquid-liquid interface started a century ago when Pickering and Ramsden observed that micro-sized particles (*e.g.*, silica particles) formed a resistant film at the interface, which is called as Pickering emulsion.[48] Later Pieranski *et al.* pointed out that the assembly of spherical particles at oil/water interface is attributed to the decrease in the total free energy by placement of a particle at the interface. The reduction in energy can be described using the following equation:[49]

$$\Delta E = -\frac{\pi r^2}{\gamma_{O/W}} \cdot \left[\gamma_{O/W} - (\gamma_{P/W} - \gamma_{P/O})\right]^2$$

Here, r is the radius of particle, $\gamma_{O/W}$, $\gamma_{P/W}$, and $\gamma_{P/O}$ are the interfacial tension between oil/water, particle/water and particle/oil, respectively. It's obvious that larger particles can be trapped at the interface more effectively, for NPs, the thermal energy is comparable to the interfacial energy, while the wettability of the particle surface can also be tuned to reduce the desorption energy. In a classic work finished by Russell's group, TOPO stabilized CdSe NPs with a diameter of 2.8 nm disperse in toluene organized at the interfaces of water and toluene, forming a monolayer at the interface to stabilize the droplet.[50]

For rod-like particles, the interfacial energy change of placing a NR onto the interface can be divided into $\Delta E_{//}$ and $\Delta E_{\perp}$, which correspond to the orientation of a single NR parallel or perpendicular to the interface.[51] Russell and Emrick *et al.* studied the assembly of TOPO-covered CdSe NRs at toluene/water interface and found that the NRs preferred to orient parallel to the plane of interface at low concentration. This was attributed to the fact that the interfacial energy loss of $\Delta E_{//}$ is about 40 times larger than $\Delta E_{\perp}$, due to the larger surface area for parallel orientation of NRs compared with perpendicular orientation.[52] The assembly process is dependent on a range of parameters, including size and concentration of NR, the wettability of particle surface, and the choice of two liquids. Large area of smectic/nematic structures of laterally aligned NRs can be obtained by solvent evaporation from a suspension of NRs in a volatile solvent on top of water.[53]

For NWs with aspect ratio much larger than NRs, they are more favorable to adopt a parallel orientation at the interface. For instance, millimeter-sized monolayer of densely aligned Au NWs was obtained by spreading oleylamine-coated Au NWs

dispersed in hexane on diethyleneglycol (DEG).[54] The long-range ordering of NW arrays can be used to guide the lateral assembly of other small building blocks such as nanospheres (NSs) and NRs in a binary assembly system. For instance, Liz-Marzan and coworkers reported the binary self-assembly of Au NWs and Au NSs/NRs at liquid-liquid interface.[55] A mixture of Au NWs and Au NSs/NRs were dispersed in hexane and drop cast on the surface of DEG. The evaporation of hexane in a controlled manner led to the formation of a film of binary assemblies in which the NWs acted as oriented template to guide the linear organization of NPs or NRs along the long axis of the NWs (Figure 1.6a, 1.6b). In contrast, drying of the same colloidal mixture on solid substrate led to the formation of 3D NW bundles integrated with NSs and NRs (Figure 1.6c, 1.6d).

The template of liquid-liquid interface can arise from the condensation of water droplets during the fast evaporation of volatile solvents. Zubarev *et al.* used condensed water droplets to template the organization of Au NRs into ring-like superstructures.[56] Upon the evaporation of solvent, PS-coated Au NRs dispersed in dichloromethane (CH_2Cl_2) spontaneously assembled into ring structures with high yield. The ring formation was attributed to the template effect of water droplet/CH_2Cl_2 interfaces formed from the condensation of water during the evaporation of highly volatile solvent.

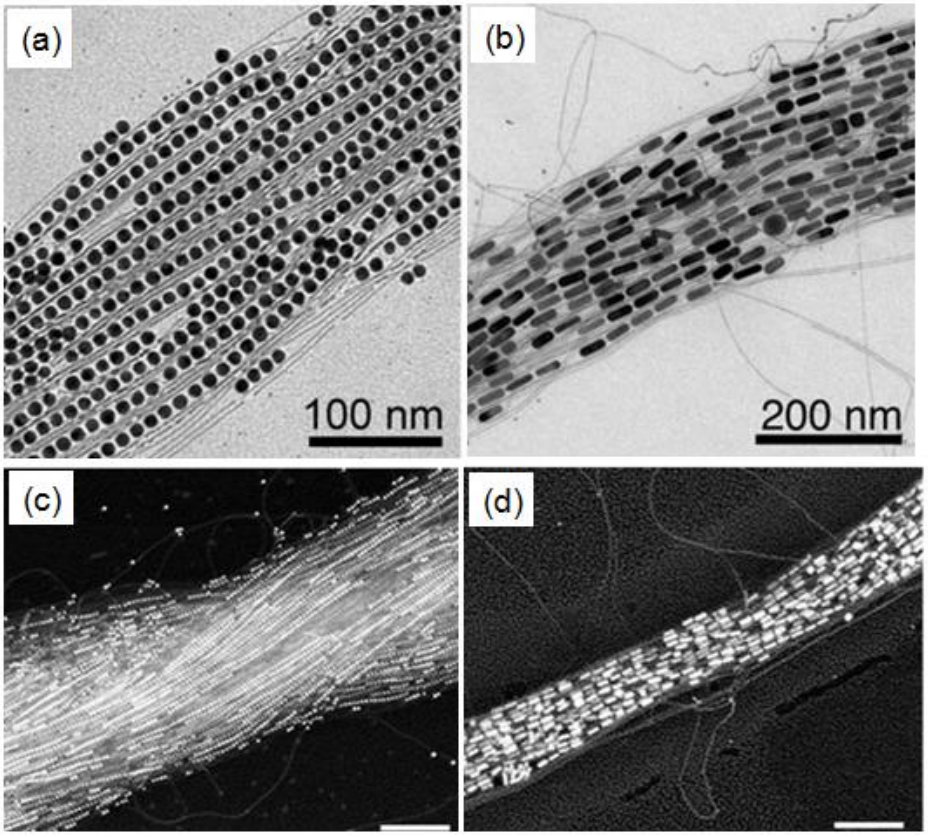

Figure 1.6 Co-assembly of Au NWs and Au NSs/NRs at liquid-liquid interface. (a-b) TEM images of linear binary assemblies of Au NS (a) and Au NRs (b) with Au NWs. (c-d) SEM images of Au NSs (c) and Au NRs (d) embedded in Au NW bundles. Scale bar: 200 nm. (Adapted with permission.[55] Copyright 2010, Wiley-VCH.)

1.3.2 Liquid-air interface

The assembly of NBBs at liquid-air interface via Langmuir-Blodgett (LB) technique can produce large-area monolayer of parallel NBBs. As shown in Figure 1.7, NBBs dispersed in an organic volatile solvent (*e.g.*, chloroform or hexane) are spread evenly over water surface using a LB trough. The NBBs form a water-supported monolayer at the interface after the evaporation of the top liquid. The lateral compression at a controlled speed generated a compact monolayer of ordered

NBB arrays, which can be subsequently transferred to desired substrate by horizontal or vertical lift-off. Large-scale assemblies of both closely packed arrays and well-defined patterns with low packing density of NBBs have been produced by using the LB technique.[57] The formation of NBB arrays can be tuned by varying the size, passivating ligand of NBBs and surface pressure. A pioneer work by Yang and coworkers reported the fabrication of a monolayer of Ag NW arrays with area over 20 cm^2 using this technique.[57d] Ag NWs were functionalized with 1-hexadecanethiol ligands to render hydrophobic surface and were dispersed in chloroform. The packing density of NWs increased gradually with the increase of surface tension. Above a certain surface tension, the monolayer underwent an insulator to metal transition, implying a remarkable side-by-side alignment of Ag NWs parallel to the trough barrier (Figure 1.7c-d). Owing to the ease in transferring the assembled film to desired substrate, multi-layer films can be prepared by repeatedly depositing monolayer film onto a substrate to produce, mesh-like mesostructures with defined cross angle between layers in a layer-by-layer fashion.[57c, 58] It is worth mentioning that in order to disperse NBBs in solvents above the water phase, it is usually necessary to functionalize NBBs with hydrophobic capping agent via ligand exchange.

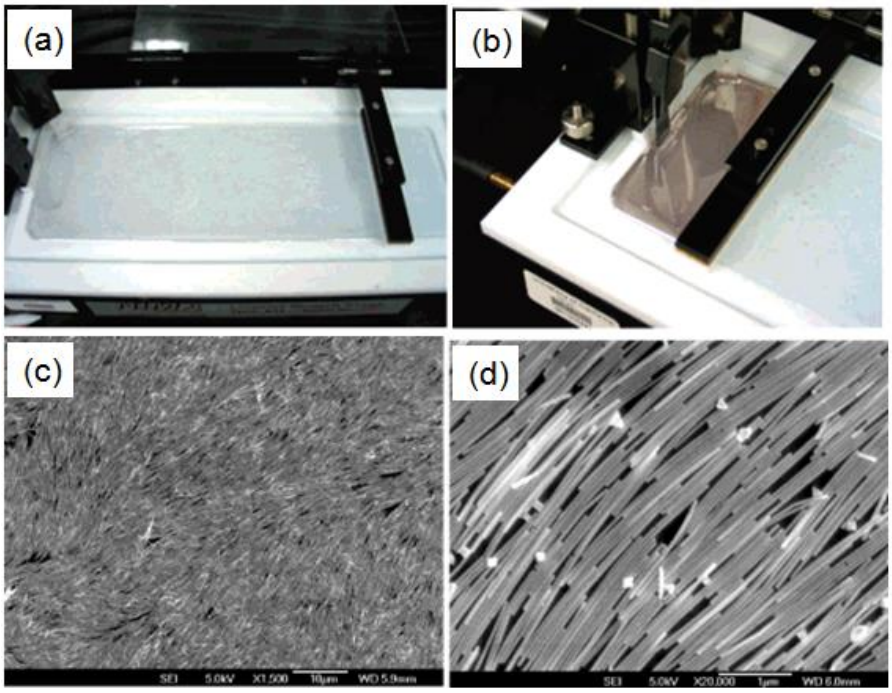

Figure 1.7 Assembly of Ag NW using LB technique. (a-b) LB NW assembly process at initial (a) and final (b) compression stage. (c-d) SEM images of Ag NWs monolayer at different magnification. (Adapted with permission.[57d] Copyright 2003, American Chemical Society.)

When relatively short NRs are used, the organization of NRs is largely dependent on the size, aspect ratio and surface functionality of NRs.[57a, 59] As in a study by Yang *et al.*, $BaCrO_4$ NRs with small aspect ratio (3-5.1) exhibited an assembly transition from isolated raft-like aggregates to 2D smectic arrangement and further to 3D nematic configuration with increasing surface pressure.[59a] In contrast, longer NRs with aspect ratio of ~150 assembled into nematic layer with NRs aligned roughly along the same direction and into bundles of NRs when the compression is strong. The experimental observation is in good agreement with the simulations on the phase behavior of hard rods.

1.3.3 Evaporation mediated assembly on solid surface

Evaporation mediated assembly offers a simple inexpensive method to produce highly ordered close-packed superstructures of NBBs on solid surface. Typically, a dispersion of NBBs is allowed to dry and assemble on solid substrate into well-ordered structures under a confined geometry and at a controlled drying rate. During the drying process, if the evaporation of liquid is faster than the diffusion of NBBs in liquid, the local particle concentration will be larger in the area right underneath the liquid surface. The surface tension will drive the self-assembly of NBBs into 2D monolayer at the surface. Continuous evaporation results in the formation of another layer on the surface of the first layer. The receding of the evaporation front pulls the particles in solution towards the drying front by convection, depositing well-ordered particles in the drying front gradually.

The organization of NBBs is largely determined by various parameters, including shape and concentration of NBBs, assembly conditions (*e.g.*, solvent, temperature) and surface property (*e.g.*, hydrophobicity) of substrate.[60] Wang *et al.* studied the shape dependency of assembly of Au nanocrystals by solvent evaporation.[61] Au NRs assembled preferentially into nematic or smectic A phase (Figure 1.8b, c). When binary Au NRs with different diameters (and different resulting aspect ratios) are used, the two populations of NRs self-separated to form smectic superstructures (Figure 1.8d). Other shaped NPs such as polyhedral, NCs and bipyramids formed hexagonally packed, tetragonally packed and nematic/three-dimensionally ordered structures, respectively (Figure 1.8 e-h). Korgel *et al.* explored the self-assembly of CdS NRs at a relatively low surface coverage on a substrate. The

assembly process produced networks of stripes consisted of NRs packed next to each other and aligned parallel to the stripe direction, rather than close-packed assemblies. Increasing the concentration of NRs led to the formation of perpendicular orientation of NRs in a smectic phase.[62]

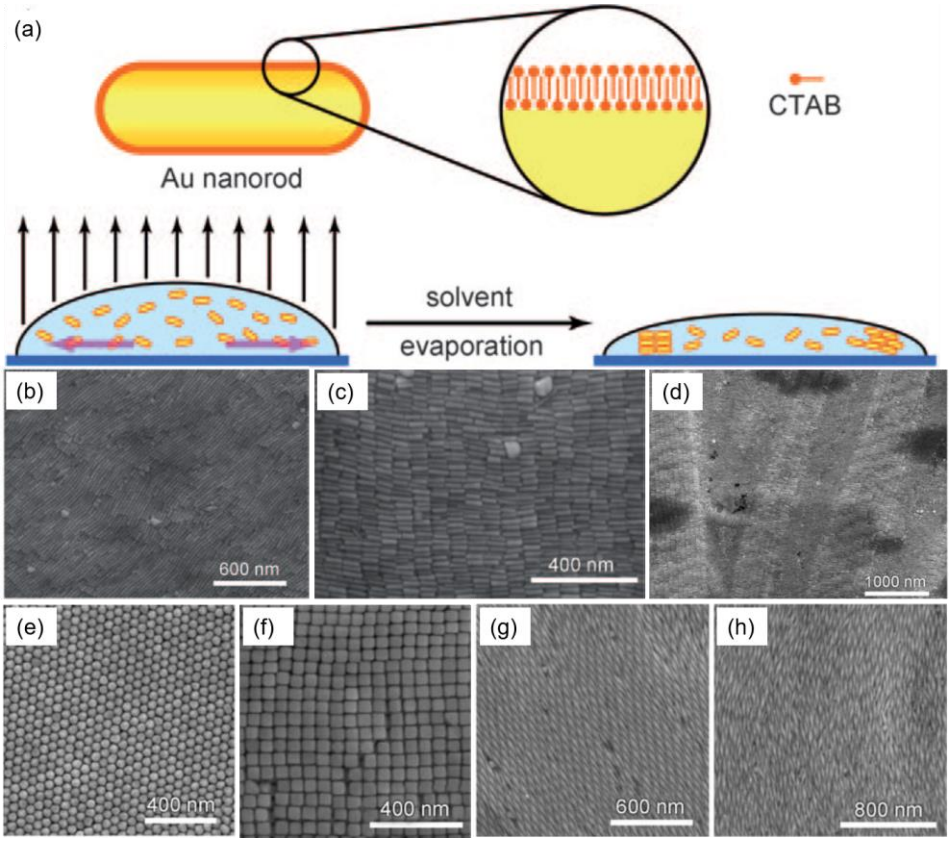

Figure 1.8 Evaporation induced assembly of Au nanocrystals. (a) Schematic illustration of evaporation mediated assembly of Au NRs on substrate. (b-c) SEM image of nematic (b) and smectic-A (c) superstructure formed by Au NRs with aspect ratio of 4.4. (d) SEM image of the self-separation of smectic superstructure formed by Au NRs with aspect ratio of 4.4 and 3.8. (e-h) SEM images of hexagonally packed Au polyhedral (e), tetragonally packed Au NCs (f), 3D ordered (g) and nematic superstructures (h) of Au bipyramids. (Adapted with permission.[61] Copyright 2008, Wiley-VCH.)

The evaporation rate of solvent, which is dependent on factors such as temperature, partial pressure and volatility of solvents, is crucial to the formation of well-ordered structures. In addition, a few other parameters such as polarity and permittivity (for charged ligand) of solvent also play an important role in controlling the solubility and interaction of NBBs. As an example, Koster *et al*. observed the transition of NR assemblies from nematic to hexagonal packing, when non-polar solvent (*e.g.*, toluene) was changed to polar solvent (*e.g.*, ethanol or water).[63]

The aforementioned research illustrates the inherent complexity in the dynamical process of drying-mediated self-assembly.[64] For better understanding and control of assembly, it is necessary to systematically optimize the assembly conditions and quantitatively assess the assembled structures. For instance, Alivisatos *et al*. aligned CdS NRs vertically on many device-relevant substrates at centimeter scale and quantitatively analyzed the orientation distribution of NRs over the entire film.[64b] The quantitative study established a correlation between the assembly conditions (i.e., temperature, aspect ratio of NRs and substrate) and the overall orientation of NRs. At the optimal condition, 96% vertical alignment of NRs on 1 cm^2 silicon nitride substrate was obtained.

Self-assembly at interface and surface provides a facile and affordable way to efficiently organize NBBs into large-area ordered structures. The assembly method does not require expensive apparatus. A rich variety of assembly morphologies can be obtained, including loose or close packing, parallel or vertical array, monolayer or multi-layer of NBBs. In this method, solvent and ligands on NBBs have to be carefully selected and assembly conditions need to be optimized before large-area

ordered structures can be generated. However, the complexity and hierarchy level of the overall assemblies by this method is restrained by the nature of this method. In order to achieve more complex organization of NBBs, it is usually necessary to combine this approach with other assembly techniques.

1. 4 Ligand Guided Assembly

Functional ligands capped on the surface of NBBs or dispersed in solution are routinely employed by chemists to control the organization of NBBs at the molecular level. Generally, a diverse range of ligands (*e.g.*, small molecules, polymeric species or biomolecules) can contribute to the assembly of NBBs in the following ways: i) serve as a linker to guide the assembly via molecular recognition of functional groups; ii) serve as scaffold to direct the assembly via both spatial and chemical template; and iii) serve as depleted additives to drive the assembly via depletion force. As a result, this assembly strategy allows one to organize NBBs into structures with high complexity or precision.

1.4.1 Small molecules

In general, small molecules possessing short chains diffuse faster and bind more efficiently to the surface of NBBs than large molecules. Small molecules have been extensively explored of guiding the assembly of NBBs. A frequent choice of such ligands is bifunctional molecules of which one group binds to the NBBs and leaves the other group free to bind another NBB. Bifunctional ligands such as dithiol molecule, thioalky carboxylic acids, cysteine and glutathione can be used to drive the assembly of Au and Ag nanocrystals due to the bridge effect of the ligand.[65] For

instance, Novak *et al*. obtained a series of supracolloids such as dimer, trimer, tetramer by tethering Au and Ag NPs with thioacetyl-terminated phenylacetylene.[65a] Other than covalent or hydrogen bonds of bifunctional linker, a series of molecular interactions can be employed to guide the assembly of NBBs. They include solvent-mediated hydrophobic interactions between alkanethiol,[66] coordination bond formation of transition metal complexes,[67] electrostatic interactions between charged NBBs (or between charged linkers and NBBs), etc.[68]

The above-mentioned small molecules spontaneously interact to drive the assembly upon NBB collision. In addition, molecular linkers that can be regulated by external stimuli such as light and pH change are also attractive for the development of responsive assembly systems.[65e, 69] Liz-Marzan *et al.* reported the use of a femtosecond laser irradiation to assist the assembly of Au NRs into dimers while inhibiting the formation of trimers and longer oligomers.[69b] In this work, dithiol was used as molecular linker. Au NRs with appropriate aspect ratio were used to ensure that the laser wavelength is in resonance with the longitudinal LSPR bands of trimers and longer oligomers, but above that of monomers and dimers. Upon irradiation of 800 nm, the localized enhancement of electromagnetic field at interparticle gap led to an increase in local temperature and the decomposition of molecular linkers within trimers and longer oligomers, thus leading to a significant increase in the yield of dimers. The pH dependency of ligands provides another route to achieve real time control over the assembly of NRs. For example, Wang *et al.* reported a reversible pH controlled assembly of Au NRs by mixing NRs with a class of bifunctional molecules such as 3-mercaptopropionic acid, 11-mercaptoundecanic acid, glutathione and

cysteine.[65e] The different charge states of these molecules in selective pH range were assumed to result in the reduction of locally repulsion between NRs and hence the assembly of NRs.

The addition of a nonsolvent ligand, (*i.e.*, depletant additive) can induce instability and subsequent assembly of NBBs. The depletant additives usually have a high solubility in the solvent, but they do not interact with the NBBs. When particles in solution approach each other, an osmotic pressure in the volume region between the particles arises, which cannot be occupied by the additive. Therefore, the attractive interaction between the particles is generated to drive the assembly of particles, refers to the depletion force. Except for the size and concentration of additives, people can also tune the strength of depletion interaction by the shape, size, and concentration of colloidal particles.[70] Cao and coworkers reported the assembly of CdSe/CdS core-shell semiconductor NRs into spherical or needle–shaped superparticles with multiple supercrystalline domains by over-coating NRs with dodecyltrimethylammonium bromide (DTAB) surfactants.[70b] As shown in Figure 1.9, CdSe/CdS NRs originally capped with octylamine and Octadecylphosphonic acid (ODPA) was first transferred into water to form NR-micelle solution by mixing the NRs with an aqueous solution of DTAB. Subsequently, continuous transfer of the NR-micelle solution into ethylene glycol led to the detachment of DTAB molecule from the NRs and triggered the fast assembly of NRs. The amount of DTAB was found to affect the kinetics of superparticle formation and control the size of superparticles. The selective removal of ligand of NRs can also change the surface chemistry and drive the anisotropic interactions among NRs.[71] Recently, an end-to-

end connection of CdSe NRs driven by the ligand desorption-adsorption equilibrium at the NR surface was reported by Nakashima *et al.* CdSe NRs were modified with water-soluble small molecular thiols such as 2-(dimethylamino)ethanethiol hydrochloride (DMAET). During static aging of the aqueous solution, the weaker binding affinity of DMAET at the NR ends led to the formation of amphiphilic NRs with hydrophobic ends and hydrophilic sides and the consequent end-to-end association of such NRs due to hydrophobic effect.[71a]

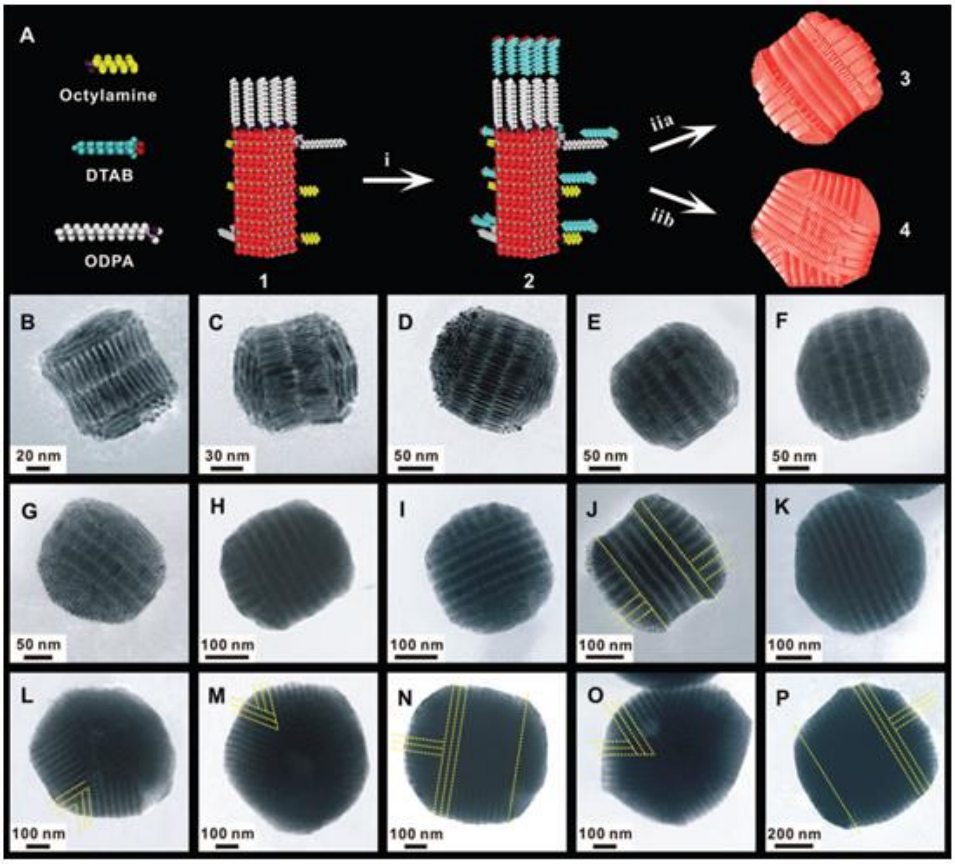

Figure 1.9 Spherical superparticles formed by CdSe/CdS NRs. (A) Schematic illustration of the formation of superparticles form CdSe/CdS NRs. (B-P) TEM images of superparticles made from NRs with length of 28 nm, and width of 6.7 nm. (Adapted with permission.[70b] Copyright 2012 Science.)

1.4.2 Polymeric species

Polymers represent an attractive class of ligands for guiding the assembly of NBBs, as the functionality of polymers can be readily tailored for different applications.[72] The flexible length, chemical composition and conformation of polymer species play a more powerful role on tuning the interparticle spacing and spatial arrangement of NBBs. This is especially meaningful for increasing the structural tunability of superlattice, as interparticle distance can be experimentally tuned with high precision ranging from one to several tens of nanometers. For instance, Ye *et al.* fabricated 10 different 2D and 3D superlattices by co-assembly of binary NPs grafted with polymers.[73] In this work, Au NPs and Fe_3O_4 NPs with different sizes were tethered with thiol-terminated and carboxyl-terminated PS, respectively. A rich variety of 2D and 3D binary superlattices were formed by slow evaporation of toluene solution of mixed particles on top of DEG. The use of polymeric ligands allows precise and quantitative control over the interparticle distance compared with small molecule ligand.

According to Glotzer's simulation works, amphiphiles made from polymer-tethered NBBs can be considered as a new class of "macromolecule" whose assembly can be controlled for the generation of new materials.[74] These building blocks have the features of common BCPs, while show much richer assembly structures due to the additional features induced by the NBBs' rigidity and geometry, combined with the immiscibility of polymer tether and NP. For instance, Nie's group fabricated a class of amphiphilic colloidal molecules by tethering Au NPs with amphiphilic block polymers such as PEO-*b*-PS.[75] The change on the solvent quality will drive the

assembly of the hybrid Au NPs into well-defined tubular and vesicular structures composed of a monolayer of hexagonally packed Au NPs.

The anisotropy on geometry of the particles will further rich the assembly behavior of the polymer grafted building blocks. Take NRs as an example, amphiphiles consisting of NR tethered with a single polymer at one end can form a rich variety of phases, including smectic C phase, zig-zag lamellar phase, cubic micelle phase, monolayer/bilayer arrowhead phase, tetragonally/hexagonally perforated lamellar phase, honeycomb phase, double gyroid phase, and hexagonal chiral cylinder phase.[74a, 76] The formation of different phases is strongly dependent on the relative fraction of polymer tethers and aspect ratio of tethered NR. For laterally-tethered rod, the amphiphiles assemble into centered rectangular stepped-ribbon phase, lamellar phase, helical scrolls, honeycomb grid, pentagonal grid, square grid, and bilayer sheet structures, depending on the length of NRs.[77]

The concept of NP amphiphile made from single polymer chain-grafted NPs is intriguing. Liu's group realized the monofunctionalization of ultra-small Au NPs (<4 nm) with a single amphiphilic triblock copolymer in a stoichiometric reaction manner.[78] The triblock copolymer consists of one hydrophilic block PEO and one hydrophobic blocks PS at the ends, and an middle block poly(lipoic acid 2-hydroxy-3-(methacryloyloxy)propyl ester-*co*-glycidyl methacrylate) which can bind with 1,2-dithiolane functionalized Au NPs. The asymmetrically functionalized Au NPs were able to assemble into micelles, vesicles and rods based on the rich microphase separation behavior of the amphiphilic surface block.

However, 1D NRs grafted with single polymer chain has barely been demonstrated in experiments to date. This is largely due to two reasons: i) the challenge in the synthesis of such building blocks, and ii) the mismatch in the dimension of single polymer chain and NP. Instead, researchers selectively modified NR with many polymer tethers at both ends to construct NP amphiphiles, which can assemble into various functional structures. As an inspiring example, Kumacheva *et al.* selectively grafted thiol-terminated hydrophobic PS to both ends of hydrophilic Au NRs covered with CTAB at the longitudinal side. The preferential grafting of polymers at ends can be explained by the deprivation of CTAB ligands at the (111) crystal facets at ends of the rods. The resulting building blocks could assemble into a range of structures including rings, nanochains, bundles, nanospheres and bundled nanochains in selective solvents, analogous to ABA amphiphilic triblock copolymer (Figure 1.10).[79] The formation of different assemblies was attributed to the amphiphilic feature of PS-grafted NRs which possess hydrophobic ends and hydrophilic center.

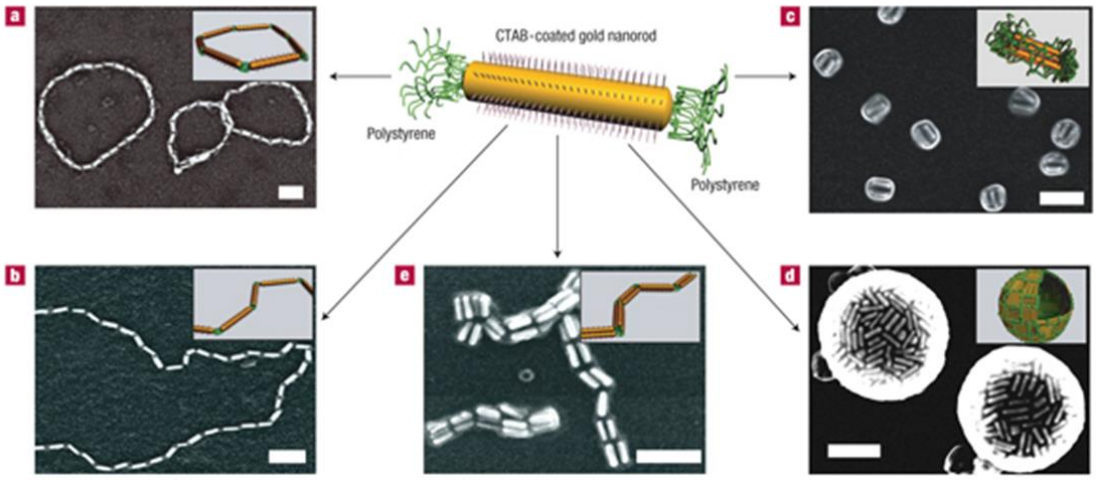

Figure 1.10 Self-assembly of polymer tethered Au NRs in selective solvents. (a-e) SEM images of self-assembled Au NR structures: rings (a) and chains (b) formed in dimethyl formamide (DMF)/water mixture at water content of 6 and 20 wt%, respectively; side-to-side bundles of NRs (c) and nanospheres (d) formed in THF/water mixture at 6 and 20 wt%, respectively; bundled NR chains obtained in DMF/THF/water mixture at weight ratio of liquids 42.5:42.5:10. (Adapted with permission.[79] Copyright 2007, Nature Publishing Group.)

1.4.3 Biomolecular ligand

DNA strands are extremely attractive in precise position and organization of colloidal NBBs owing to their programmable base-pairing interactions, ease in introducing different functional groups, and readily automated synthesis. Single or numerous DNA strands can be bonded to the surface of NBBs to guide the fabrication of discrete clusters or well-defined superlattices via DNA-recognition interactions.[80] Mirkin *et al.* proposed a set of basic rules for designing nine crystallographic symmetries using DNA as a programmable linker.[80c] Later, Gang's group presented a

general approach to create heterogeneous NP superlattices by co-assembly of multifunctional single stranded DNA capped NPs.[80e] Tikhomirov *et al.* reported the self-assembly of quantum dot complexes with various valence using CdTe NPs capped with well-designed DNA sequences.[81] DNA functionalized CdTe nanocrystals were synthesized via a one-pot process. The DNA ligand was composed of three domains: a quantum-dot-binding domain which can tune the spectral properties and the valence of the quantum dots during synthesis, a spacer containing phosphodiester linkages which can tune the interparticle distance, and a DNA-binding domain which hybridize with the complimentary domain from another particle. As shown in Figure 1.11, CdTe NPs with 5 different valences and brightness were obtained, which can further assemble into a variety of quantum dot complexes using similar core quantum dot but with different valence (Figure 1.11b). More intricate structures were also obtained including linear ternary complexes and cross-shaped ternary complexes, as shown in Figure 1.11c.

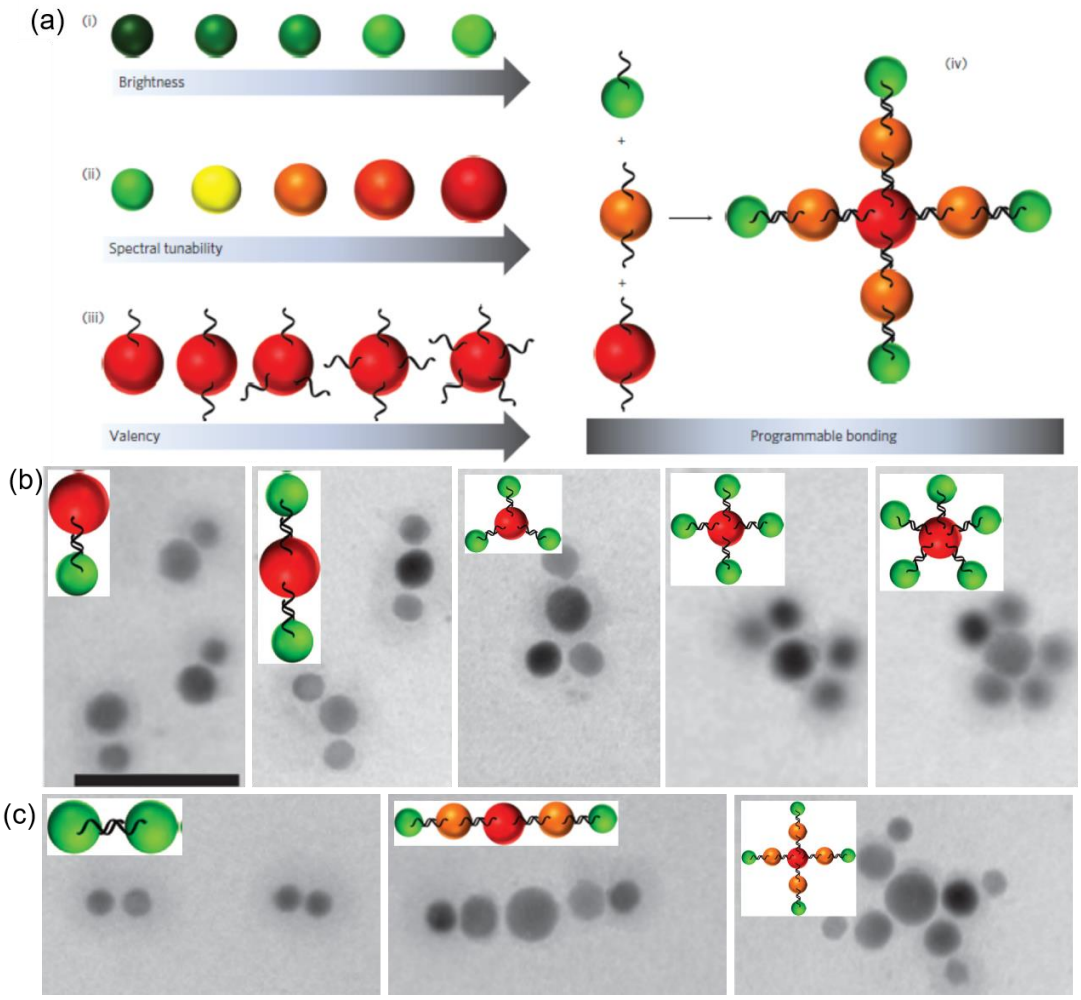

Figure 1.11 Quantum dots complexes formed by DNA-capped CdTe nanocrystals. (a) Schematic illustration of synthesizing DNA coated CdTe nanocrystals with tunable spectral property and valence, and their further assembly into quantum dots complexes via DNA hybridization. (b) Quantum dots assemblies using same red particle with valences of 1-5 to bind with different number of green particle. (c) Symmetric binary system made from the same green particle (left); linear ternary complex (middle) and cross-shaped ternary complex (right) made from three different dots. (Adapted with permission.[81] Copyright 2011, Nature Publishing Group)

The shape effect of NBBs on their assembly behaviors were studied using a series non-spherical NBBs. It was found that the shape of NBBs strongly dictates the resulting crystallographic symmetry of assembled superlattice. The 2D superlattice assembled from Au NRs exhibited long range hexagonal symmetry. In contrast, triangular nanoprisms, with length and width greater than its depth, assembled into 1D lamellar arrays with particles stacked in a face-to-face configuration.[82] This anisotropic shape largely facilitates the directional bonding interactions by maximizing DNA linker interactions to reach the most stable structure. The complementary interactions between DNA ligands are reversible, thus enabling responsive assembly of NBBs and tunable properties of assembled structures. For instance, assembly and disassembly of DNA-grafted Au NRs in response to temperature variation can be used to reversibly tune the plasmonic circular dichroism response of the system.[83] Gang *et al.* fabricated 1D ladder-like ribbons with side-by-side arrangement of Au NRs using single-stranded DNA as molecular linker.[84] The reversibility of DNA hybridization allows the temporal evolution of 1D ribbons into 3D morphology at later stages of assembly.

Folding programmed DNA sequence into intricate geometries constructs DNA origami which can be used as template to program the position of NBBs.[85] The DNA origami is formed by folding a long scaffold strand with the help of hundreds of short 'staple' strands into various 1D, 2D and 3D well-defined shapes. Typically, binding regions are incorporated into the origami to capture particles bearing complementary DNA sequence. Sophisticated superstructures with precisely positioned NBBs can be constructed by designing the pattern of the capturing strands on the scaffold.[86] Kuzyk

et al. designed a DNA origami with 24-helix bundles which contains nine helically arranged anchoring site for Au NPs coated with complementary single-stranded DNA.[87] The conjugation of Au NPs with the attachment site results in left- and right-handed nanohelices composed by nine Au NPs. Ding *et al.* constructed a nanoplatform by assembling single Au NR on the surface of triangular DNA-origami structures with DNA capture strands extended from one arm of the template.[88]

Other biological molecular recognitions (*e.g.*, antibody-antigen interactions) have also been utilized to assemble NBBs. Take the assembly of NRs as example, in a pioneering work by Murphy *et al.*, biotin-coated Au NRs assembled end-to-end upon the addition of streptavidin.[89] Kotov and coworkers assembled Au NRs carrying MC-LR antibodies or its ovalbumin antigen in both side-to-side and end-to-end modes in a controlled manner.[90] More complex assemblies can be generated when the presence of proteins is localized. For instance, gold-tipped CdSe NRs immobilized with avidin and biotin on the Au nanodomain organized into dimers, trimers and flowers of NRs, depending on the ratio of biotin and avidin to NRs.[91]

Ligand-guided assembly offers plenty of room for chemists to tune the assembly of NBBs. This method is easy to perform and most of the assembly can be fulfilled in solution phase without the use of special instrument. The assembly of NBBs is driven by interparticle forces, which owns a great variety of directionality and specificity of interactions. Except for the use of DNA origami, the ligand-guided assembly usually does not offer good directionality as field-driven assembly or high precision in the organization of NBBs as templated assembly.

1.5. Scope of the dissertation

As discussed in the previous sections, self-assembly of NBBs has proven to be an efficient way to create a vast range of nanostructures with desired properties in a predetermined manner. Recent advances in the synthesis of nanocrystals have offered us a large library of building blocks for assembling functional materials, while the development of novel assembly approaches becomes more significant in order to exploit the properties and applications of these materials. I have chosen NPs modified with functional BCPs as the starting building block for *i) the facile synthesis of polymer with well-designed chemical composition and length; ii) the flexible conformation of polymer ligand on the surface of NPs and their interaction softness on directing the assembly behavior and tuning the structure; iii) the incorporation of NPs with functionality with polymers to form various superstructures with collective properties*. The objective of this dissertation is to study *i) self-assembly of BCP tethered NPs at multiple hierarchy levels by designing different functional blocks; ii) the effect of polymer length, particle size and environmental stimuli (such as pH) on the self-assembly at each level of hierarchy*.

Chapter 2 describes the design of amphiphilic supracolloids with defined valence by co-assembly of binary BCP tethered NPs. The Lewis acid/base containing blocks of these BCP tethers drive the assembly of NPs via acid/base neutralization of the polymer chain. The size, shape and composition of NPs and the length of BCPs were tuned to study the assembly mechanism and to enlarge the family of supracolloids. Chapter 3 describes the hierarchical assembly of amphiphilic supracolloids obtained in Chapter 2. The assembly process was triggered by placing a

solution of supracolloids in tetrahydrofuran on top of immiscible salt-saturated water and evaporating the solvent. As a demonstration, amphiphilic supracolloidal dimers and trimers with controlled chemical patches were used as building blocks to further assemble into hierarchical structures, including petal-like structures, chains and ribbons. Chapter 4 describes a systemic study on the formation of ribbon structures from amphiphilic supracolloidal trimers with hydrophobic center and hydrophilic ends. The lengths of hydrophobic and hydrophilic block of BCP tethers were tuned for understanding their role of polymer length and conformation on the assembly process. Chapter 5 describes the pH effect on the hierarchical assembly of amphiphilic supracolloidal trimers. Different amount of acid or base were added into the bottom water phase during the further assembly of trimers, in order to study how the change in the amphiphilicity and the competition between hydrophobic force and electrostatic interaction influence the formation of different structures. In Chapter 6, a brief summary of completed work was given and recommendations for the future work are also presented.

Chapter 2: Designing nanoscale amphiphilic supracolloids with valence by co-assembly of binary hybrid building blocks

Overview. We report the design of amphiphilic supracolloids with defined valence by co-assembly of binary hybrid building blocks. Two types of functional BCPs containing either Lewis acid or base in one of their blocks were attached to two types of NPs (different in sizes or compositions) separately to form binary hybrid building blocks. The reaction between the Lewis acid and base moieties of BCPs on complementary NPs drives the self-assembly of NPs to form bimolecular compound-like supracolloids with various geometries and valences, which resembles bimolecular compounds, such as HF, CO_2, BF_3, XeF_4, and alternating copolymers.

A manuscript based on this chapter and chapter 3 is in preparation to be submitted to *Nature Material*, and another manuscript partially based on this chapter is in preparation to be submitted to *Science*.

2.1 Introduction

In a classic talk given by Richard P. Feynman at the annual meeting of the American Physical Society in 1959, he proposed "*The principle of physics, as far as I can see, do not speak against the possibility of maneuvering things atom by atom. It is not an attempt to violate any law; it is something, in principle, that can be done; but in practice, it has not been done because we are too big.*" After almost 60 years, atomic manipulation of chemical is still in its early stage. Inspired by this, the construction of colloidal molecules from colloidal NPs, just like building molecules from atoms, has attracted great interest for fundamental understanding of colloidal interactions, as well as property discovery and application development of inorganic NPs.[1b] Assemblies of inorganic NPs often exhibit unique physical and chemical

properties beyond their bulk counterpart or individual NPs, which makes them attractive for use in plasmonic devices, solar energy harvesting, biological detection, etc.[2, 92] For instance, a "plasmonic ruler" can be designed to estimate the interparticle separation of Au NSs, based on the plasmonic band shift due to the interparticle spacing-dependent plamonic coupling between closely placed plasmonic NPs. The relative shift of plasmonic band is well approximated by an exponential decay, which is correlated with the edge-to-edge separation between the NPs and the diameter of NPs.[93]

Currently, there are two major strategies for the fabrication of plasmonic NP-based colloidal molecules: top-down nanofabrication techniques, and bottom-up self-assembly of colloidal NPs. Electron beam lithographic patterning, a highly practical top-down method, has been widely used to fabricate well-defined plasmonic clusters with precisely controlled NP shape and size and interparticle distance.[94] However, the reliance on clean rooms and specific instrument along with the challenges associated with the fabrication of 3D structures largely limit the applicability of this technique. Conversely, the prosperity on wet chemical synthesis of NPs has greatly diversified the bottom-up self-assembly of colloidal molecules. A variety of approaches have been developed, including interfacial assembly, molecular ligand (small molecules, polymer, protein, DNA etc.) assisted assembly, templated assembly and external field directed assembly.[28, 59b] Among others, DNA-based assembly has been used to fabricate NP clusters with controlled valence by tethering NPs with specifically designed complimentary DNA sequences.[81, 95] In this case, NPs are site-specifically functionalized with defined numbers of DNA. Despite the amazing complexity of

assemblies that can be achieved, DNA-based assembly shows limitations, such as sophisticated purification process, relatively low yield of production, lack of mechanical property of assembled structures (i.e., few work was reported to tune the mechanics of 3D DNA-NP assemblies). Nevertheless, there is urgent need for a simple yet robust strategy for assembling NPs into high-quality supracolloidal molecules (i.e., clusters with precisely positioned multiple types of NPs) in high yield.

In this chapter, we describe a new strategy for the fabrication of high-quality supracolloidal molecules with controlled valences by co-assembly of binary hybrid building blocks. As a demonstration, Au NPs with different sizes were used as a model system. As shown in Figure 2.1, the NPs were surface-modified with one of the binary BCPs with one block containing complementary functional groups that can react. A typical combination of BCPs is thiol terminated poly(ethylene oxide)-*block*-poly(N, N-dimethylaminoethyl methacrylate-*r*-styrene) (*Abbrev:* PEO-*b*-P(DMAEMA-*r*-St)-SH) and polystyrene-*block*-poly(acrylic acid-*r*-styrene) (*Abbrev*: PS-*b*-P(AA-*r*-St)-SH). The corresponding BCP-grafted NPs are referred to as building block **A** and **B**. The block of randomly copolymerized styrene and a proton donor (carboxylic group) or acceptor (tertiary amine group) allows for independently tuning the block length and ratio of reactive moieties, thus the interactions between binary building blocks. The assembly process was triggered by mixing binary building blocks in a favorable solvent for the BCPs, such as THF. Supracolloids with defined valences were formed in high yields through the neutralization reaction between the binary particles as giant spherical Lewis acids and Lewis bases. A variety

of supracolloids with defined valence were produced by tuning the length of polymers and size of NPs. They include dimers (**AB**), trimers (**BA_2** and **AB_2**), tetramers (**BA_3** and **AB_3**), pentamers (**BA_4** and **AB_4**), and alternating chains **$(AB)_n$**. (More complex supracolloidal molecules have been also demonstrated in a separated project in the group). These supracolloids exhibit amphiphilic surface which is determined by the local polymeric patch (i.e., the PEO or PS block of BCPs on the building block **A** and **B**).

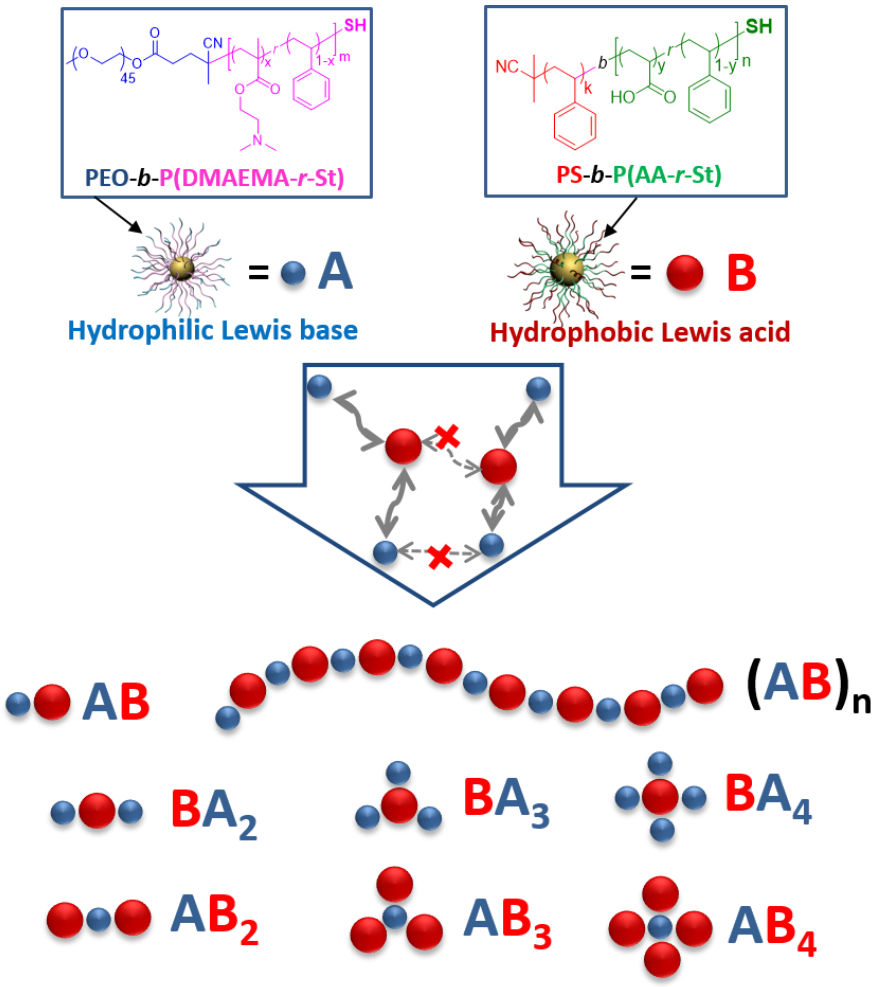

Figure 2.1 Schematic illustration of building supracolloidal molecules with valence by co-assembling binary hybrid building blocks composed of inorganic NPs functionalized with complementary BCPs.

2.2 Experiments

2.2.1 Materials

Gold (III) chloride trihydrate ($HAuCl_4$, ≥99.9% trace metals basis), sodium citrate tribasic dihydrate (≥99%), iron(III) chloride hexahydrate ($FeCl_3 \cdot 6H_2O$), sodium oleate (NaOL), oleic acid, silver nitrate ($AgNO_3$), potassium iodide, ascorbic acid, PVP, THF, DMF were purchased from Sigma Aldrich and were used as received. Styrene (St) and N, N-dimethylaminoethyl methacrylate (DMAEMA) were passed through an Al_2O_3 column to remove inhibitors. Acrylic acid (AA) was distilled under vacuum before use. Azobis(isobutyronitrile) (AIBN) was recrystallized from ethanol. PEO_{45}-CTA, was synthesized by coupling poly(ethylene oxide) methyl ether (PEG_{45}-OH, molecular weight 2 $Kg \cdot mol^{-1}$) with 4-cyano-4-(phenylcarbonothioylthio)pentanoic acid (CPPA) through esterification according to our previously reported method.[75] Deionized water (Millipore Milli-Q grade) with resistivity of 18.0 MΩ was used in all the experiments.

2.2.2 Synthesis of thio-terminated BCPs

The thiol-terminated PEO-*b*-P(DMAEMA-*r*-St)-SH and PS-*b*-P(AA-*r*-St)-SH for modifying Au and Ag NPs, were synthesized separately using reversible addition fragmentation chain-transfer (RAFT) polymerization. The synthetic procedures are illustrated in Figure 2.2 (The synthetic routes of BCPs for modifying Fe_3O_4 NPs are shown in Figure 2.S1).

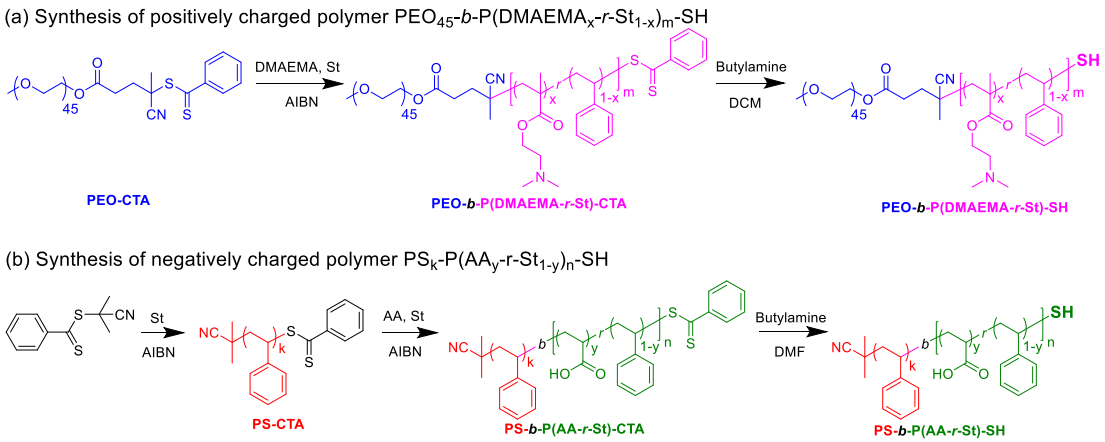

Figure 2.2 The synthetic routes of thiol terminated BCPs: (a) PEO-*b*-P(DMAEMA-*r*-St)-SH and (b) PS-*b*-P(AA-*r*-St)-SH.

2.2.2.1 Synthesis of PEO-b-P(DMAEMA-r-St)-SH.

BCPs of PEO-*b*-P(DMAEMA-*r*-St)-CTA were synthesized using PEO-CTA as the first block. Using PEO_{45}-*b*-$P(DMAEMA_{0.40}$-*r*-$St_{0.60})_{419}$-SH as an example, briefly, 0.2 g of PEO-CTA, 7.29 g of styrene, 4.76 g of DMAEMA and 1.64 mg of AIBN were mixed well in a 20 mL flask. The reaction mixture was degassed under vacuum for 10 min and refilled with Argon for 30 min. Then the flask was placed in an oil bath at 65 °C for 30 hours. After polymerization, the polymer was purified by precipitating in hexane and petroleum ether three times and dried under vacuum for 24 hours. To obtain thiol-terminated polymers, as-synthesized dithioester-terminated PEO-*b*-P(DMAEMA-*r*-St)-CTA were dissolved in DMF with excess of *n*-butylamine (50 eq.), and the mixture was stirred under nitrogen for 2 hours. The product was then precipitated in hexane three times to remove excess *n*-butylamine, and then dried under vacuum for 24 hours.

From the ^{1}H NMR spectrum (in $CDCl_3$, see Figure 2.S2), the ^{1}H NMR-based molecular weight M_n(NMR) is 54.5 Kg·mol^{-1}, by comparing the integrals of the resonance peaks of aromatic ring of PS block (6.4-7.3 ppm), the methylene groups of PEO-CTA (3.62-3.66 ppm) and methyl groups of DMAEMA block (0-1 ppm). By varying the amount of AIBN and reaction time, PEO-*b*-P(DMAEMA-*r*-St)-SH with different length and charge ratios were synthesized, as listed in *Table 2.1*.

2.2.2.2 Synthesis of macroRAFT chain transfer agent (PS-CTA)

Briefly, 66 mg of CPDB, 2.46 mg of AIBN and 15.6 g of Styrene were added into a 50 mL flask. The mixture was stirred under N_2 for 30 min, and then reacted at 85 ℃ for 23 hours. The polymer was precipitated in hexane 3 times and dried under vacuum for 24 hours. From the GPC curve (in THF, see Figure 2.S3), the GPC-based M_n is 27.9 Kg·mol^{-1}, and this polymer is determined to be PS_{267}-CTA.

2.2.2.3 Synthesis of thiol-terminated PS-b-P(AA-r-St)-SH

BCPs of PS-*b*-P(AA-*r*-St)-CTA were synthesized using PS-CTA as the first block. Briefly, 0.95 g of PS_{267}-CTA, 0.972 g of acrylic acid, 3.276 g of styrene, and 0.74 mg of AIBN were dissolved in 6 g of dioxane. The mixture was stirred under Argon for 30 min, and then reacted at 75 ℃ for 24 hours. The polymer was precipitated in hexane and petroleum ether 3 times and dried under vacuum for 24 hours.

To convert the terminal group from dithioester to thiol, PS-*b*-P(AA-*r*-St)-CTA was dissolved in DMF with excess n-butylamine (50 eq.), and the mixture was stirred under nitrogen for 2 hours. Then the mixture was transferred into an ice bath, with a dropwise addition of excess 37% HCl to neutralize and precipitate the product. The

polymer was then washed several times with water, to remove residual acid and salt, and was precipitated in petroleum ether twice and dried under vacuum for 24 hours. From GPC measurements (Figure 2.S4), the polymer sample has a M_n(GPC) of 57.7 Kg·mol^{-1}and a polydispersity index (M_w/M_n) of 1.07. From the ^{1}H NMR spectrum (in DMSO-*d6*, see Figure 2.S4), the molecular formula is PS_{267}-*b*-P($AA_{0.32}$-*r*-$St_{0.68}$)$_{318}$-SH. The parameters of PS-*b*-P(AA-*r*-St)-SH and other BCPs used in this chapter are listed in *Table 2.1*.

Table 2.1 Characterization of BCPs*.

sample	Compositions	Charge ratio	$M_{n,\ NMR/GPC}$ [c] (Kg·mol^{-1})	R_0 (nm)
P1	PEO_{45}-*b*-P($DMAEMA_{0.32}$-*r*-$St_{0.68}$)$_{98}$-SH	0.32	13.9	7.9
P2	PEO_{45}-*b*-P($DMAEMA_{0.41}$-*r*-$St_{0.59}$)$_{156}$-SH	0.41	21.6	9.9
P3	PEO_{45}-*b*-P($DMAEMA_{0.40}$-*r*-$St_{0.60}$)$_{419}$-SH	0.40	54.5	15.7
N1	PS_{90}-*b*-P($AA_{0.31}$-*r*-$St_{0.69}$)$_{273}$-SH	0.31	35.1	12.6
N2	PS_{111}-*b*-P($AA_{0.31}$-*r*-$St_{0.69}$)$_{289}$-SH	0.31	38.8	13.2
N3	PS_{140}-*b*-P($AA_{0.31}$-*r*-$St_{0.69}$)$_{279}$-SH	0.31	40.9	13.6
N4	PS_{267}-*b*-P($AA_{0.32}$-*r*-$St_{0.68}$)$_{318}$-SH	0.32	57.7	16.1

*: The molecular weight of PEO-*b*-P(DMAEMA-*r*-St)-SH is calculated from ^{1}H NMR measurements. The number-average molecular weight for PS-*b*-P(AA-*r*-St) is determined by GPC. Mean square end-to-end distance for PS block R_0 is calculated from $R_0=N^{0.5}b$, where *b* is the Kuhn length (*b*=1.8 nm for PS) and *N* is the number of Kuhn segments.

2.2.3 Synthesis of inorganic NPs

2.2.3.1 Synthesis of Au NPs

Au NPs with different sizes (~18, 24, 30, 36, 40 nm) were synthesized using methods previously reported.[75] Using 15 nm Au NPs as an example, 10 mg of $HAuCl_4$ was dissolved in 500 mL of water and heated to boiling under stirring. 10 mL of a sodium citrate solution (1% w.t.) was quickly added into the solution, and the solution was kept heating for 30 min. The 15 nm Au NPs were used as seeds for

further growth of larger Au NPs in the presence of sodium citrate at 90 °C. By varying the concentration of $HAuCl_4$, Au NPs with different diameters between 18 nm and 40 nm were obtained accordingly. Then the Au NPs were collected by centrifugation.

2.2.3.2 Synthesis of Fe_3O_4 NPs

Fe_3O_4 NPs of about 20 nm were synthesized according to previously reported protocol.[96] First, the precursor, iron oleate, was synthesized as follows: 5.4 g $FeCl_3{\cdot}6H_2O$ and 18.25 g NaOL were dissolved in a mixed solvent containing 40 mL ethanol, 70 mL hexane and 30 mL distilled water. The reaction mixture was stirred for 4h at 70 °C. Then the organic layer was extracted and washed three time with water, followed by the removal of organic solvents through rotary evaporator and drying under vacuum over 50 °C to obtain dry iron oleate. For the synthesis of Fe_3O_4 NPs, 9.0 g iron oleate, 1.4 g oleic acid, and 40 mL octadecene were mixed in a 250 mL 3-neck flask under stirring and protective Argon. The reaction temperature was elevated to 310 °C after 30 min and maintained for another 30 min. Afterwards, the reaction was cooled to room temperature. Fe_3O_4 NPs were precipitated by adding 500 mL of ethanol into the reaction solution. After purification, Fe_3O_4 NPs were dissolved in THF for further ligand exchange.

2.2.3.3 Synthesis of Ag NPs

Ag NPs with diameter around 20 nm were synthesized following procedures previously published after minor modification.[97] Briefly, a 2.0 mL of aqueous solution of sodium citrate (34.0 mM) was added into 2.5 mL of water under stirring, continuously followed with addition of 0.5 mL of an aqueous solution of $AgNO_3$

(29.7 mM) and 2 mL of aqueous solution of potassium iodide (3.0 μM). After 5 min incubation at room temperature, the mixture was injected into 95 mL of boiling aqueous solution of ascorbic acid, which was prepared by adding 1 mL of 10 mM ascorbic acid solution into 94 mL of pre-boiled water. The reaction solution was further boiled for another 1 h under strong stirring to form monodisperse spherical Ag NPs. To expand the library of inorganic building blocks, Ag NWs were also synthesized using methods previously reported with slight modification.[98] The SEM and TEM images for the inorganic building blocks can be found in Figure 2.S5.

2.2.4 Surface modification of Au NPs

Au NPs were grafted with thiol-terminated BCPs via ligand exchange through Au-S bond. Taking functionalization of 20 nm Au NPs with Lewis base-containing BCPs as an example, 15 mg of thiol-capped PEO-*b*-P(DMAEMA-*r*-St)-SH were dissolved in 10 mL of DMF in a 20 mL vial. 2 mL of Au NPs dispersed in DMF (~2 mg/mL) were slowly added into the above solution under sonication. Afterwards, the mixture was sonicated for 1 hour and incubated overnight to complete the ligand exchange. The polymer modified Au NPs were further purified via centrifuging with DMF and THF. The as-modified hybrid building blocks were redispersed in THF (~1 mg/mL) as a stock solution.

2.2.5 Co-assembly of BCPs modified Au NPs to form supracolloids

The assembly of supracolloids was triggered by mixing binary building blocks in a good solvent, i.e. THF. Due to the good solubility of both PEO and PS block in THF, the reaction of building block **A** and **B** was driven by the neutralization of the

Lewis acid and base containing block. Take the formation of AB for example, 1 mL of 20 nm **A** NPs (0.05 mg·mL^{-1}) were directly mixed with 1.7 mL of 24 nm **B** NPs (0.05 mg·mL^{-1}) in THF. The mixture was sonicated for 20 sec, and then incubated for 2 hr. The sample was imaged by SEM and TEM to statistically analyze the yield of supracolloids.

2.2.6 Sample preparation for characterizations

^{1}H NMR. ^{1}H NMR spectra were recorded using Bruker AV-400 MHz high resolution NMR spectrometer.

Gel Permeation Chromatography (GPC). GPC measurements were performed on a Waters GPC-a (1515 HPLC pump and Waters 717 Plus autoinjector) equipped with a Varian 380-LC evaporative light scattering detector and a Waters 2487 dual absorbance detector. PS standards were used for molecular weight and molecular weight distribution calibration, and THF was used as the elution solvent with a flow rate of 2.0 mL·min^{-1}. For PS-*b*-P(AA-*r*-St), the random block of AA and St was converted to poly(methyl acrylate-*r*-styrene) with trimethylsiyldiazomethane before measurement.

Thermogravimetric Analysis (TGA). TGA was used to characterize the grafting density of BCPs on the surface of the NPs. A 5.0 mL stock solution of building blocks was centrifuged to remove the supernatant, hexane was subsequently added, and the sample was centrifuged until a pellet formed. The pellets were dried in a vacuum oven for 24 h to remove the solvent residues before TGA measurement. The experiments were carried under argon, with a scan rate of 25 °C·min^{-1} from 25 °C to 1000 °C. During the scan process, the temperature was maintained at 100 °C for 30

min to further remove moisture. The weight fraction of polymer ligands *f* was determined by using the TA Universal Analysis software package.

Zeta potential. The zeta potential of hybrid building blocks and supracolloids were measured using ZetaPALS (Brookhaven Instruments Corporation, USA).

Dynamic Light Scattering (DLS). DLS measurements for hybrid building blocks and supracolloids were conducted on Zetasizer Nano-ZS system (Malvern), equipped with a He-Ne 633 nm laser as the light source.

UV-vis Absorption Spectroscopy. Absorbance measurements of samples was conducted in a PERKIN LAMBDA 35 UV/vis system.

SEM and TEM imaging. The morphologies of assemblies were obtained using a Hitachi SU-70 Schottky field emission gun Scanning Electron Microsccope (FEG-SEM) and a JEOL FEG Transmission Electron Microscope (FEG-TEM). Supracolliodal samples for SEM and TEM analysis were prepared by depositing ~10 μL of solution on silicon wafer and 300 mesh copper grids covered with carbon film, respectively. The samples were dried at room temperature before imaging measurement.

2.3 Results and discussion

2.3.1 Hybrid building blocks

Figure 2.1 illustrates the structure of binary hybrid building blocks. The grafted BCPs are designed to have two functional blocks in which the outer PEO or PS blocks provide both building blocks and final supracolloids with extra steric stabilization, while the inner random block consisting of styrene and a reactive proton donor/acceptor moiety enables the controlled association of complementary disparate

NPs via stoichiometric reaction between–COOH and $–NMe_2$. Such hybrid building blocks can be considered as analogies of giant spherical Lewis polyacids and polybases during the self-assembly. Here Lewis base containing Au NPs, with a hydrophilic outer layer of PEO, are shown as blue particles (denoted as **A**), and Lewis acid containing Au NPs, coated with a hydrophobic outer layer of PS, are represented by red particles (denoted as **B)**. The size of Au NPs was expressed by the subscript. For instance, $\mathbf{A_{20}}$ represents 20 nm Au NPs capped with polymer P3, while $\mathbf{B_{24}}$ represents 24 nm Au NPs capped with polymer P4 (P3 and P4 are the polymers used most frequently in this chapter, **A** and **B** capped with BCPs other than these two polymers will be specially explained). UV-vis spectroscopy was used to characterize the Au NPs before and after the surface modification, based on the direct correlation of absorption bands and aspect ratio of Au NPs. After the grafting of BCPs on NP surfaces, a slight red-shift (~6 nm) of was observed for both $\mathbf{A_{20}}$ and $\mathbf{B_{24}}$, which indicates an increase on particle size due to the capped polymer layer on the surface of Au NPs (Figure 2.3).

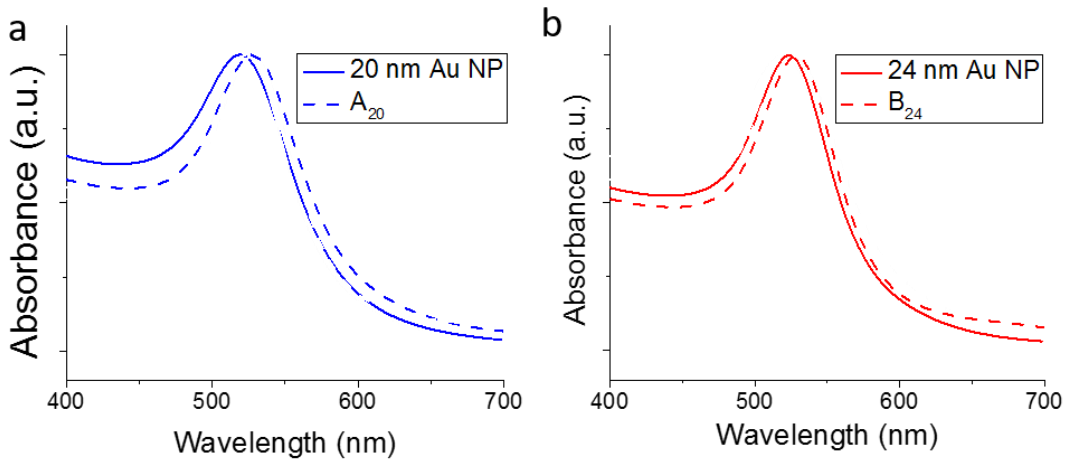

Figure 2.3 UV-vis spectrum of Au NPs before and after surface modification. (a) UV-vis spectrum of 20 nm Au NPs in aqueous solution and **A_{20}** in THF. (b) UV-vis spectrum of 24 nm Au NPs in aqueous solution and **B_{24}** in THF.

TGA was performed to quantify the amount of grafted polymers on NPs (Figure 2.4). Take **A_{20}** as an example, the weight loss was observed at elevated temperatures above 200 °C, due to the thermal degradation of BCPs into volatile products. Based on the measured weight of grafted polymers, the grafting density (σ) of polymers on NPs was estimated using the following formula: [73]

$$\sigma = \frac{f \times N_A \times \rho \times d}{6 \times M_n \times (1 - f)} \quad \text{Equation 1}$$

Where f is the weight fraction of the polymer determined by TGA, N_A is the Avogadro's constant, ρ is the bulk density of the NP core (the formula is under the assumption that the density of Au NPs is identical to the density of the bulk gold), d is the diameter of Au NP core, and M_n is the number-average molecular weight of the BCPs determined by GPC. From the TGA measurement, **A_{20}** and **B_{24}** showed a weight loss of 10.48% and 9.15%, respectively. Following the abovementioned

procedures, σ of polymers was calculated to be 0.0833 chain/nm^2 and 0.0812 chain/nm^2. It is well known that σ plays an important role on the conformation of polymer chains. From the calculated σ, the average distance (l) between adjacent ligand anchoring point can be estimated by assuming the effective footprint of each individual polymer chain is a circular area with a radius equal to half of the distance between adjacent chains. The l between polymer ligand on **A_{20}** and **B_{24}** is estimated to be 3.91 nm and 3.96 nm, respectively. The radius of gyration for each corresponding BCPs can be calculated using the formula $R_g=(R_0^2/6)^{1/2}$ (R_0 can be found in table 2.1). The ratio of R_g/l is estimated to be in the range of 1.6 to 1.7, which suggests that the BCPs on Au NPs adopt a mostly flexible "brush" conformation (Figure 2.S6). [99] The polymer chains extend far away from the particle surface to avoid steric overcrowding. In the vicinity of the particle surface, the polymer brushes are expected to take a more stretched conformation, which will become more relaxed with increasing distance from the surface. This conformation facilitates the interpenetrations of complementary BCP brushes from neighboring Au NPs and deformation of flexible brushes, which benefits the interparticle reactions.

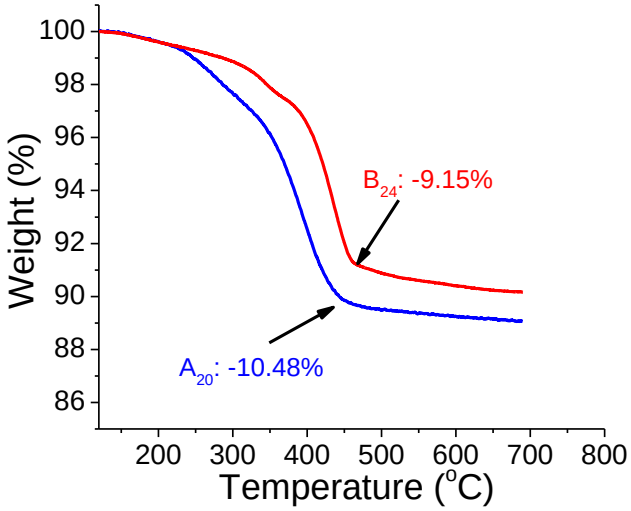

Figure 2.4 TGA curves of hybrid building block **A_{20}** and **B_{24}**.

A series of hybrid building blocks with different sized Au NPs were produced and used in the construction of supracolloids (see characterization of size and charge in Table 2.2). The zeta potential analysis shows a negative charge for building block **B** (i.e., Au NPs tethered with PS-*b*-P(AA-*r*-St)-SH) dispersed in THF. This can be explained by the proton transfer between carboxylic moiety of BCPs and citric acid originally on the surface of NPs during the ligand exchange in THF solvent. It is interesting that the zeta potential of **A** (i.e., Au NPs tethered with PEO-*b*-P(DMAEMA-*r*-St)-SH) is close to zero. This can be attributed to the suppressed protonation of amine group in organic solvent. The hybrid building blocks all exhibit a larger size compared with the size of Au NPs in aqueous solution, which suggests a successful modification of polymer brushes on Au NPs.

Table 2.2 Zeta potential and hydrodynamic diameter of hybrid building block A and B.

Hybrid Building blocks	Zeta potential (mV)	Hydrodynamic diameter (nm)	PDI
$\mathbf{A_{20}}$	4.75±1.99	63.98	0.372
$\mathbf{A_{24}}$	0.04± 3.49	75.12	0.032
$\mathbf{A_{30}}$	1.19±0.62	82.47	0.166
$\mathbf{A_{36}}$	0.72±2.62	83.54	0.142
$\mathbf{B_{18}}$	-68.9±3.63	65.01	0.245
$\mathbf{B_{24}}$	-58.3±7.93	67.35	0.271
$\mathbf{B_{30}}$	-56.1±7.91	79.22	0.156
$\mathbf{B_{36}}$	-63.9±5.50	88.37	0.1

2.3.2 Amphiphilic supracolloids

Co-assembly of **A** and **B** in THF produced different types of amphiphilic supracolloids in high yield. The type of supracolloids is determined by the NP sizes, and feeding ratio of **A** and **B**. For example, the co-assembly of $\mathbf{A_{20}}$ and $\mathbf{B_{24}}$ at a

number ratio ~ 1:1 generated **AB** dimers as the major supracolloids (Figure 2.5). As shown in the statistical analysis in Figure 2.5c, the yield of dimers was above 70% without any purification. This purity is higher than that obtained by any methods previously reported. (The highest yield of Au dimers obtained from previously reported work was around 60%, by a complicated solid phase approaches, polymer encapsulation approach or DNA origami assisted approach after intricate purification process.)[100]

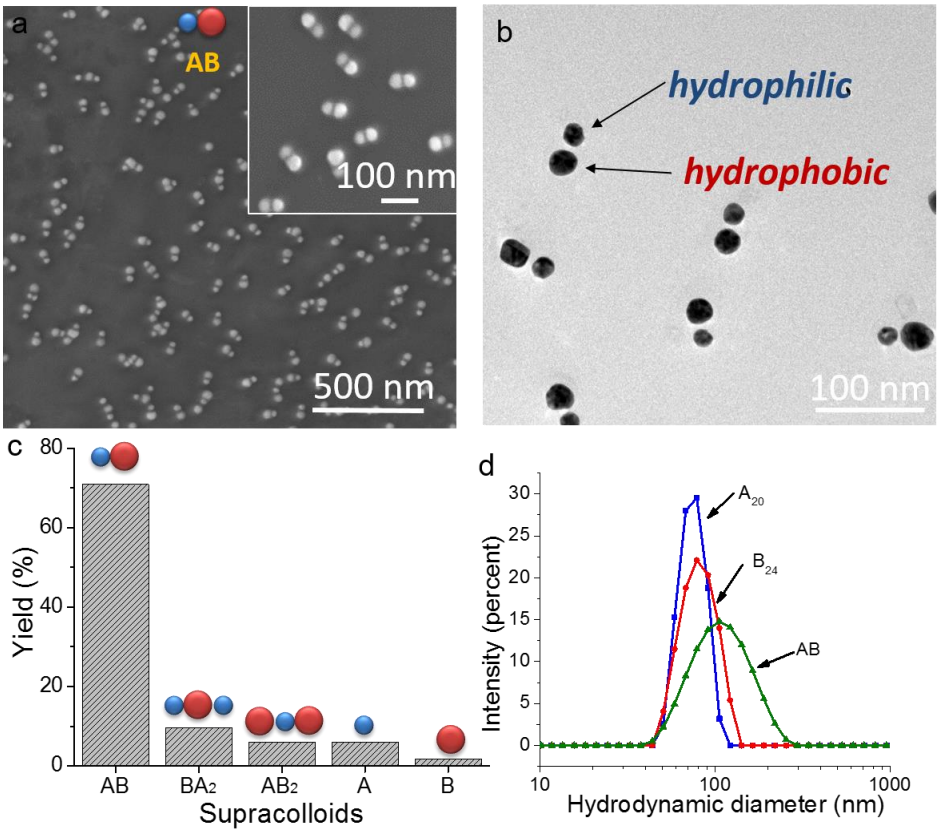

Figure 2.5 Supracolloidal dimers (**AB**) formed from $\mathbf{A_{20}}$ and $\mathbf{B_{24}}$. Representative SEM (a) and TEM (b) image of dimer **AB** after the reaction between $\mathbf{A_{20}}$ and $\mathbf{B_{24}}$. The parameters of the building blocks were summarized in Table 2.3. (c) Yield distribution of supracolloids generated by mixing $\mathbf{A_{20}}$ and $\mathbf{B_{24}}$. (d) Hydrodynamic diameters of $\mathbf{A_{20}}$, $\mathbf{B_{24}}$ and dimer **AB**.

The interparticle distance between NPs in dimers is measured to be ~8.6±2.0 nm which explains the slight red-shift on UV-vis spectrum (See Figure 2.S7a). The hydrodynamic diameter before and after assembly monitored by DLS (Figure 2.5d) and zeta potential (Figure 2.S7) also indicates that the reaction occurred in THF instead of during the drying process.

This versatile method allows for the preparation of supracolloids with tunable parameters by varying the size of NP cores, as well as the feeding ratio of building blocks (BCPs for **A** and **B** were fixed to be P3 and N4 polymer). At the same feeding ratio of **A** and **B**, tuning the size of Au NPs generates dimers with different domain size (Figure 2.6a-c). It is worth noting that the supracolloids are amphiphilic with **A** capped with hydrophilic outlayer polymer block (blue particle) and **B** capped with hydrophobic outlayer polymer block (red particle). By tuning the feeding ratio, supracolloidal trimers with two NPs bonded to the opposite sites of one central NP were produced. In our system, further tuning the number ratio of **A/B** creates a series of trimers such as $\mathbf{AB_2}$ and $\mathbf{BA_2}$. When the feeding ratio **A/B** is around 1:2, $\mathbf{AB_2}$ structures were formed with a hydrophilic center **A** and two hydrophobic ends **B**, as shown in Figure 2.6e-g. However, when the concentration of **A** NPs is twice that of the **B** NPs, the assembly produced $\mathbf{BA_2}$-type trimers with a hydrophobic center **B** and two hydrophilic ends **A** (Figure 2.6 i-k). These plasmonic trimers are expected to show remarkable optical properties.[101]

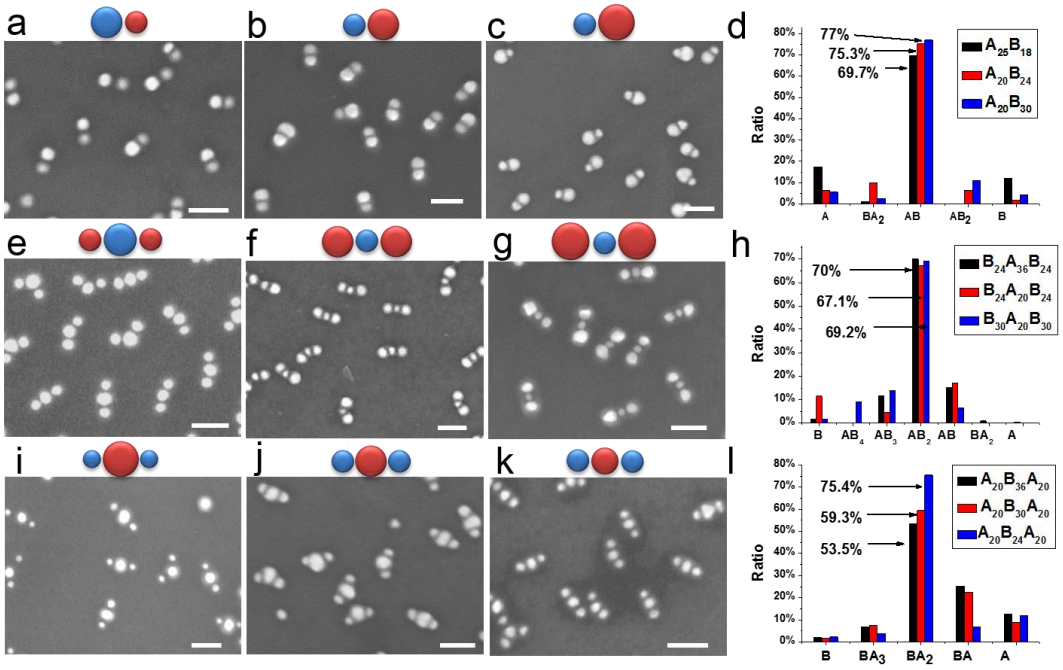

Figure 2.6 Amphiphilic supracolloids formed by **A** and **B** NPs with different size. (a-c) SEM images of **AB** formed from $\mathbf{A_{25}}$ and $\mathbf{B_{18}}$ (a), $\mathbf{A_{20}}$ and $\mathbf{B_{24}}$ (b), and $\mathbf{A_{20}}$ and $\mathbf{B_{30}}$ (c). (e-g) SEM images of $\mathbf{AB_2}$ formed from $\mathbf{A_{25}}$ and $\mathbf{B_{36}}$ (e), $\mathbf{A_{20}}$ and $\mathbf{B_{24}}$ (f), and $\mathbf{A_{20}}$ and $\mathbf{B_{30}}$ (g). SEM images of $\mathbf{BA_2}$ formed from $\mathbf{A_{20}}$ and $\mathbf{B_{36}}$ (i), and $\mathbf{A_{20}}$ and $\mathbf{B_{30}}$ (j), and $\mathbf{A_{20}}$ and $\mathbf{B_{24}}$ (k). Scale bar: 100 nm. (d,h,l) Yield distribution of **AB**, $\mathbf{AB_2}$, and $\mathbf{BA_2}$ respectively.

For all the supracolloids, the yield of the major product all reach around 70% or higher, this high-yield qualifies the pristine product being used as building blocks again for the further self-assembly to hierarchical superstructures. Supracolloidal molecules of a yield above 86% have been achieved after optimization of polymers in a separated project in the group, which is not the focus of this project. According to the theory in that work, high yield supracolloids could be achieved when the overall

functional group ratio of **A** and **B** compensates each other. However, in current system, we can always obtain high yield of supracolloids. This is mainly attributed to the long PS block on **B** particle, which functions as a buffer outer shell to protect the untreated Lewis acid/base containing block in the inner layer. When the Lewis acid-containing block on **B** is not fully reacted with Lewis base blocks on **A** NPs, the residue reactive brushes can be stabilized when protected by the thick PS shell. Upon the formation of supracolloids, the overall zeta potential (initially ~ – 60 meV for **B**) significantly increased (final~ –14 meV for **AB**, ~ –20 meV for $\mathbf{AB_2}$ and ~0 meV for $\mathbf{BA_2}$), indicating the assembly of supracolloids in solutions. The increase in the hydrodynamic diameter of particles in assembly system before and after assembly further confirmed the formation of supracolloids in THF (see Table 2.3).

Table 2.3 Zeta potential and hydrodynamic diameter of supracolloids **AB**, $\mathbf{AB_2}$, $\mathbf{BA_2}$.

Building blocks	Mobility ($\mu m \cdot cm \cdot V^{-1} \cdot s^{-1}$)	Zeta potential (mV)	Hydrodynamic diameter (nm)	PDI
a: $\mathbf{A_{25}\,B_{18}}$	-0.2003±0.04686	-13.7±8.8	103.5	0.217
b: $\mathbf{A_{20}\,B_{24}}$	-0.2122±0.04259	-14.5±2.9	91.46	0.2
c: $\mathbf{A_{20}\,B_{30}}$	-0.2085±0.1070	-14.2±7.3	107.3	0.158
d: $\mathbf{B_{24}A_{36}B_{24}}$	-0.2799±0.03353	-19.1±2.3	176.7	0.211
e: $\mathbf{B_{24}A_{20}\,B_{24}}$	-0.2939±0.04222	-20.1±2.9	114.0	0.178
f: $\mathbf{B_{30}A_{20}\,B_{30}}$	-0.3486±0.09017	-23.8±6.2	127.3	0.161
h: $\mathbf{A_{20}B_{36}\,A_{20}}$	0.02179±0.04052	1.5±2.8	178.2	0.157
i: $\mathbf{A_{20}B_{30}\,A_{20}}$	-0.06249± 0.04246	-4.3±2.9	135.6	0.085
j: $\mathbf{A_{20}B_{24}\,A_{20}}$	-0.03349 ± 0.007722	-2.3±0.5	111.5	0.176

Supracolloids with higher valance were also obtained by tuning the length of each BCP and the size of NPs. As shown in Figure 2.7, tetramers **($\mathbf{BA_3}$** and $\mathbf{AB_3}$) and

pentamers (**BA_4** and **AB_4**) with tunable surface chemistry (i.e., the relative location of hydrophilic and hydrophobic domains) were created by varying building block parameters (see parameters in Table 2.S1). With the decrease length of PS block on **B** particle, the supracolloids **AB_3** and **AB_4** were obtained, due to weaker steric repulsion from the long PS block on **B** particles. With the decrease length of BCPs on **A** particle, **BA_3** and **BA_4** were obtained, resulting from the shorter Lewis base containing block on **A** particles consuming less Lewis acid block on **B** particles. These supracolloids with higher valence also appear with symmetric geometry, tetramers mostly showed trigonal planar shape, and pentamers mostly had planar square morphology, which is risen from the directional interactions between A and B. The tetramer and pentamer structures would be of great interest in the development of negative index metamaterials.[102]

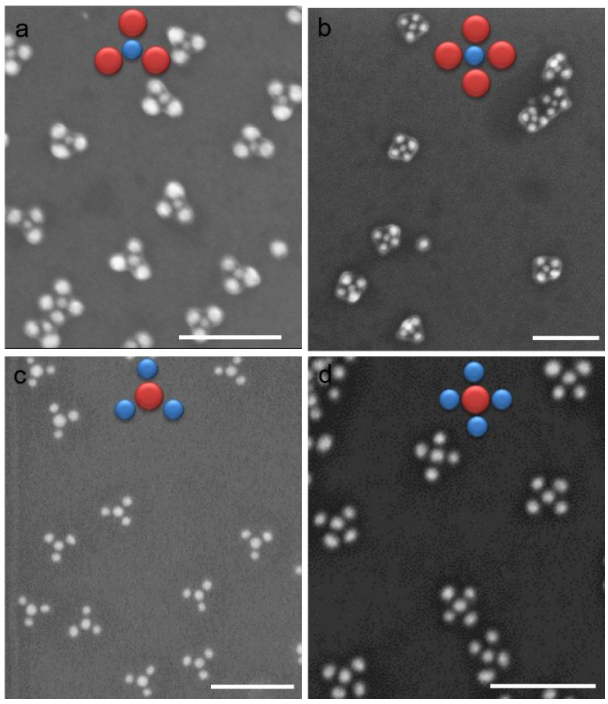

Figure 2.7 Supracolloids tetramers and pentamers formed from **A** and **B**. (a-d) Representative SEM images of **AB_3**, **AB_4**, **BA_3**, **BA_4**, respectively. Scale bar: 200 nm.

It is interesting that these supracolloids are highly symmetric in geometry, resembling symmetric (or non-polar) biomolecular compounds, such as CO_2, BF_3, and XeF_4. This also means that the hydrophilic or hydrophobic polymeric patches (defined by the outer block of BCPs on **A** or **B**) are arranged with high symmetry. For instance, the above trimers all exhibit a linear arrangement of Au NPs, which is likely attributed to the directional interactions between opposite binary NPs, as illustrated in Figure 2.8. Based on the zeta potential we measured, **B** particles carry negative charge from the $-COO^-$ group, **A** particles are nearly neutral in THF. When **A** and **B** were mixed, the collision among particles created the bonding between **A** and **B**. After the binding of one **B** particle with **A** particle, part of the unreacted charges on **B** was relocated to the gap between **A** and **B**. When another **B** particle was bonded from other direction, the residual charges from the second **B** particle would be distributed to another gap. The repulsive interaction between two 'clouds' of charges pushes the two particles symmetrically distributed at opposite side of the central particle, which leads to the formation of linear trimers..

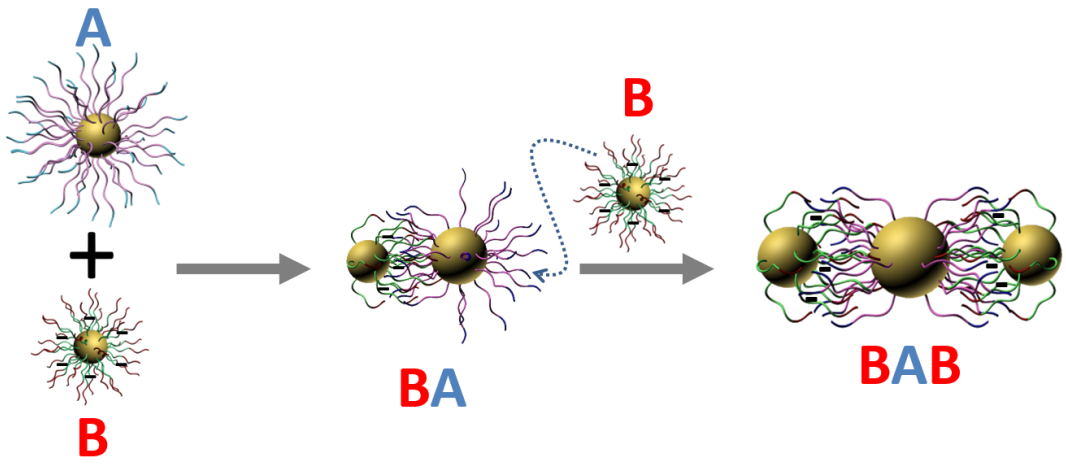

Figure 2.8 Scheme of forming linear trimer.

2.3.3 Multi-component supracolloids

Compositionally heterogeneous supracolloids were also readily synthesized, by simply replacing Au NP cores with other inorganic NPs, such as Ag or iron oxide (Fe_3O_4). Figure 2.9 (a-b) show the TEM images and the corresponding element mapping of trimers and tetramers from Au and Ag NPs. Similarly, co-assembly of Au NPs and Ag NWs were also obtained by replacing Au NP cores with Ag NWs, as shown in Figure 2.S8. For the surface modification of Fe_3O_4 NPs, phosphonate terminated hydrophobic BCPs were utilized to replace the anchoring group thiol for Au NPs. See the synthetic route of the phosphonate terminated BCPs in Figure 2.S1. As a result, dimers and trimers of Au and Fe_3O_4 NPs were obtained, as shown in Figure 2.9c-d. With rational design of reactive BCPs and control of assembly conditions, it is conceivable to expand the family of supracolloids by integrating other metallic or oxide NPs into the supracolloids.

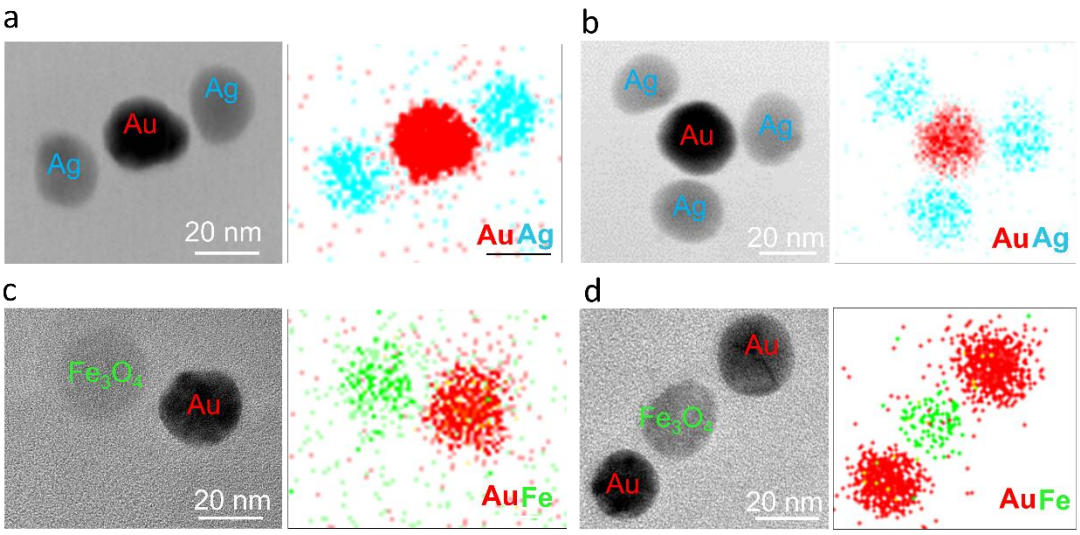

Figure 2.9 Compositional heterogeneous supracolloids formed by co-assembly of Au NPs and Ag NP or Fe_3O_4 NPs. (a) TEM and elemental mapping of trimers formed by

two terminal Ag NPs and one central Au NPs. (b) TEM and elemental mapping of tetramers formed by three surrounding Ag NPs and one central Au NPs. (c) TEM and elemental mapping of dimers formed by Fe_3O_4 NPs and Au NPs. (d) TEM and elemental mapping of trimers formed by two terminal Au NPs and one central Fe_3O_4 NPs.

2.3.4 pH-responsive of building blocks to form alternating chains

The hybrid building blocks also show pH responsiveness during self-assembly, originating from complementary reactive moieties –COOH and $–NMe_2$. Utilizing the parameters to form dimers, adding a trace amount of acetic acid (5/1000 vol. ratio) into the system led to the formation of alternating chains in which the dimers behavior like dipoles to connect with each other in a head-to-tail manner. We presume that the addition of acid triggers the protonation of the reactive blocks, which largely reduces the stability of formed dimers. Therefore, the more reactive end will further grow into long chains upon collisions. Figure 2.10 displays the alternating chains formed by a combination of **A** and **B** with the parameter of building blocks shown in Table 2.S1.

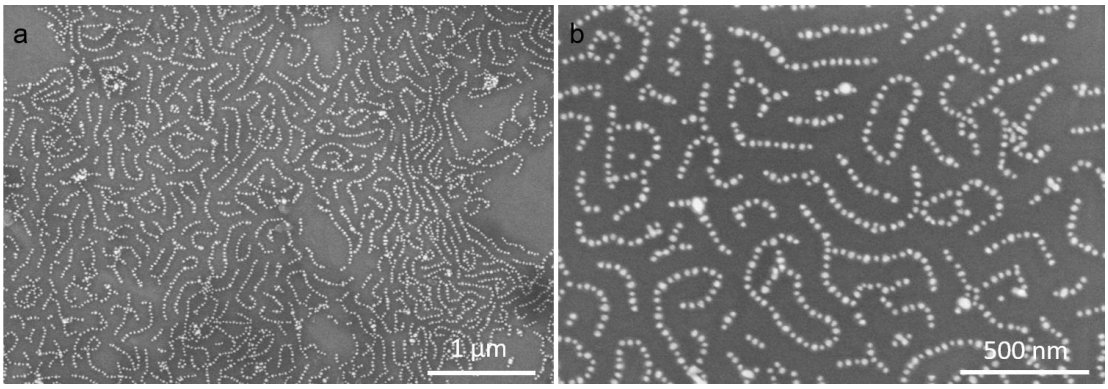

Figure 2.10 SEM images of alternating chains formed by adding acid to **A** and **B**.

When the size of Au NPs increases, NP shape turns into more irregular because of the presence of random crystal facets. The irregular shape (vs. spherical) of NPs induces the formation of kinks (or curvatures) of alternating chains (Figure 2.11). The angle of the non-spherical NPs (θ_P) and the curvature of the alternating chains (θ_c) were quantitatively analyzed. The statistical analysis on the dependency of θ_c on θ_P implies that a majority of points (87.4%) fall into the range between a fit of y = x and y = 2x, which means the curvature of chains is amplified by the angle of the non-spherical NPs.

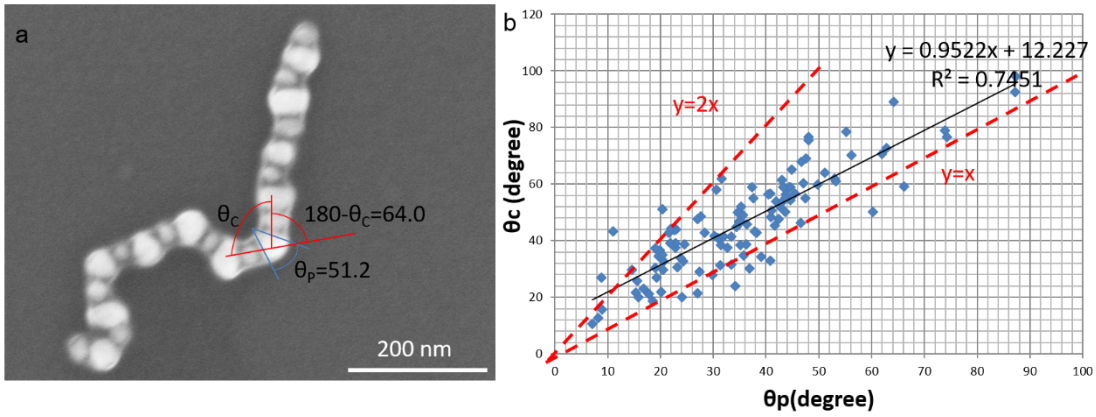

Figure 2.11 Relationship of the curvature of chain and the shape of NP. (a) SEM image of an alternating chain formed by $\mathbf{A_{40}}$ and $\mathbf{B_{25}}$. The angle of the non-spherical NPs and the curvature of the alternating chains are illustrated in the image. (b) Chain angle dependency on the particle angle.

2.4 Conclusion

In this Chapter, we demonstrated the generation of various supracolloids with defined valences by tethering Au NPs with complementary reactive BCPs. Tunable domain sizes and various valences were realized by tuning the size of Au NPs and the

length of BCPs. The obtained supracolloids all feature high yields and symmetric geometries, which qualify these structures as building blocks in further self-assembly. The heterogeneous chemical composition of supracolloids was also achieved by replacing one type of Au NP with Ag or Fe_3O_4 NP, which largely expanded the diversity of supracolloids. Such colloidal molecules are of great scientific importance in designing directional and specific interaction between NPs, and can serve as building blocks for hierarchical superstructures in plasmonic devices, such as LSPR and SERS sensing and single molecule detection.[2]

Chapter 3: Self-assembly of nanoscale amphiphilic supracolloids constructed from binary nanoparticles at the liquid/liquid interface

Overview. Controlled assembly of NPs into ensembles with increased complexity and hierarchy is crucial to the property discovery and application development of inorganic NPs. Despite tremendous efforts made in the past several decades, little progress has been achieved in the controlled assembly of NPs into structures with multiple hierarchy levels. Herein, we developed a novel strategy to achieve step-wise assembly of NPs into a class of well-ordered superstructures by tethering NPs with designed BCPs. In the first level assembly, a series of amphiphilic supracolloids with well-defined valance and chemical patches were fabricated in high yields by co-assembling a combination of binary hybrid building blocks (chapter 2). The amphiphilic supracolloids were demonstrated to assemble into a variety of defined structures with tunable optical properties. This step-wise assembly strategy provides a robust and efficient way to generate highly ordered superstructures that are not readily achieved through traditional approaches.

A manuscript based on this chapter and chapter 2 is in preparation and to be submitted to *Nature Material*.

3.1 Introduction

Throughout the history of self-assembly, researchers have drawn inspiration from the natural world, where vast arrays of ubiquitous and functional materials have been produced through hierarchical organization of molecular or colloidal building blocks.[1a, 103] In man-made system, the multi-step assembly of molecules has been demonstrated for the preparation of complex structures. For instance, BCPs can be

designed to assemble into patchy or blocked micelles in which defined chemical patterns provide directional interaction to guide their further assembly at a higher hierarchy level.[104] Despite the molecular design over polymer composition allows fascinating control over the spatial organization, these soft assembly structures usually do not possess unique physical and chemical properties of their inorganic counterparts.

To achieve precise or multi-step assembly of NPs, one commonly-adopted concept is to encode NPs with directional or anisotropic interaction patterns by site-specific functionalization of NPs with chemical patches or defined number of molecules (e.g., DNA). For example, Pine *et al.* uncovered a new direction of creating "patchy" particles via encapsulating PS clusters using a two-stage swelling and polymerization approach. The spatial patches were subsequently decorated with DNA oligomers to introduce specific interactions between patchy particles.[95a] In this work, colloidal molecules, that mimic atomic bonding in molecules, were fabricated via complementary nucleic interaction of patches on the NP surface. Although intelligent is design, this strategy still requires further purification process to separate particles with different patchy number, and the size of patchy particles were limited to micro-size. Another solution to endow chemical patch is modifying NPs with controlled number of ligands on particle surface. For instance, CdTe NPs capped with varying number of DNA sequences were formed in a one-pot process, the number of DNA on NPs were controlled by varying the length of the quantum dot binding domain. The combination of CdTe NPs with different DNA sequence led to the formation of quantum dot complexes with various valence.[81]. Despite the initial

success of patchy particles, the site-specific functionalization of particles remains challenging, specifically for nanoscale particles with size below 100 nm. Nevertheless, there remains a grant challenge to organize man-made colloidal particles in a way that mimics assembly pathways observed in nature.

Here we report the assembly of amphiphilic supracolloids, which are constructed from binary NPs, to form defined structures at a higher hierarchy level. The step-wise assembly of NPs relies on the design of BCP ligands on the surface of NPs in such a way that each block responds specifically to one stimulus at a specific stage. In detail, the BCPs were designed to have a random block consists of styrene and a proton donor/acceptor moiety, which provide the Lewis acidity/basicity with tunable ratios to trigger the first stage of assembly of forming supracolloids. The second PEO or PS blocks of the BCPs was designed to protect both hybrid NPs and finally-formed supracolloids by providing extra steric stabilization. Moreover, they define the anisotropic surface chemistry (hydrophobic/hydrophilic) of the obtained supracolloids, which triggers specific interactions between supracolloids in second step assembly. As shown in Figure 3.1, level one assembly was construction of amphiphilic supracolloids from hybrid building blocks **A** and **B**, as described in Chapter 2, obtained structures include amphiphilic dimers (**AB**) or trimers (**BAB** and **ABA**). Therefore, the amphiphilic supracolloids were able to serve as building blocks for the next stage of assembly. The second step assembly was triggered by changing the solvent quality of supracolloids at liquid-liquid interface, where hydrophobic interactions, induced by the PS block on the B particles, are utilized to trigger the association of supracolloids. At this stage, we assembled the dimers into petal-like

structures, with a tunable number of petals **(AB)$_N$**, and the trimers into either ribbon structures **(ABA)$_N$** from side-by-side stacking of **ABA** or chain structures **(BAB)$_N$** from end-to-end connection of **BAB**.

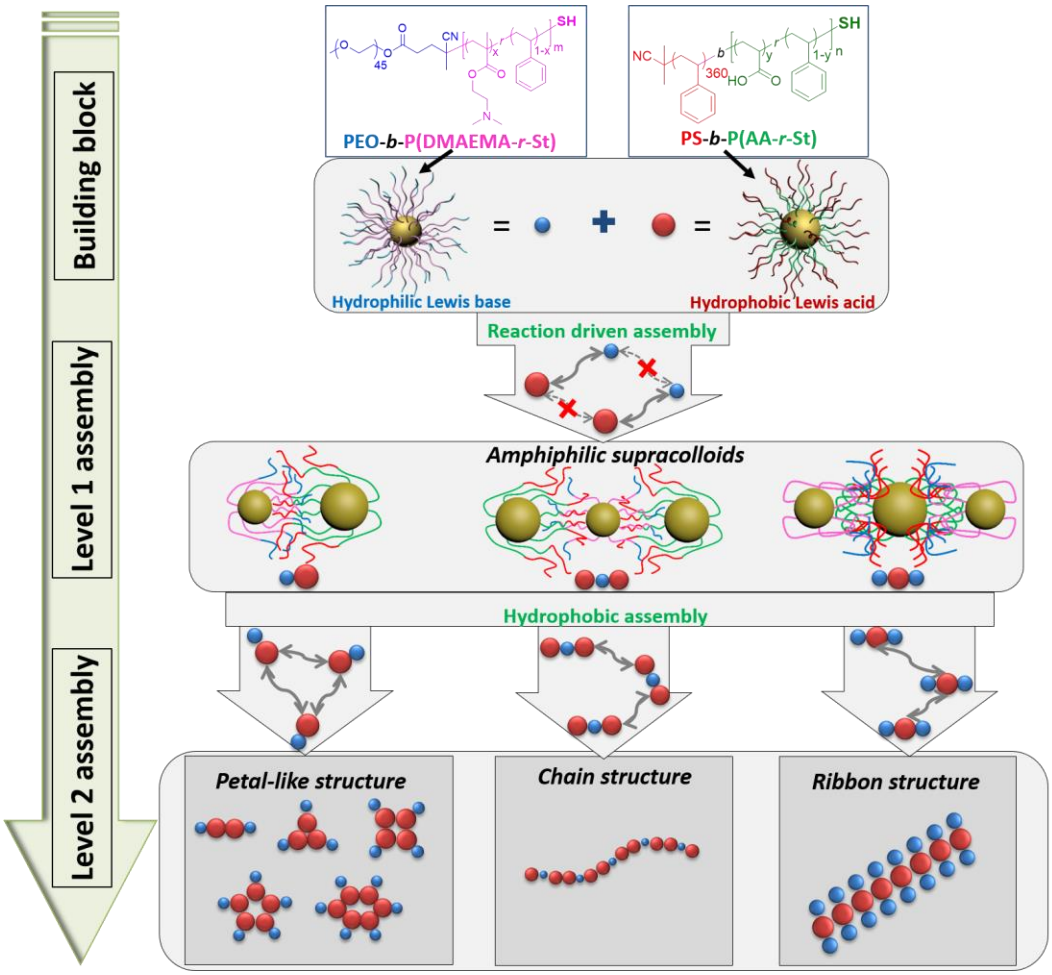

Figure 3.1 Scheme of hierarchical assembly of amphiphilic supracolloids.

3.2 Experiments

3.2.1 Materials

BCPs PEO-*b*-P(DMAEMA-*r*-St)-SH and PS-*b*-P(AA-*r*-St)-SH, Au NPs with diameter ranging from 18 to 36 nm were synthesized by the same method described in Chapter 2. The length and symbol for BCPs can be found in Table 2.1.

Hydrochloric acid (36.5-38.0%), sodium chloride were purchased from Sigma Aldrich and used as received unless otherwise noted. Deionized water (Millipore Milli-Q grade) with resistivity of 18.0 MΩ was used in all the experiments.

3.2.2 Preparation of hybrid building blocks

The preparation of hybrid building blocks is referred to experimental section in Chapter 2 (section 2.2.2−2.2.4).

3.2.3 Level-1 assembly: Preparation of amphiphilic supracolloids

Assembly of BCP tethered Au NPs was triggered by mixing binary building blocks in THF. Due to the good solubility of both PEO and PS block in THF, the reaction of building block **A** and **B** was driven by the neutralization of Lewis acid and base containing block, so only particles carrying opposite acidity and basicity can react with each other during collision. Take the formation of AB as example, 1 mL of 20 nm **A** NPs (0.05 mg·mL^{-1}) direct mix with 1.7 mL of 24 nm **B** NPs (0.05 mg·mL^{-1}) in THF. The mixture was sonicated for 20 sec, and then incubated 2 hr. The sample was imaged by SEM and TEM to analyze statistically the yield of supracolloids.

3.2.4 Level-2 assembly: Liquid-liquid interfacial assembly of supracolloids

The assembly of amphiphilic supracolloids (2nd step assembly of inorganic NPs) was performed at liquid-liquid interface. Briefly, 1 mL of supracolloids dispersed in THF was placed on top of a mixture of 4 mL of saturated sodium chloride solution and 1 mL of 1M HCl aqueous solution. An interface was formed between two liquids due to the incompatibility of THF and dense salt solution. As a poor solvent for the PS blocks of B particles, the aqueous phase triggered the

hydrophobic force and drove the red particles to associate with each other. Then the mixture was capped and incubated until all of the THF was evaporated. Afterwards, a film of ensembles was floating on the surface of salt solution. The liquid-liquid interfacial assembly is shown in Figure 3.2.

3.2.5 Dissipative particle dynamics (DPD) simulation

Simulation was performed by our collaborator to understand the system. Dissipative particle dynamics (DPD) simulation technique was proven to be a suitable and efficient method in the studies of self-assembly of NPs. In DPD method, the time evolution of the interacting coarse-grained (CG) beads is governed by Newton's equations of motion[105]

$$\frac{d\vec{r}_i}{dt} = \vec{v}_i, \quad \frac{d\vec{v}_i}{dt} = \sum_{j \neq i} (\vec{F}^C{}_{ij} + \vec{F}^D{}_{ij} + \vec{F}^R{}_{ij}) = \vec{f}_i \qquad (1)$$

Inter-bead interactions are characterized by pairwise conservative, dissipative, and random forces. They are

$$\vec{F}^C{}_{ij} = \alpha_{ij}(1 - r_{ij}/r_c)\vec{e}_{ij}, \quad \vec{F}^D{}_{ij} = -\gamma w^D(r_{ij})(\vec{e}_{ij} \cdot \vec{v}_{ij})\vec{e}_{ij}, \quad \vec{F}^R{}_{ij} = \sigma w^R(r_{ij})\theta_{ij}\vec{e}_{ij} \qquad (2)$$

Here, $\vec{r}_{ij} = \vec{r}_i - \vec{r}_j, r_{ij} = |\vec{r}_{ij}|, \vec{e}_{ij} = \vec{r}_{ij}/r_{ij}$, r_c is the cutoff radius, and $\vec{v}_{ij} = \vec{v}_i - \vec{v}_j$. θ_{ij} is a random number with Gaussian distribution and unit variance. α_{ij} is the interaction parameter between beads *i* and *j*. The weight functions $w^D(r_{ij})$ and $w^R(r_{ij})$ of dissipative and random forces couple together to form a thermostat. Español and Warren showed the correct relation between the two functions,[106]

$w^D(r_{ij}) = [w^R(r_{ij})]^2$, $\sigma^2 = 2\gamma k_B T$.

DPD-VV algorithm is used for numerical integration,[2] i.e.

$$\begin{aligned}
&\vec{v}_i \leftarrow \vec{v}_i + \frac{1}{2}\frac{1}{m}(\vec{F}_i^C \delta t + \vec{F}_i^D \delta t + \vec{F}_i^R \sqrt{\delta t}) \\
&\vec{r}_i \leftarrow \vec{r}_i + \vec{v}_i \delta t \\
&Calculate\ \vec{F}_i^C(\vec{r}), \vec{F}_i^D(\vec{r}_i, \vec{v}_i^0), \vec{F}_i^R(\vec{r}) \\
&\vec{v}_i \leftarrow \vec{v}_i + \frac{1}{2}\frac{1}{m}(\vec{F}_i^C \delta t + \vec{F}_i^D \delta t + \vec{F}_i^R \sqrt{\delta t}) \\
&Calculate \vec{F}_i^D(\vec{r}_i, \vec{v}_i)
\end{aligned} \quad . \qquad (3)$$

In this work, we adopte x particles for the bigger Au NPs and y particles for the smaller Au Ps to form the composite system A_xB_y, $(A_x)_2B_y$, $A_x(B_y)_2$ in which m=x+y CG beads form a spherical rigid body[107]. We simulate the hierarchical assembly of amphiphilic supracolloids by dissipative particle dynamics (DPD)[108], using a coarse-grained (CG) model in our previous work[109]. To map onto the experimental systems, we choose an appropriate coarse-graining level for Au NPs and solvents C and solvents D. The interaction α_{AB}=46-52, $\alpha_{AC}=\alpha_{AD}=\alpha_{BC}=\alpha_{BD}$=50, α_{CD}=100, α_{AA}=40/0, α_{BB}=0/40 and $\alpha_{CC}=\alpha_{DD}$=25 are used in our simulations.

3.2.6 Sample preparation for characterizations

The characterization of supracolloids is referred to section 2.6 in Chapter 2.

UV-vis Absorption Spectroscopy. Absorbance measurements of samples was conducted in a PERKIN LAMBDA 35 UV/vis system. For absorbance of hierarchical assembly structure, the sample (ensembles floating on aqueous phase after interfacial assembly) was transferred onto a transparent glass slide before measurement.

SEM and TEM imaging. The morphologies of assemblies were obtained using a Hitachi SU-70 Schottky FEG-SEM and a JEOL FEG-TEM. Hierarchical assembly samples for SEM and TEM analysis were prepared by lifting the film from the surface of aqueous phase to silicon wafer or copper grids, and gently rinsed with deionized water to remove the excess salt. All the above samples were dried at room temperature before imaging measurement.

3.3 Results and discussion

Co-assembly of **A** and **B** with different size, polymer length and feeding ratio in THF generates various amphiphilic supracolloids in high yields. Supracolloids designed in Chapter 2 (see Table 3.S1 for the parameters of supracolloids) were used for studying their further assembly at a higher hierarchy level in this Chapter. As mentioned early, since the surface chemistry was pre-encoded using incompatible polymer blocks, the supracolloids formed during level-1 assembly was endowed with an amphiphilic patchy surface, i.e., **AB** (hydrophilic/hydrophobic), **BAB** (hydrophobic/hydrophilic/hydrophobic) and **ABA** (hydrophilic/hydrophobic/hydrophilic). For easy characterization, the initial study was focused on two-dimensional assembly of supracolloids confined at the liquid/liquid interface. The assembly process was triggered by placing a dispersion of supracolloids in THF on top of saturated sodium chloride aqueous solution which is immiscible with THF and evaporating the volatile solvent of THF. The aqueous phase is a poor solvent for the PS blocks on particle **B**, but a good solvent for the PEO blocks on particle **A**. The change of solvent quality destabilized the hydrophobic polystyrene blocks of **B** within

supracolloids and induced the association of the hydrophobic domain to minimize the unfavorable interfacial energy between **B** and aqueous phase.

3.3.1 Assembly of amphiphilic supracolloidal dimers

The amphiphilic supracolloidal dimers were well dispersed in THF. In this case, the thick polymer shell provides steric stabilization to prevent the aggregation of supracolloids in the solution. During the second step assembly, the dimers were forced to contact with water at the liquid/liquid interface, which drove the association of **B** particles. Meanwhile, during the THF evaporation, the concentration of dimers close to the interface was increased, which also facilitated the aggregation of dimers in defined interface domain. In the end, **B** NPs tended to aggregate while leaving the **A** NP in the outlayer, which results in the formation of petal-like structure, as shown in Figure 3.2.

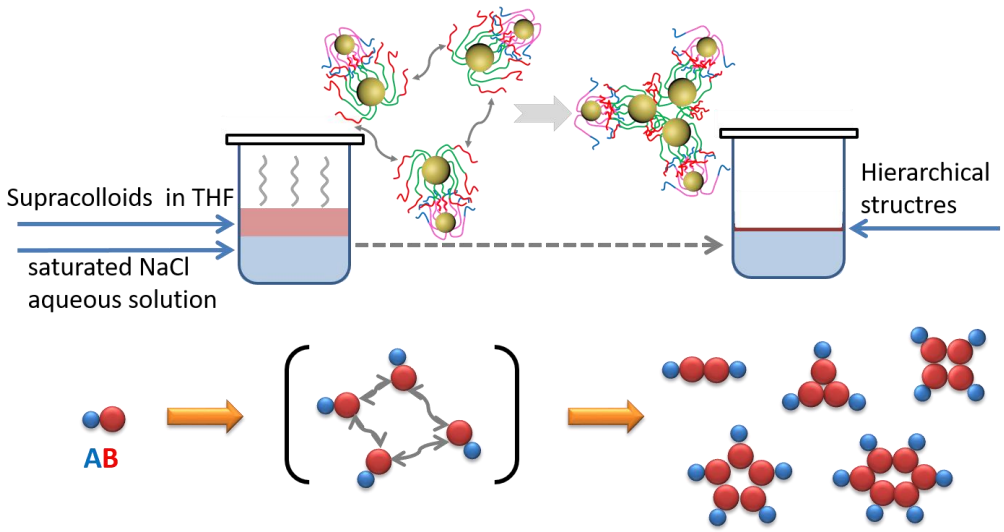

Figure 3.2 Scheme of liquid-liquid interfacial assembly and the association of dimer into petal-like structures.

$A_{20}B_{24}$ supracolloidal dimers were used as the building blocks for the interfacial assembly. They were obtained by co-assembly of **A_{20}**: 20 nm Au NP tethered with polymer P3 and **B_{24}**: 24 nm Au NP tethered with polymer N4 (see Figure 2.5 for the characterization of **$A_{20}B_{24}$**). To further facilitate the formation of petal-like structure, acid was added into salt aqueous solution. Upon the addition of acid, the residual charge from carboxyl group on **B** particles was reduced due to protonation with additional H^+, thus weakening the repulsion among **B** particles and facilitating the formation of petal structure. After slow evaporation of THF, the hierarchical assemblies was formed on the surface of the aqueous solution. Figure 3.3(a-j) shows a panel of representative SEM and TEM images of petal-like structure **$(AB)_N$** assembled from **$A_{20}B_{24}$** amphiphilic dimer. In the petal-like structure, the hydrophobic units, **B**, converge forming an inner ring, while the hydrophilic particles **A** form an outer layer. Large area TEM image of the petal-like structure can be found in Figure 3.S1. Figure 3.3k shows the angle distribution between dimers within petals. The angles were found to be158.4±16.8°, 118.7±12.6°, 89.6±9.3°, 70.7±10.4°, and 58.8±10.3° for **$(AB)_2$**, **$(AB)_3$**, **$(AB)_4$**, **$(AB)_5$**, and **$(AB)_6$**, respectively. The highly symmetric arrangement of dimer units within each type of petals suggests the presence of long-range repulsive interactions between dimers to force them separate equally in space. We presume that the high symmetry can be attributed to the steric repulsion of polymer brushes on **A** and the residual charge of **A** from the protonation of residual amine group in acidic environment. This is also supported by the fact that the measured angle deviated more from traditional polygon geometries as the number

of petals decreased, due to reduced repulsion for particles **A** with a larger interparticle spacing.

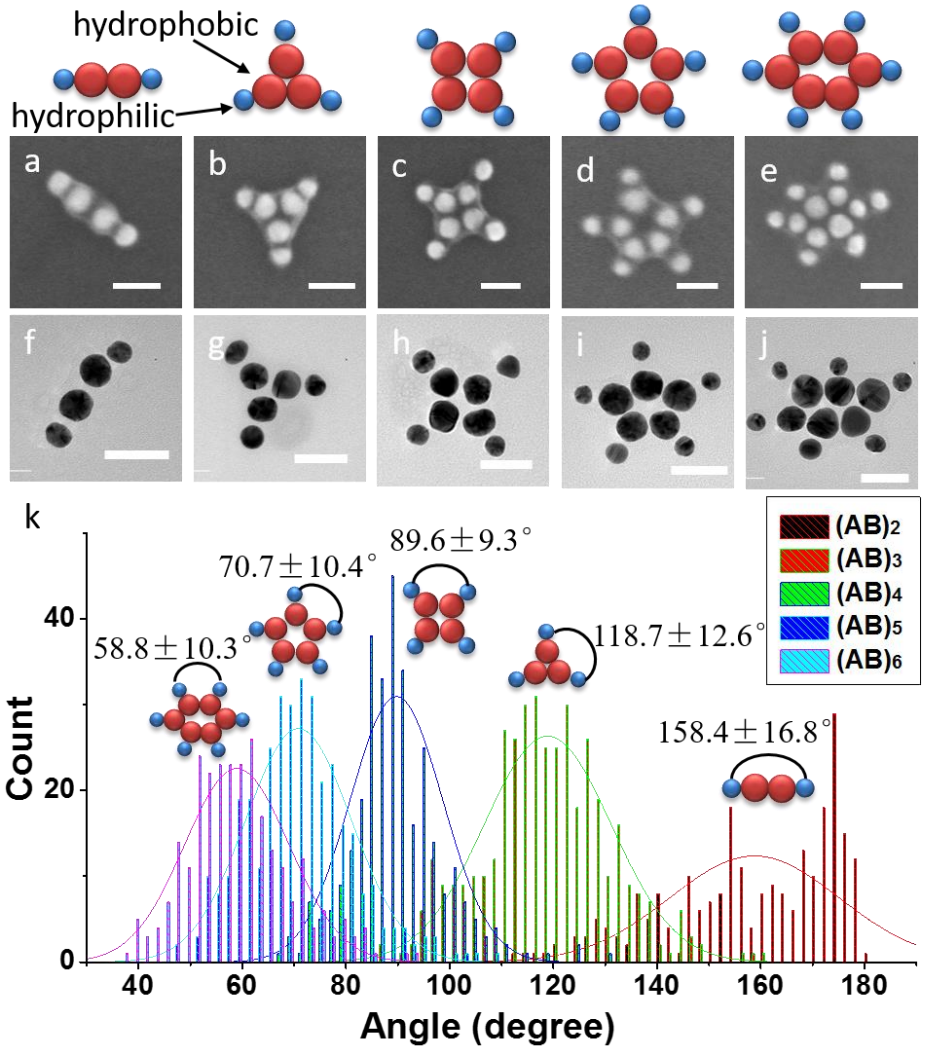

Figure 3.3 Petal-like structure formed from amphiphilic dimer **AB**. (a-j) SEM (a-e) and TEM (f-j) images of petal-like structure formed from $\mathbf{A_{20}B_{24}}$ with aggregation number of dimers from 2 to 6. Scale bar: 50 nm. (k) Angle distributions of petal-like structures.

3.3.2 Mechanism of forming petal-like structure

To understand the formation mechanism of petal-like structure, control experiments were conducted with hydrophilic **AB** (both **A** and **B** are hydrophilic) and hydrophobic **AB** dimers (both **A** and **B** are hydrophobic). The interfacial assembly of them both led to the formation of alternating chains (Figure 3.4). However, some hydrophilic **AB** dimers still remained as individual, while hydrophobic **AB** dimers tended to form tangled and branched long chains. As shown in Figure 3.4e, when **AB** dimers was placed on top of aqueous phase, the introduction of water favored the ionization of the Lewis base/acid containing block, strengthening the electrostatic attraction between the oppositely charged blocks on **A** and **B**, thus, the dimers could prefer an head-to-end connection to form alternating chains driven by electrostatic attraction between **A** and **B** (blue arrow). Meanwhile, introducing water also trigger the hydrophobic force, which favor the aggregation of hydrophobic domain (red arrow). Therefore, for hydrophilic **AB** (no hydrophobic domain), the electrostatic force is predominant, resulting head-to-tail connection of **AB** to form chains. For amphiphilic **AB**, both electrostatic force and hydrophobic force existed, the predominant hydrophobic force led to the aggregation of **B** particle to form petal-like structure. While for hydrophobic **AB**, the hydrophobic attraction applied for both **A** and **B** (favoring **AB**, **AA** and **BB** aggregation), together with the electrostatic force favoring **AB** connection. Therefore, the collective effect of hydrophobic attraction and electrostatic attraction gave rise to the formation of tangled chains.

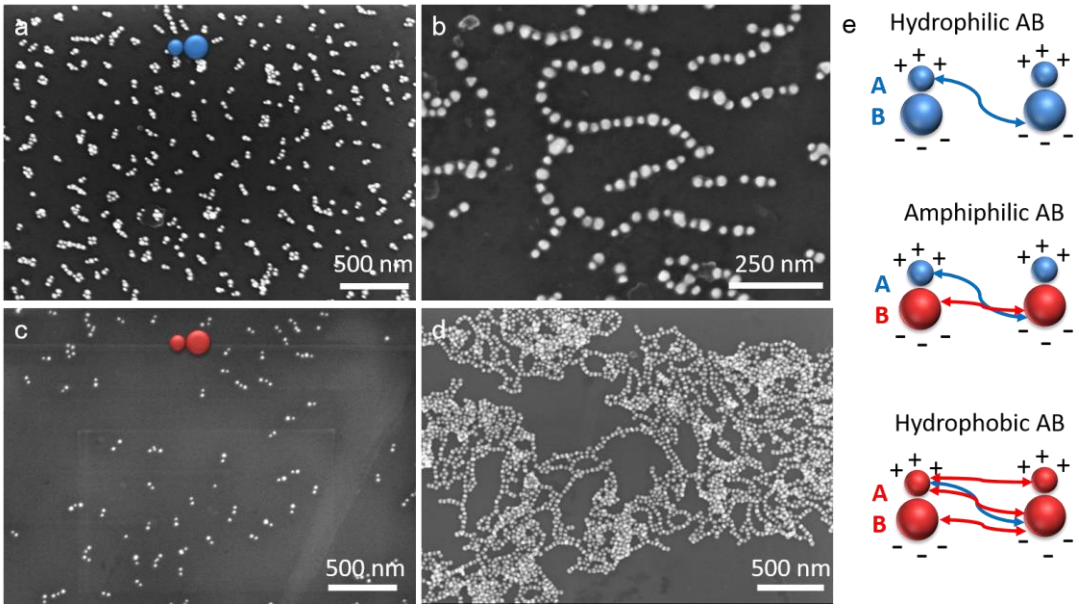

Figure 3.4 Interfacial assembly of hydrophilic and hydrophobic **AB**. (a) SEM image of hydrophilic $\mathbf{A_{20}B_{24}}$, the BCPs used for surface modification are polymer P3 and PEO_{45}-*b*-$P(AA_{0.3}$-*r*-$St_{0.7})_{328}$-SH. (b) SEM image of chains formed from further assembly of hydrophilic $\mathbf{A_{20}B_{24}}$. (c) SEM image of hydrophobic $\mathbf{A_{20}B_{24}}$, the BCPs used for surface modification are PS_{173}-*b*-$P(DMAEMA_{0.3}$-*r*-$St_{0.7})_{300}$-SH and polymer N4. (d) SEM image of tangled chains formed from further assembly of hydrophobic $\mathbf{A_{20}B_{24}}$. Scale bar: 500 nm. (e) Scheme of interactions between dimers **AB** during interfacial assembly.

When initial building block **A** and **B** were directly subjected to interfacial assembly without the formation of dimers, this process led to the formation of irregular aggregates of the NPs (Figure 3.5). In this case, the individual **B** particles would aggregate at the interface, while the **A** particles would just disperse around the aggregated **B** particles, thus leading to the aggregation of particles without obvious

order or pattern. These results further confirm that the multiple steps of assembly and the amphiphilicity of **AB** dimers are crucial to the formation of petal-like structures.

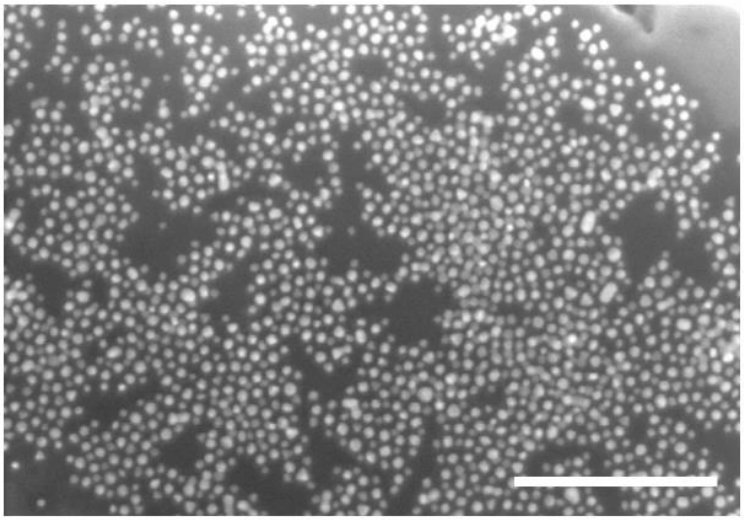

Figure 3.5 SEM image of film formed after liquid-liquid interfacial assembly from $\mathbf{A_{20}}$ and $\mathbf{B_{24}}$ without first step assembly. Scale bar: 500nm.

3.3.3 Effect of acid on the formation of petals

The protonation of trace amount of tertiary amine groups in the presence of acid generates weak charges on **A** particle, resulting in the symmetric geometry of the petal-like structures with minimal repulsive interaction energy between **A** particles. For better understanding of the assembly process, we studied the effect of acid on the assembly of dimers into petals. First, zeta potential of hybrid building block $\mathbf{A_{20}}$ and $\mathbf{B_{24}}$ with the addition of acid was measured, as shown in Figure 3.6. In order to avoid the effect of introducing water, acetic acid was used as the source of acid. With the gradual addition of acid, the zeta potential for both $\mathbf{A_{20}}$ and $\mathbf{B_{24}}$ gradually shifted from a more negative value towards positive potential, which suggests the protonation of tertiary amine groups of $\mathbf{A_{20}}$ and carboxyl groups of $\mathbf{B_{24}}$.

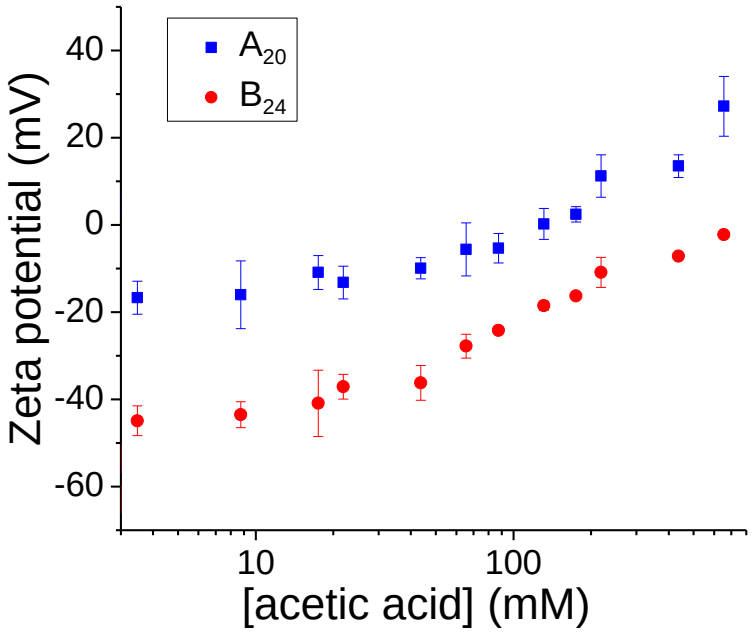

Figure 3.6 Zeta potential of $\mathbf{A_{20}}$ and $\mathbf{B_{24}}$ in respond to addition of acid.

Second, amphiphilic $\mathbf{A_{20}B_{24}}$ dimers were assembled in the presence of different amount of acids in the saturated salt solution. It was found that the average number of dimers (*N*) in petals $\mathbf{(AB)_N}$ increased with the addition of more acid (Figure 3.7). With no acid added, the majority of the assemblies is petal structures with two dimers (~60%). The value of *N* gradually increased from 3.1, to 3.6, and finally to 4.1, when the concentration of acid in aqueous phase increased from 0.1 M to, 0.2, 0.4 M, respectively (Figure 3.7f). This can be explained by more acidic environment facilitate the protonation of –COOH group on **B** particles, which increased the hydrophobicity of **B** due to weaker electric double layer.

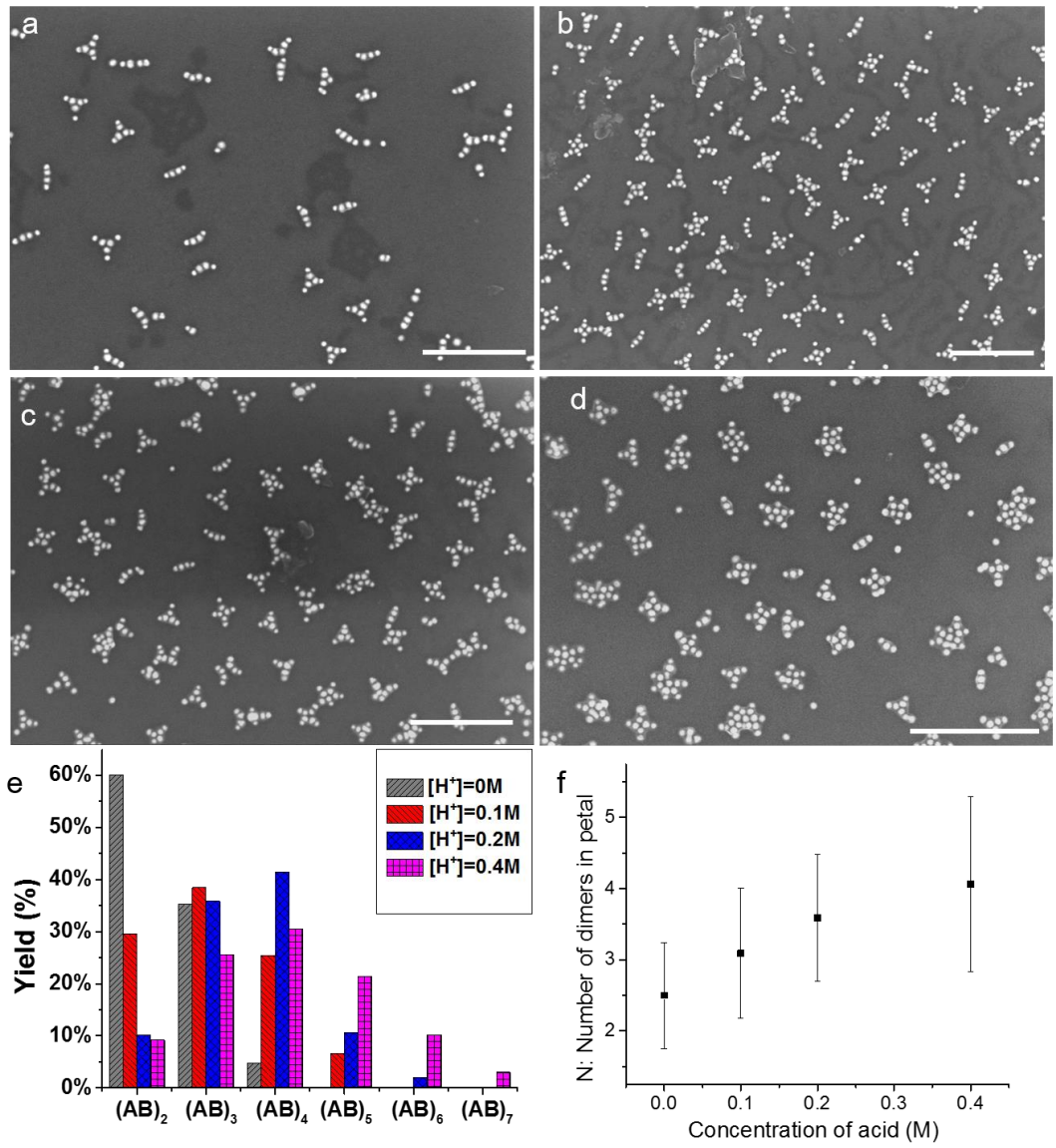

Figure 3.7 Tune the aggregation number of dimers in petal structure by adding acid. (a-d) SEM images of $\mathbf{(AB)_N}$ formed by $\mathbf{A_{20}B_{24}}$ with $[H^+]$=0M, 0.1M, 0.2M, 0.4M respectively. Scale bar: 500 nm. (e) Yield distribution of $\mathbf{(AB)_N}$ formed by $\mathbf{A_{20}B_{24}}$ under different $[H^+]$. (f) Average aggregation number of dimers (*N*) in petal structures $\mathbf{(AB)_N}$ under different $[H^+]$.

3.3.4 Effect of size ratio on the formation of petals

The number of petals can also be adjusted by changing the size ratio of the hydrophobic core of **B**/hydrophilic core of **A** and hence the strength of hydrophobic attraction among **AB**. Figure 3.8 shows the petal-like structures assembled from **AB** with different size ratios of **B/A.** The average aggregation number of dimers in petals increased with the increase in size ratio of **B/A** (Figure 3.8a-c). We define D(x/y) as the size ratio of **B** particle with diameter of x nm and **A** particle with diameter of y nm. The majority of assemblies were $\mathbf{(AB)_2}$ with yields above 70% for D(18/25) (Figure 3.9a). With increase size ratio to D(24/20), a greater population of $\mathbf{(AB)_3}$ and $\mathbf{(AB)_4}$ was achieved, while the population of $\mathbf{(AB)_2}$ was found to greatly decrease. Further increasing the size ratio to D(30/20) led to higher ratio of $\mathbf{(AB)_5}$ and $\mathbf{(AB)_6}$. (Large area SEM images can be found in Figure 3.S2.) This is due to the increased hydrophobicity to hydrophilicity balance of **AB** dimers with increasing size ratio of **B/A**, which gradually strengthened the hydrophobic forces between dimers. A gradual red-shift of UV-vis spectrum from 549 to 575 to 583 nm was observed when the size ratio increased from D(18/25), to (D24/20), and to D(30/20), respectively (Figure 3.9e). This can be explained by increasing aggregation number of dimers and smaller interparticle distance with increasing size ratio, suggesting the well agreement between structure and optical property of petal-like structures.

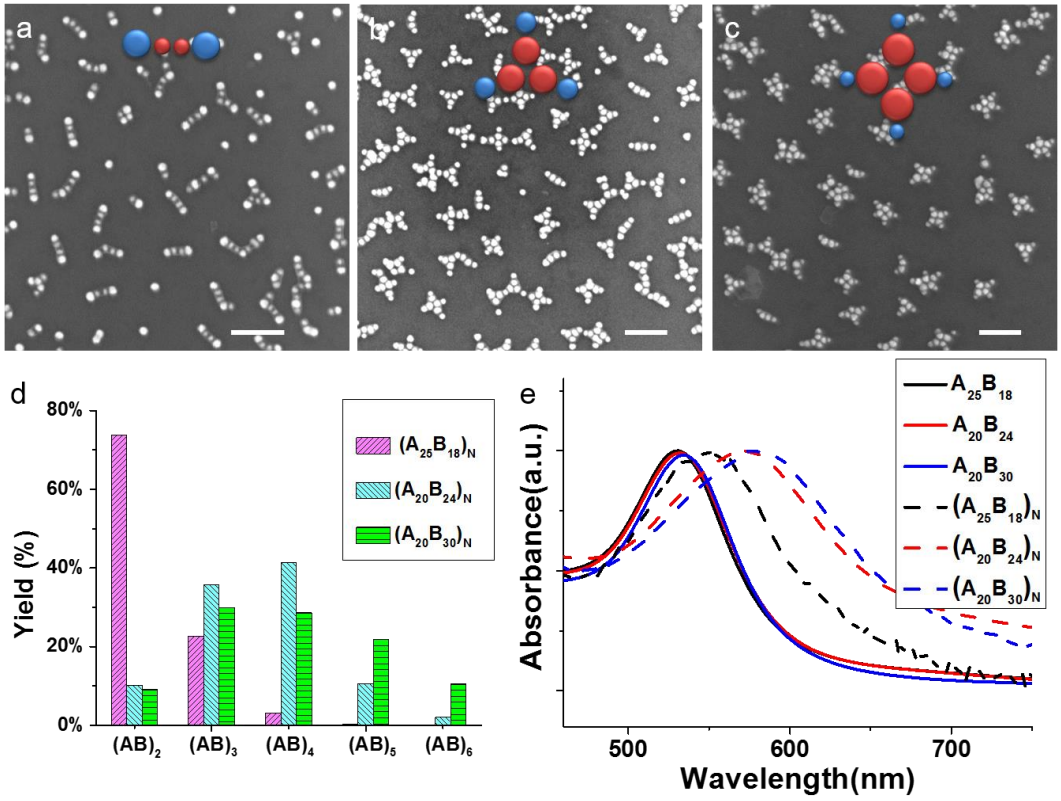

Figure 3.8 Tune the aggregation number of dimers in petal structure by changing the size ratio of **B**/**A**. (a-c) SEM images of $\mathbf{(AB)_N}$ formed by $\mathbf{A_{25}B_{18}}$ (a), $\mathbf{A_{20}B_{24}}$ (b), and $\mathbf{A_{20}B_{30}}$ (c). Scale bar: 200 nm. (d) Aggregation number distribution of $\mathbf{(AB)_N}$ in Figure 4 (a-c). (e) UV-vis absorption spectrum of **AB** and corresponding $\mathbf{(AB)_N}$ with different size ratio of **B**/**A**.

It is worth noting that larger irregular aggregates rather than well-defined petal structures were obtained when $\mathbf{A_{20}B_{36}}$ was used (Figure 3.9). This can be attributed to the combination effect of increase in the hydrophobic contact area between **B** particles and decrease in the repulsive interaction between **A** particles. As shown in Table 3.1, the number of grafted BCPs on NPs increased with the increase of NP sizes, although a trend of decrease in the grafting density σ of BCPs was observed. See Figure 3.S3 for the TGA curve for **A** and **B** particles with different sizes. This

suggests a larger volume of hydrophobic segments on **B** particles and hence a higher hydrophobic interactions for dimers with larger hydrophobic core. Moreover, the larger separation distance between **A** particles (caused by the presence of larger **B** particles in the center of petals) weakened the repulsion between **A** (assuming that the same amount of residual charges is presented on **A**), thus weakening control over the valence.

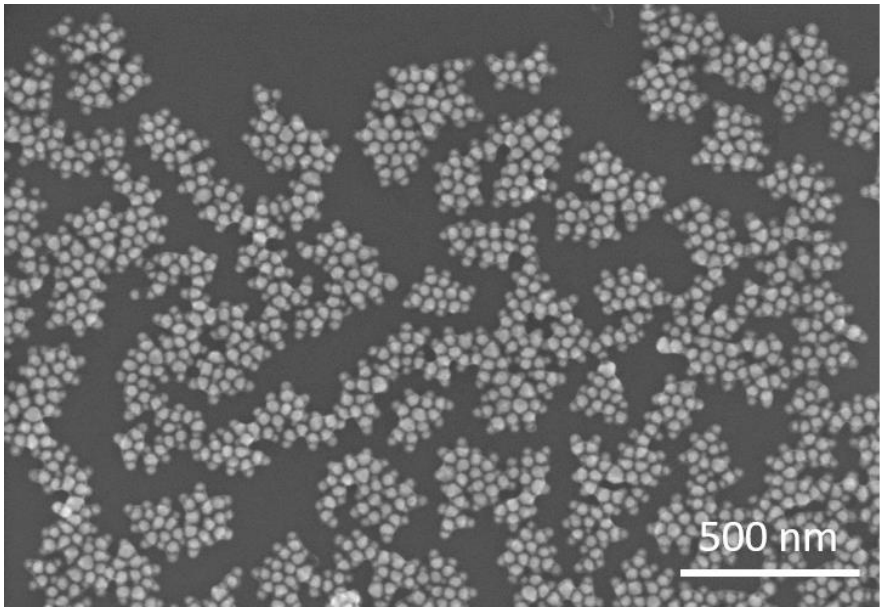

Figure 3.9 SEM image of assembled structure formed from $\mathbf{A_{20}B_{36}}$.

Table 3.1 Grafting density σ and average number of BCP ligands per Au NP for hybrid building blocks **A** and **B** with different size.

Hybrid building blocks	$\mathbf{A_{20}}$	$\mathbf{B_{18}}$	$\mathbf{B_{24}}$	$\mathbf{B_{30}}$	$\mathbf{B_{36}}$
Grafting density σ (chain/nm^2)	0.0833	0.0833	0.0812	0.0690	0.0562
Number of BCP ligands per NP	105	85	147	195	229

Interestingly, the interparticle distance between **B-B** (d_{BB}) and **A-B** (d_{AB}) appears to be largely dependent on the size of **A** and **B** NPs. Figure 3.10a shows a representative scheme and calculation of d_{BB} and d_{AB} for three-petal structure. Figure 3.10b indicates a summary of interparticle distance for $\mathbf{(AB)_N}$ with different size of **A**

and **B**, as well as aggregation number *N* (The actual number of interparticle distance is shown in Table 3.S2). Taking **$(AB)_2$** as an example, With the increasing of the size of **B** NPs from 18 nm to 36 nm, d_{BB} decreases gradually from 9.94±2.42 nm to 7.44±1.45 nm due to the thinner polymer shell from low grafting density .

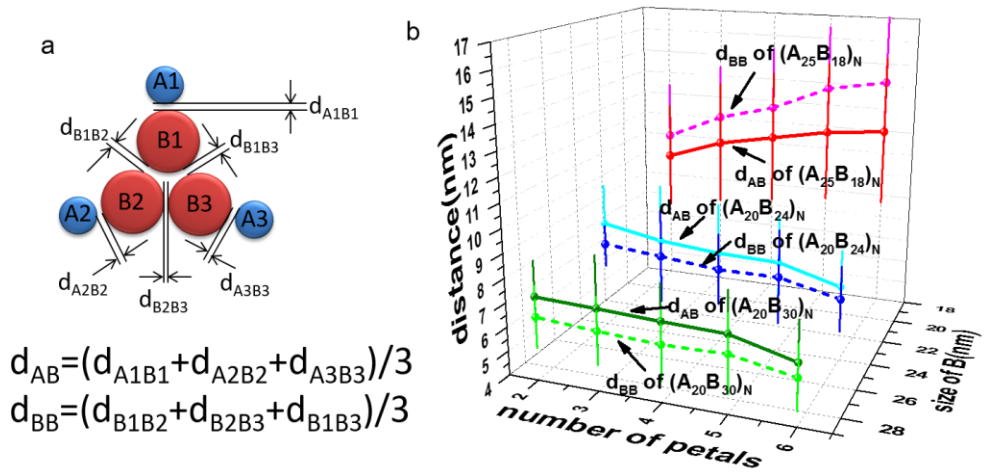

Figure 3.10 (a) Scheme of interparticle distance of **$(AB)_3$** and the calculation of d_{AB} and d_{BB}. (b) Interparticle distance d_{AB} and d_{BB} in petal structures.

3.3.4 Assembly of BAB hydrophobic/hydrophilic/hydrophobic trimers into chains

In addition to the formation of petal-like structures from **AB** dimers, the use of trimers (e.g., hydrophobic/ hydrophilic/ hydrophobic **BAB** and hydrophilic/hydrophobic/ hydrophilic **ABA**) enables the generation of more diverse hierarchical assemblies. When **BAB** trimers in which one hydrophilic **A** is sandwiched between two hydrophobic **B** NPs to form linear CO_2-like structures, were used, the end-to-end association of hydrophobic **B** in the presence of water led to the production of linear chains with alternative arrangement of two **B** and one **A** at the

interface (Figure 3.11). The same linear assembly of alternating chains was not observed for trimers with the same sized NPs but solely hydrophilic outer block of BCPs, and the assembly of hydrophobic **BAB** led to disordered aggregation of trimers. The result confirmed that the amphiphilic surface anisotropy is essential for the chaining of **BAB**. (Figure 3.S4)

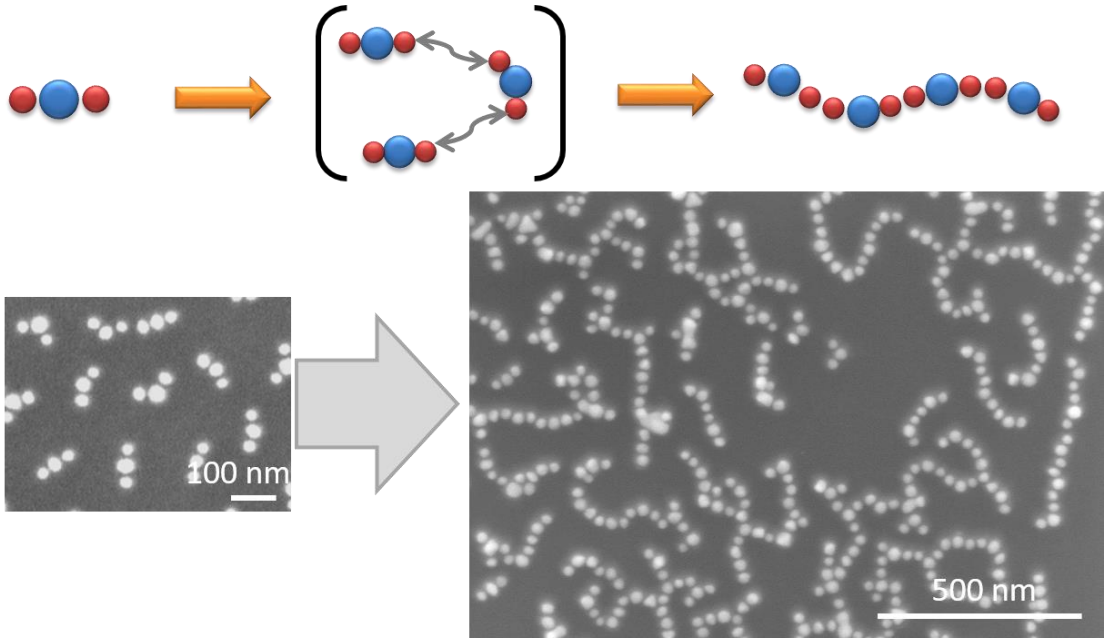

Figure 3.11 Scheme of end-to-end association of **BAB** into chain structure.

Figure 3.12 (a-c) shows different chains assembled from **BAB** trimers with different size of **A** and **B** NPs (See large area SEM images in Figure 3.S5). Interestingly, increasing the size ratio of **B/A** of the trimers from $\mathbf{B_{24}A_{36}B_{24}}$ to $\mathbf{B_{24}A_{20}B_{24}}$ doesn't change the sequential chain structure, only affect the interparticle distance (Figure 3.S5, Table 3.2). However, Further increasing the size ratio to $\mathbf{B_{30}A_{20}B_{30}}$, the chains of trimers begin to connect, forming a network structure, where the branch points are composed of three or more **BAB** trimers. We define the average

chain length as the number of **BAB** between two nearest branching points (See scheme in Figure 3.S7). Figure 3.12d shows the length distribution of chains assembled from trimers with different size ratios of **B/A** from 24/36, to 24/20 to 30/20. An increase in the average interparticle distance between **B** particles with the increase in the size ratio was observed (Table 3.2). Upon the chain formation, an obvious red-shift in UV-vis spectrum was observed for all chains (Figure 3.13e). It is interesting that the red-shift of chains continuously increased with decreasing interparticle distance, indicating a stronger dependence of plasmonic coupling on the interparticle distance rather than the length of chains.

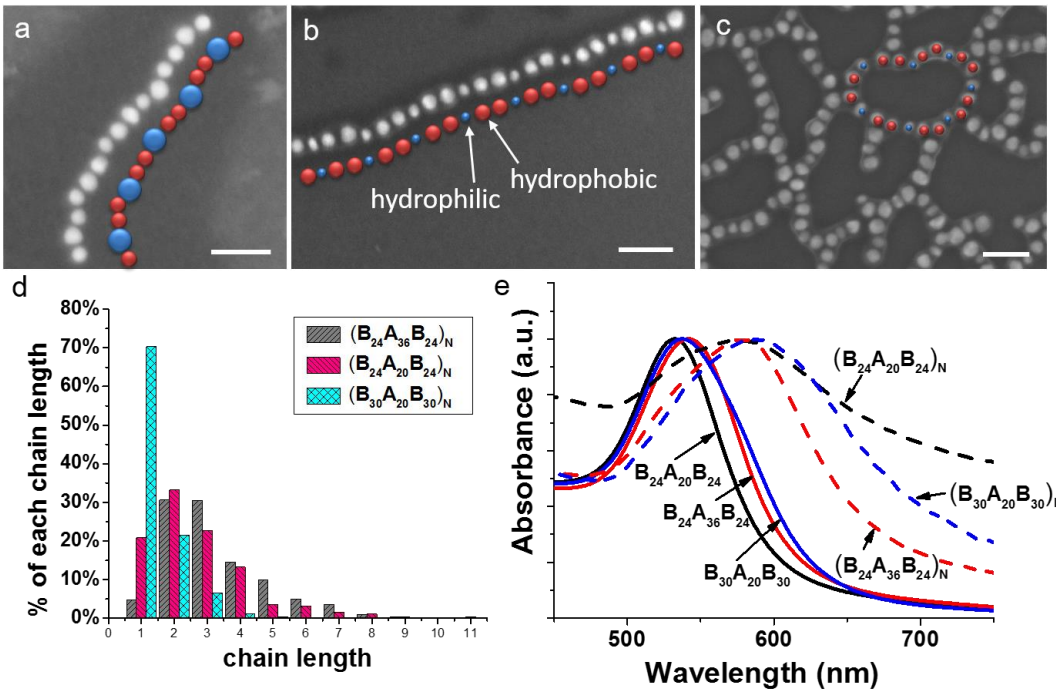

Figure 3.12 End to end connection of **BAB** with tunable size ratio of **B/A**. (a-c) SEM images of $\mathbf{(BAB)_N}$ formed by $\mathbf{B_{24}A_{36}B_{24}}$ (a), $\mathbf{B_{24}A_{20}B_{24}}$ (b) and $\mathbf{B_{30}A_{20}B_{30}}$ (c) respectively. Scale bar: 100 nm. (d) Chain length distribution for the chains of **BAB**. (e) UV-vis absorption spectrum of **BAB** and corresponding $\mathbf{(BAB)_N}$ with different size ratio of **B/A**.

Table 3.2 Interparticle distance of $\mathbf{(BAB)_N}$ with different size of Au NPs.

Sample	d_{AB}	d_{BB}
$\mathbf{(B_{24}A_{36}B_{24})_N}$	6.49±1.33 nm	8.17±1.46 nm
$\mathbf{(B_{24}A_{20}B_{24})_N}$	9.46±2.04 nm	8.9±1.5 nm
$\mathbf{(B_{30}A_{20}B_{30})_N}$	8.05±2.09 nm	7.42±1.84 nm

3.3.5 Assembly of ABA hydrophilic/hydrophobic/ hydrophilic trimers into ribbons

As discussed early, the surface chemistry of trimers can be tuned to produce amphiphilic **ABA** supracolloids in which one hydrophobic **B** is located between two hydrophilic **A** NPs. **ABA** trimers dispersed in THF were placed on top of a saturated NaCl aqueous solution, and an interface was formed due to the immiscibility of THF and the dense salt solution. The interface provides a platform for the assembly by specifically changing the solvent condition for trimers close to the interface, as the aqueous phase serves as a poor solvent for the PS rich **B** particles. The association of **B** particle led to the side-by-side assembly of trimers to reduce the unfavorable interface between PS and the aqueous phase. After the slow evaporation of THF, the ensembles was obtained on the surface of the aqueous phase, where trimers stack into ribbon structures, protecting the hydrophobic center in the inner back bone and leaving the hydrophilic ends as the outer wings, analogous to peptide ribbons. (Figure 3.13).

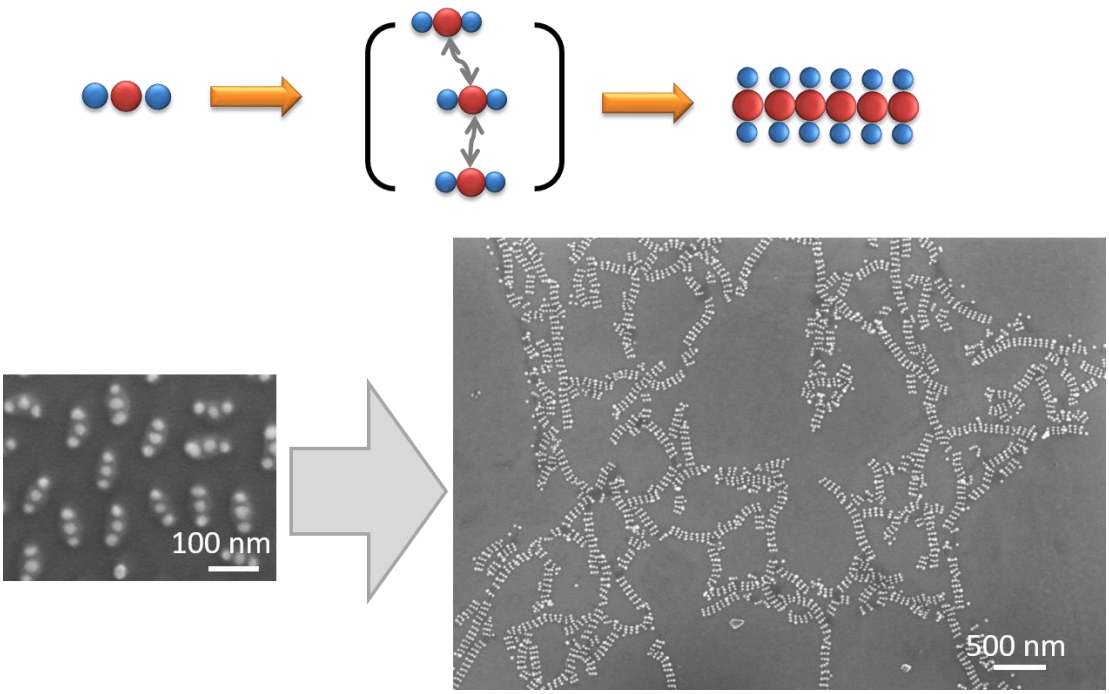

Figure 3.13 Scheme of side-by-side stacking of **ABA** into ribbon structure.

We studied the effect of relative size ratio of **B/A** on the assembly of ribbons at the interface. As shown in Figure 3.14 (a-c), with the decrease in D(x/y) from D(36/20) to D(30/20) to D(24/20) ($\mathbf{A_{20}B_{36}A_{20}}$ → $\mathbf{A_{20}B_{30}A_{20}}$ → $\mathbf{A_{20}B_{24}A_{20}}$), a gradually increase on the ribbon length and the interparticle distance was observed. (See Figure 3.S8 for large area SEM images.)The aggregation number *N* in the ribbon structures $\mathbf{(ABA)_N}$ increased from 3.6 to 3.7 to 7.3 based on the distribution of *N* in Figure 3.14d. The increase in ribbon length was accompanied with an increase in the rigidity (i.e., decrease in the flexibility) of ribbons and decrease in the defects along the ribbons. This can be attributed to the smaller size ratio of **B/A** strengthens the rigidity of **ABA**. Moreover, the residual charge on **B** NPs also play an important role, for larger **B** NPs, the stronger residual charge repels the attaching of approaching **ABA** which prevents the formation of longer ribbons. The interparticle distance

between **B** NPs in the ribbon was also investigated, which shows a larger distance with decreasing size ratio of **B/A**, as shown in Figure 3.14e. See Figure 3.S9 for the calculation of interparticle distance d_{BB}. The trend of interparticle distance observed in ribbon structure is in agreement with that observed in petal and chain structure, which is d_{BB} is in positive correlation with the grafting density of BCPs, suggesting that the consistent adjustment on the interparticle distance is feasible in our system. The UV-vis absorption spectrum is shown in Figure 3.14f, it appears that the ribbons formed from **ABA** with higher size ratio of **B/A** have a stronger red shift, which is due to the closer interparticle distance.

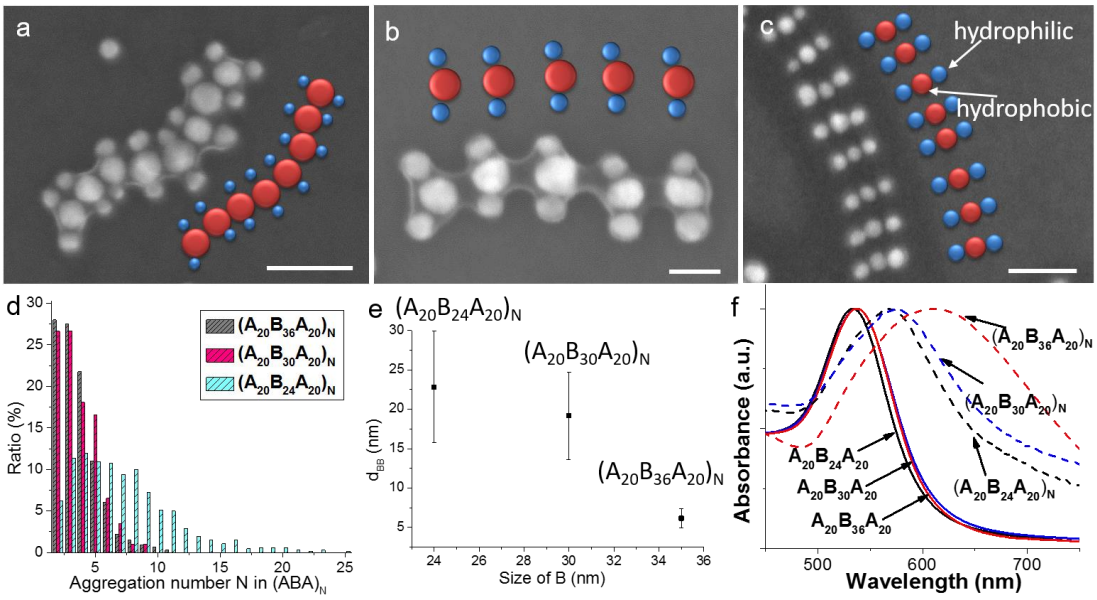

Figure 3.14 Side by side connection of **ABA** with tunable size ratios of **B/A**. (a-c) SEM images of $\mathbf{(ABA)_N}$ formed by $\mathbf{A_{20}B_{36}A_{20}}$, $\mathbf{A_{20}B_{30}A_{20}}$ and $\mathbf{A_{20}B_{24}A_{20}}$ respectively. Scale bar: 100 nm. (d) Aggregation number distribution of $\mathbf{(ABA)_N}$ with different size ratios of **B/A**. (e) Interparticle distance d_{BB} in ribbon structures with different size ratios of **B/A**. (f) UV-vis absorption spectrum of **ABA** and corresponding $\mathbf{(ABA)_N}$ with different size ratios of **B/A**.

3.3.6. DPD simulation of hierarchical assembly

We simulate the hierarchical assembly of amphiphilic supracolloids by DPD[108], using a CG model in our previous work[109]. In the simulation, the **A** and **B** building blocks were represented as blue and red particles. Our DPD simulation results are in good agreement with experimental observations: The petal-like structure (Figure 3.15 (a-b) is assembled from **AB**, ribbon structure is assembled (Figure 3.15c) from **ABA** and chain structure is assembled (Figure 3.15d) from **BAB**. Comparing the petal-like structure in Figure 3.15a and b, the transition in aggregation number N in $\mathbf{(AB)_N}$ comes from the different size ratio of **B**/**A**. As the size ratio decrease from Figure 3.15a to b, the average aggregation number also decrease accordingly, which is in well agreement with our experimental results. The different assembly geometry of trimers in Figure 3.15c and d results from the different surface amphiphilicity, hydrophilic/hydrophobic/hydrophilic trimers further assemble into ribbons, while switch the surface hydrophobicity led to the formation of chains, which is the same as the experimental results. Our simulations confirm that amphiphilic supracolloids can further assemble under hydrophobic driven, and the aggregation number can be tuned by the size ratio of NPs.

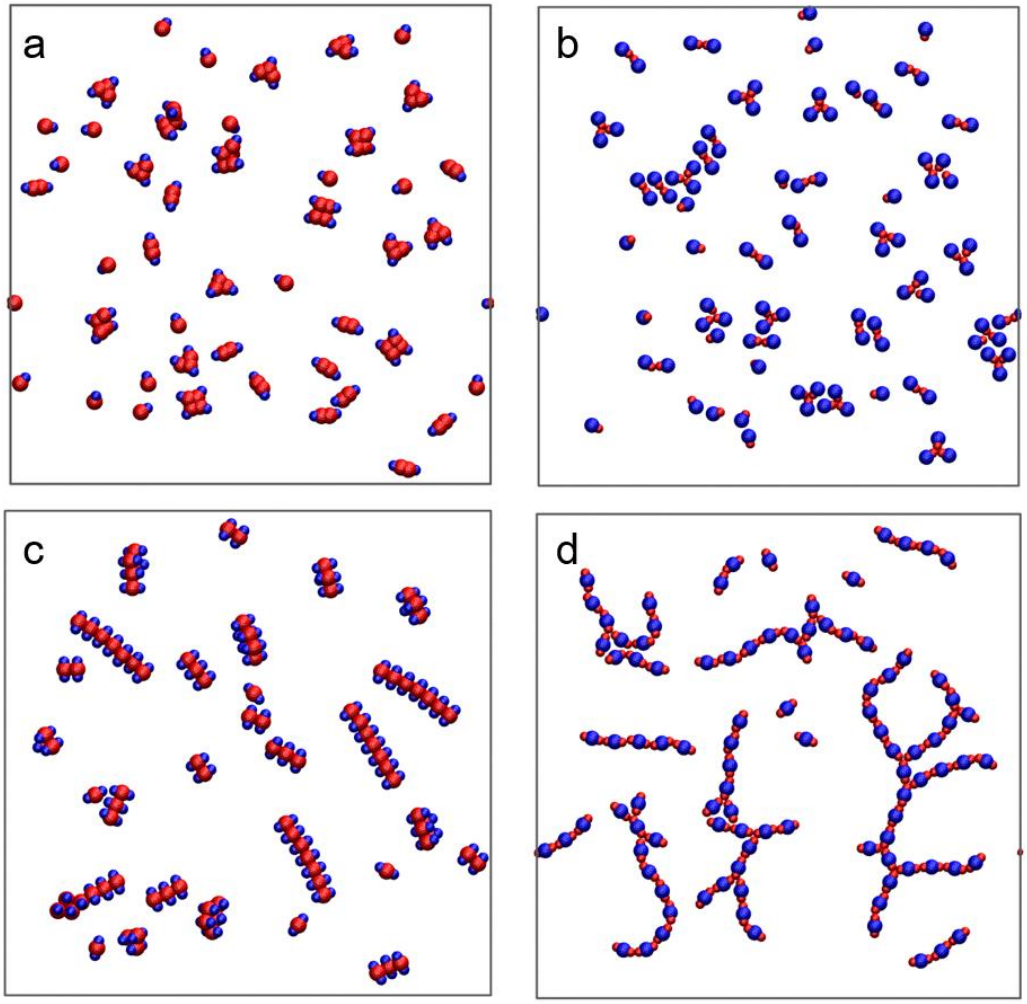

Figure 3.15 Simulation of forming petal like structure (a,b) from **AB** with different size of **A** and **B**, ribbon structure (c) from **ABA** and chain structure (d) from **BAB**.

3.4 Conclusion

In this Chapter, we demonstrated that amphiphilic supracolloids that are produced from binary assembly of inorganic NPs can further assemble into a variety of superstructures, including petal-like structures, ribbon structures, and chains at the liquid/liquid interface. It was found that the assembly is largely driven by the balance of hydrophobic attraction between **B** particles and electrostatic repulsion between

similarly charged NPs. The formation of different assembly structures is, therefore, determined by the relevant parameters such as the size ratio of **B/A**, the pH of aqueous phase and the amphiphilicity of supracolloids. It is particularly striking that the switching of hydrophobic/hydrophilic arrangement led to the change in the association mode of trimers from side-by-side to end-to-end, which suggest that anisotropic hydrophobicity serves an important role in the assembly process. This multi-step assembly strategy is simple yet versatile. It opens up avenues to construct new ensembles that are difficult to obtain via traditional assembly.

Chapter 4: The length effect of block copolymer tethers on the ribbon formation of supracolloidal trimers

Overview. The side-by-side association of amphiphilic **ABA** trimers with one hydrophobic center and two hydrophilic ends was demonstrated to be a feasible way to produce colloidal ribbon structures in the last chapter. The hydrophobic interaction originated from hydrophobic polystyrene blocks of BCPs on the central NPs was considered to be the driving force for the side-by-side association of trimers. Here, we report a systematic study on the effect of BCP length on the assembly of ribbon structures from amphiphilic supracolloidal trimers. A series of amphiphilic BCPs with different lengths of constituent blocks were used to functionalize NPs to construct **A** and **B** hybrid building blocks. The resulting supracolloidal trimers consist of hydrophilic and hydrophobic chemical patches of hairy polymers and hence local domains with tunable hydrophobicity. A product diagram of assembly was obtained to summarize the critical boundary conditions for the ribbon formation. The result provides not only guidance for the better fabrication of ribbons, but also new insights into the assembly mechanism of supracolloids at the interfaces.

A manuscript based on this chapter is in preparation and to be submitted to *Journal of the American Chemical Society*.

4.1 Introduction

Building blocks with anisotropic shape or chemistry are generally created to achieve directional and/or specific interactions for controllable assembly of functional materials. The unprecedented progress in the syntheses of inorganic NPs with controlled size, shape and composite in the past decades has drastically broadened the

library of building blocks that are available for assembly.[110] The concept of shape anisotropy has been proposed to assemble shaped NPs into complex structures. To achieve controllable assembly of spherical NPs with high precision, it is crucial to break the symmetry of NP surface. Various strategies have been developed to decorate the surface of as-synthesized NPs with defined chemical patches or controlled number and position of ligands, such as solid-state surface functionalization, phase separation of ligands, etc.[111] These methods, however, are either complicated, costly, or unscalable. Nevertheless, to date symmetry breaking of spherical particles still remains a challenge. Here we study the generation of **ABA** trimers (hydrophilic/hydrophobic/hydrophilic) by co-assembly of binary Au NPs tethered with functional BCPs and their further assembly into ribbon structures by tuning the amphiphilic patches. The lengths of binary BCPs tethers on **A** and **B** were tuned to study the effect of hydrophobic and hydrophilic brushes on the formation of ribbons. A transition from non-ribbon to ribbon formation was observed with increasing the length of hydrophobic polymer and decreasing the length of hydrophilic polymer. Inspired by these results, we confirmed the essential driven force of ribbon formation as central hydrophobic block and the critical boundary condition of BCP length for the ribbon formation. This systematical study provides new insights in understanding the controllable ribbon formation and the assembly mechanism of supracolloids at the interfaces.

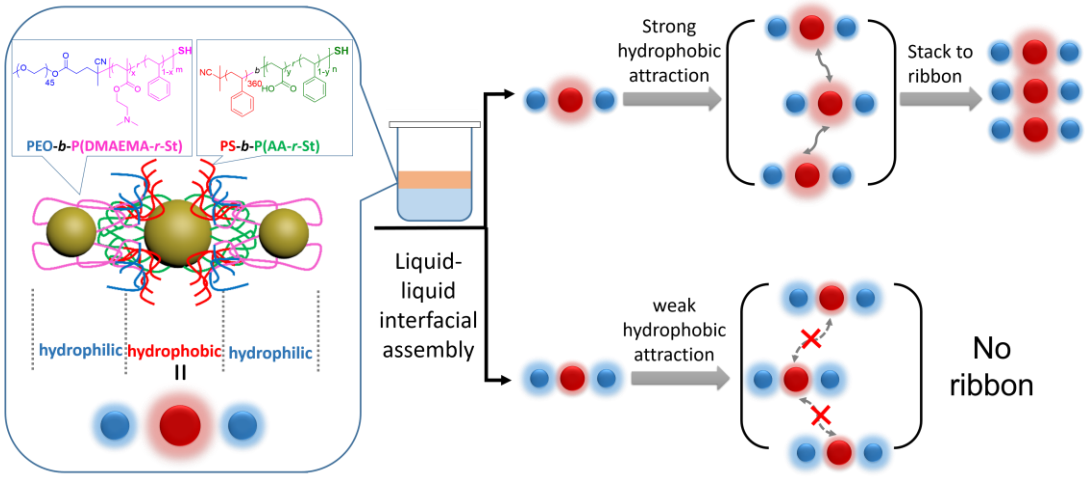

Figure 4.1 Scheme of self-assembly of amphiphilic trimers into ribbons. Increase the length of hydrophobic block of BCPs on **B** particle facilitate the ribbon formation, while increase the length of hydrophilic BCPs on **A** particle impede the ribbon formation.

4.2 Experiments

4.2.1 Materials

The BCPs, thiol-terminated PEO-*b*-P(DMAEMA-*r*-St)-SH and PS-*b*-P(AA-*r*-St)-SH, were synthesized separately using RAFT polymerization, Au NPs with diameter of 20 nm, 24 nm, 30 nm and 36 nm were synthesized by the same method described in experimental section in Chapter 2. Hydrochloric acid (36.5-38.0%), sodium chloride were purchased from Aldrich and used as received unless otherwise noted. Deionized water (Millipore Milli-Q grade) with resistivity of 18.0 MΩ was used in all the experiments.

See Figure 4.S1 and 4.S2 for representative ^{1}H NMR spectrum for PEO_{45}-*b*-$P(DMAEMA_{0.32}$-*r*-$St_{0.68})_{98}$-SH, and GPC curve for PS-CTA and PS-*b*-P(AA-*r*-St)-SH

with different lengths. By varying the amount of initiator and the monomer, and reaction time, PEO-*b*-P(DMAEMA-*r*-St)-SH and PS-*b*-P(AA-*r*-St)-SH with different lengths and charge ratios were synthesized, as listed in Table 4.1.

4.2.2 Building amphiphilic trimers ABA by co-assembly of A and B

The surface modification of Au NPs with BCPs is also referred to the experimental section in Chapter 2. Formation of **ABA** trimers was triggered by mixing binary building blocks **A** and **B** in THF. In detail, 1.2 mL of 20 nm **A** NPs (0.05 mg·mL^{-1}) were directly mixed with 1 mL of 24 nm **B** NPs (0.05 mg·mL^{-1}) in THF. The mixture was sonicated for 20 sec and then incubated for 2 hr. The sample was imaged by SEM and TEM to statistically analyze the yield of supracolloids.

4.2.3 Liquid-liquid interfacial assembly of trimers

Formation of ribbons was performed by liquid-liquid interfacial assembly of amphiphilic **ABA** trimers. Briefly, 1 mL of **ABA** trimers dispersed in THF was added to a mixture of 4 mL of a saturated sodium chloride solution and 1 mL aqueous solution of 1M HCl. Then the mixture was capped and incubated until all the THF was evaporated. Afterwards, the ensembles floated on the surface of the salt solution. The sample was imaged by SEM to analyze the structure of the ensembles.

4.2.4 Sample preparation for characterizations

BCPs were characterized by ^{1}H NMR and GPC, the grafting density of BCPs on Au NPs was characterized by TGA, amphiphilic **ABA** trimers and the ribbons structures were studied by zeta potential measurement, DLS, UV-vis Absorption spectroscopy, SEM and TEM, the sample preparation was described in Chapter 2-3.

4.3 Results and discussion.

4.3.1 Formation of amphiphilic ABA trimmers

The same approach described in Chapter 2 was used to fabricate amphiphilic supracolloidal **ABA** trimers. Hybrid building block **A** and **B** tethered with different lengths of BCPs is summarized in Table 4.1. 20 nm Au NPs tethered with PEO-*b*-P(DMAEMA-*r*-St)-SH with a molecular mass of x Kg/mol is denoted as **A(x)**, changing the length of BCPs resulting 3 types of **A** particle: **A(14)**, **A(22)**, and **A(55)**. It is worth noting that for the hydrophobic polymer, the major difference on polymer length comes from the pure polystyrene block instead of the random block, so we define **B(y)** to be Au NPs tethered with PS-*b*-P(AA-*r*-St)-SH with a polymerization degree of y for the first PS block. Four different length of hydrophobic polymers were used to modify the surface of 24 nm Au NPs, resulting 4 types of **B** particle: **B(90)**, **B(111)**, **B(140)** and **B(267)**. The grafting density, σ, for **A(22)** and **B(267)** was calculated to be 0.215 chain/nm^2 and 0.0812 chain/nm^2 based on the TGA curve in Figure 4.S3. The distinct grafting density of **A** and **B** particles comes from the different polymer lengths and core NP sizes. Based on the self-limiting nature of the ligand-exchange process, the already attached polymer chains impose a steric barrier for the incoming polymer chains, and the steric force would be stronger for longer polymer chains. Also, as for larger Au NPs, the local environment for each polymer brush would be more crowded due to the decreased curvature of particles.

Table 4.1 Summary of A and B particles with different length of BCPs tethers.

Hybrid building blocks	Diameter of Au NP (nm)	BCPs	$M_{n,\ NMR/GPC}$ [c] (Kg·mol^{-1})
A(14)	20	PEO_{45}-*b*-$P(DMAEMA_{0.32}$-*r*-$St_{0.68})_{98}$	**13.9**
A(22)		PEO_{45}-*b*-$P(DMAEMA_{0.41}$-*r*-$St_{0.59})_{156}$	**21.6**
A(55)		PEO_{45}-*b*-$P(DMAEMA_{0.40}$-*r*-$St_{0.60})_{419}$	**54.5**
B(90)	24	$PS_{\mathbf{90}}$-*b*-$P(AA_{0.31}$-*r*-$St_{0.69})_{273}$	35.1
B(111)		$PS_{\mathbf{111}}$-*b*-$P(AA_{0.31}$-*r*-$St_{0.69})_{289}$	38.8
B(140)		$PS_{\mathbf{140}}$-*b*-$P(AA_{0.31}$-*r*-$St_{0.69})_{279}$	40.9
B(267)		$PS_{\mathbf{267}}$-*b*-$P(AA_{0.32}$-*r*-$St_{0.68})_{318}$	57.7

Figure 4.2 exhibits the characterization of **ABA** form by co-assembly of **A(22)** and **B(267)**. The large area SEM image (Figure 4.2a) indicates a majority of supracolloids to be **ABA** trimers, and statistics based on more SEM images show a yield of 75.4%. The hydrodynamic diameter measured by DLS (Figure 4.2c) further supports the formation of trimers in THF, as an obvious shift in the hydrodynamic diameter was observed for **A** and **B** particles before and after self-assembly. The zeta potential of **A** and **B** particles and the trimers were also measured, which suggests the neutralization of the Lewis acid and base during the self-assembly (see Figure 4.S4). However, the shift in the UV-Vis absorption is not obvious, mainly due to the thick polymer shell blocking the coupling of NPs, as shown in Figure 4.2d.

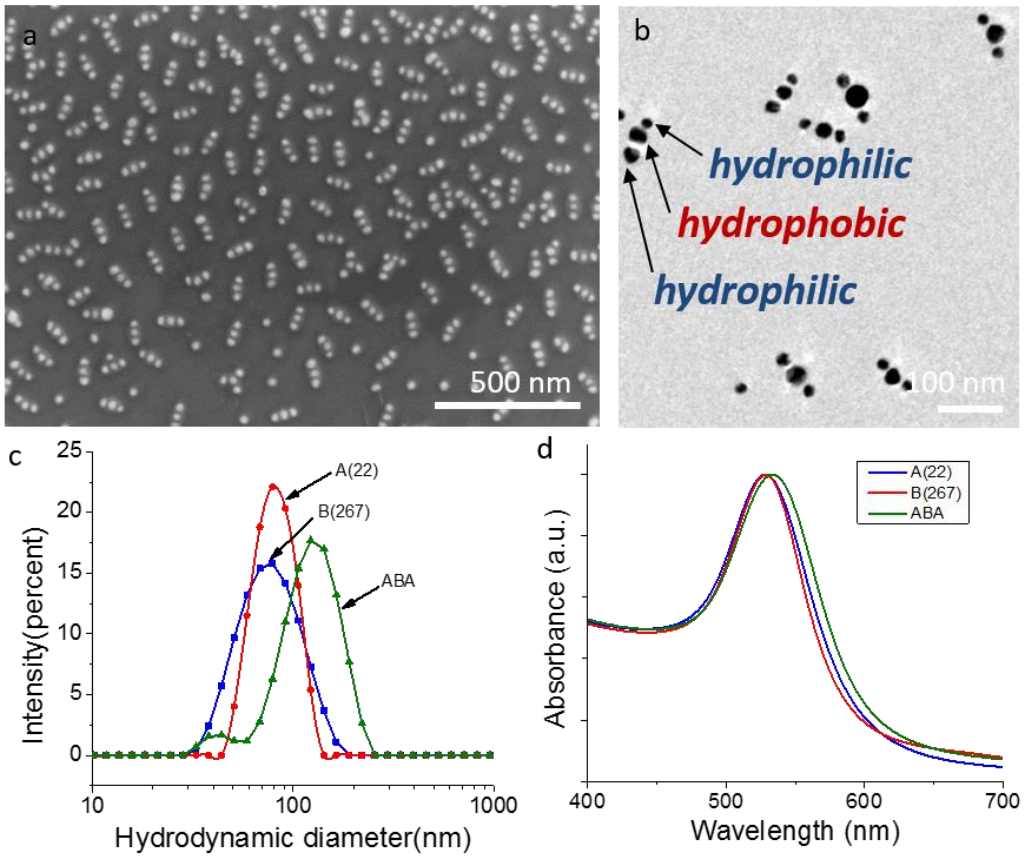

Figure 4.2 Characterization of amphiphilic trimers **ABA** formed by **A(22)** and **B(267)**. (a-b) SEM (a) and TEM (b) images of trimers **ABA**. (c-d) Hydrodynamic diameters (c) and UV-vis spectrum (d) of hybrid building block **A**, **B** and amphiphilic trimers **ABA**.

4.3.2 Fabrication of amphiphilic supracolloidal trimers using BCPs with different lengths of constituent blocks.

To investigate the effect of polymer lengths on the further assembly of supracolloids, we fabricated amphiphilic **ABA** supracolloids using the combination of different **A** and **B** summarized in Table 4.1. Consequently, amphiphilic supracolloidal trimers with various flexible hydrophilic/hydrophobic thickness were produced and

used for the subsequent assembly studies in following section (Figure 4.3). A horizontal view from left to right exhibit trimers with increasing length of hydrophobic brushes on **B**, and a vertical view from top to bottom represents trimers with increasing hydrophilic brush length. For instance, sample a-3 represent **ABA** trimers assembled from **A(14)** and **B(140)** (i.e., **A**: 20 nm Au NP tethered with PEO_{45}-*b*-$P(DMAEMA_{0.32}$-*r*-$St_{0.68})_{98}$ and **B**: 24 nm Au NP tethered with PS_{140}-*b*-$P(AA_{0.31}$-*r*-$St_{0.69})_{279}$). Figure 4.3a-c shows that the yield of **ABA** supracolloidal trimers was ~60% - 75%, depending on the types of BCPs.

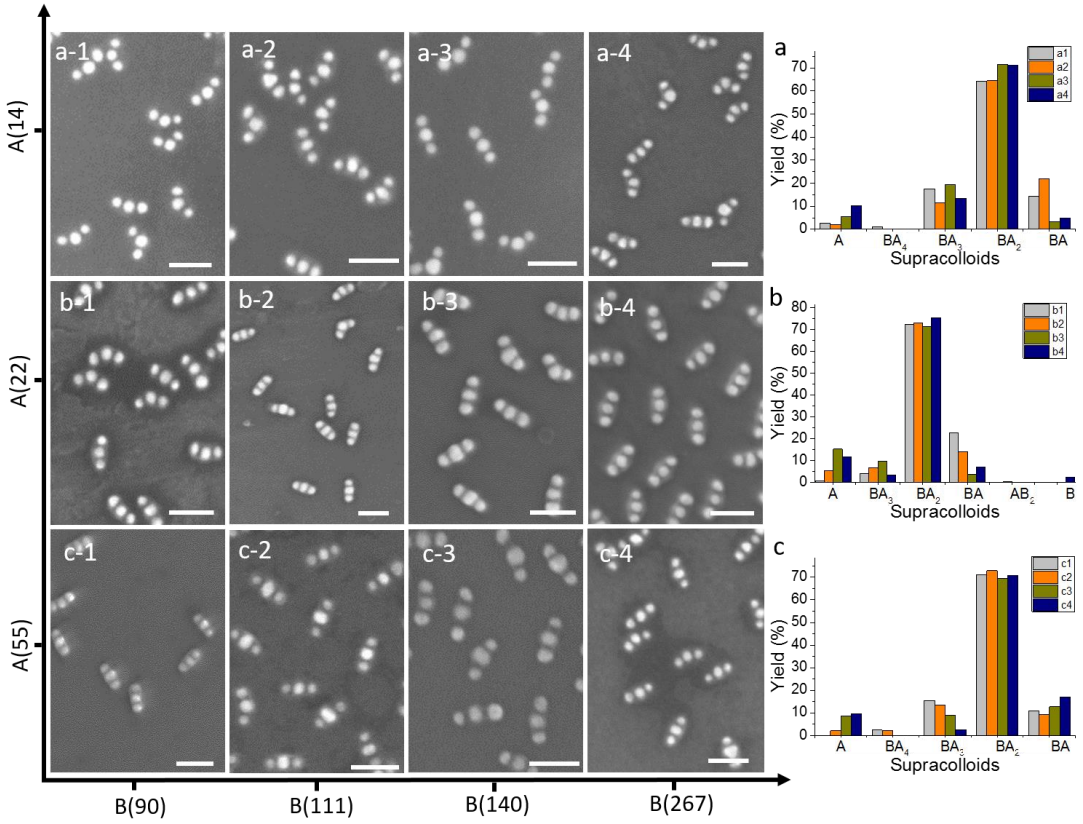

Figure 4.3 Summary of **ABA** trimers with different amphiphilicity. (a1-c4) SEM images of trimers formed by **A** and **B** particles tethered with different polymer length. (a-c) Yield distribution of supracolloids corresponds to the samples on each row.

4.3.3 Effect of hydrophobic polymer length on the formation of ribbons

As discussed in the Chapter 3, the surface chemistry of the supracolloidal trimers is determined by the PEO block of BCPs from the **A** particle and the PS block of BCPs from the **B** particle. Thus, varying the length of the PEO block or PS block will directly impact the relatively hydrophilicity (or hydrophobicity) of the domains within the resulting supracolloids. At the liquid/liquid interface, the hydrophobic attraction from **B** drives the side-by-side association of the hydrophobic center of **ABA** trimers to form ribbons (Figure 4.4).

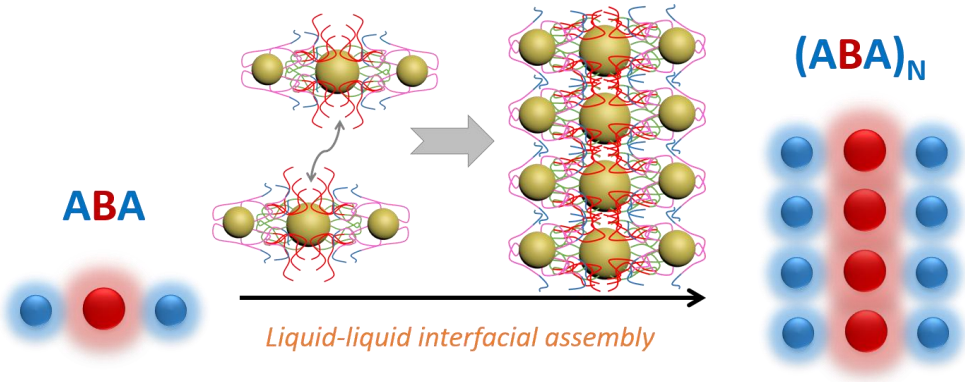

Figure 4.4 Scheme of further assembly of **ABA** to ribbon structures **$(ABA)_N$**.

The assembly of **ABA** supracolloids with varying length of PS block on the central NP (and fixed tether length on **A** NP) was evaluated. The length of the outer PS block of PS-*b*-P(AA-*r*-St)-SH for the **B** particles increased from PS_{90} to PS_{267}, while the length of PEO-*b*-P(DMAEMA-*r*-St)-SH for the **A** particles was fixed to be 22 Kg/mol, as illustrated by the glow range of the red particle. As shown in Figure 4.5 (a-d), a transition from individual trimers (without association), to disordered aggregation of disordered trimers to defined ribbon structures was observed with increasing PS length (see large area SEM images in Figure 4.S5). These results

suggest that the hydrophobic PS block has to be sufficiently long to drive the attraction of the trimers through the hydrophobic center. The average length of the ribbons gradually increased with increasing the PS length (Figure 4.5e and Figure 4.S6). This can be attributed to the stronger hydrophobic attraction that facilitated the growth of longer ribbons. With the stacking of trimers into ribbons, the plasmonic coupling of Au NPs demonstrates a noticeable red shift in the UV-Vis spectrum when compared to trimers, and longer ribbons display stronger red-shift (Figure 4.5f). A broadening of absorption peak was observed for the non-ribbon assemblies **[A(22)B(90)A(22)]$_N$** from trimers with the shortest hydrophobic domain, presumably due to the disordered aggregation of trimers in a small area.

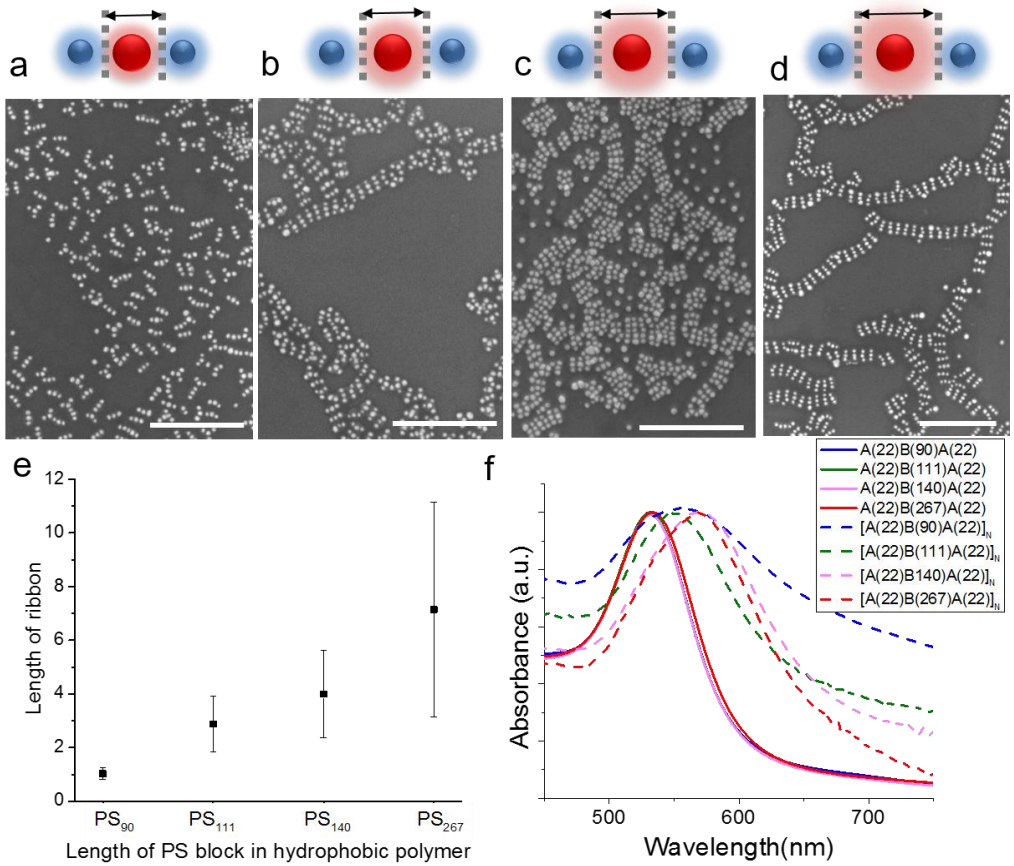

Figure 4.5 Tune the interaction of trimers by changing the length of PS block. (a-d) SEM images of interfacial assembly of **ABA** formed by **A(22)** and **B(90)**, **B(111)**,

B(140), **B(267)**, respectively. Scale bar: 500 nm. (e) Average length of ribbon formed by trimers in sample a-d. (f) UV-Vis spectrum for **ABA** trimers and the corresponding ensembles formed by **B** particles tethered with different hydrophobic polymer lengths.

When pure hydrophilic **ABA** trimers were used, the same assembly procedure did not induce their assembly to form ribbons at the interface (Figure 4.6). Instead, some supracolloidal trimers interacted with impurities (i.e., other types of supracolloids presented in the system, such as **AB** dimers to form short alternating chains. This control experiment further indicates that the hydrophobic force from the **B** particle is the driving force for ribbon formation.

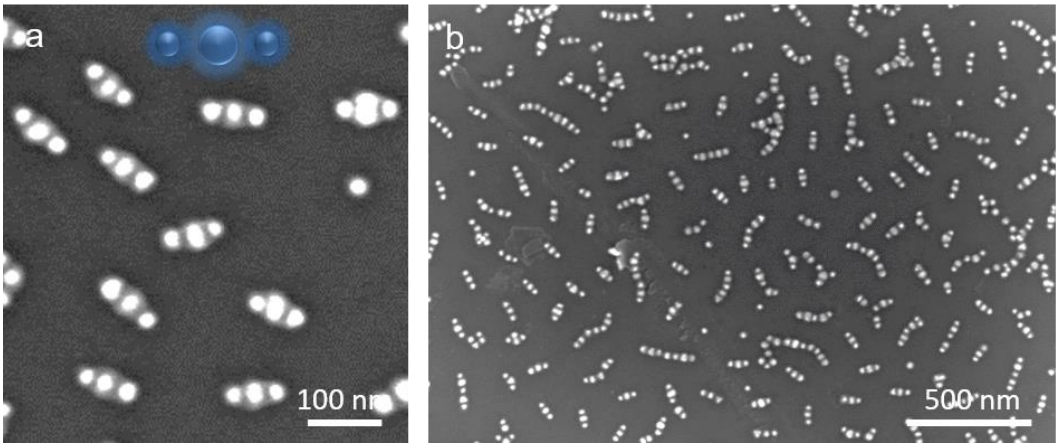

Figure 4.6 Interfacial assembly of hydrophilic trimers **ABA**. (a) SEM image of hydrophilic trimers **ABA** formed by **A(22)** and **B**: 24 nm Au NPs tethered with PEO_{45}-*b*-$P(AA_{0.3}$-*r*-$St_{0.7})_{328}$-SH. (b) SEM image of the interfacial assembly of hydrophilic **ABA**.

4.3.4 Effect of hydrophilic polymer length on the formation of ribbons

We further studied the effect of the randomly-copolymerized block length of the hydrophilic region on the assembly of ribbons from amphiphilic trimers. Figure 4.7 (a-c) exhibits the assembly results of amphiphilic supracolloidal trimers with overall polymer length of PEO-*b*-P(DMAEMA-*r*-St)-SH for **A** particles varied from 14 to 55 Kg/mol, as illustrated by the increasing glow range of blue particles, and a fixed length of PS_{267}-*b*-$P(AA_{0.32}$-*r*-$St_{0.68})_{318}$ for **B** particles, When the length of PEO-*b*-P(DMAEMA-*r*-St)-SH on **A** is short (14 and 22 Kg/mol), the corresponding trimers assembled into defined ribbons (Figure 4.7a,b). However, as the length of PEO-*b*-P(DMAEMA-*r*-St)-SH increased to a certain point (55 Kg/mol), ribbon formation was impeded (Figure 4.7c). We presume that this is caused by the polymer bending toward gaps of NPs as follows. During the formation of supracolloids, the flexible polymer brush on each particle bends toward the gap between the NPs in order to maximize the Lewis acid-base interaction. When the Lewis base-containing block of BCPs (with hydrophilic outer block) is long, more Lewis acids from the complementary BCPs (with hydrophobic outer block) are needed to consume the Lewis bases, resulting in the bending of more hydrophobic polymer brush towards the gap of NPs. The presence of much less residual PS blocks in the center significantly reduces the hydrophobicity of the central **B** particle and the driving force for assembly. In this case, some of the trimers associated randomly to form disordered aggregates (Figure 4.7c). The average ribbon length was found to be increased from 4.9 to 7.2 for samples in Figure 4.7a and b, then decreased to 1.0 for sample 4.7c indicating non-ribbon formation (Figure 4.7d and Figure 4.S7). The UV-Vis spectrum

of trimers and the corresponding assemblies from Figure 4.10 (a-c) is shown in Figure 4.10e, which also supports the ribbon formation or lack thereof compared with well dispersed trimers.

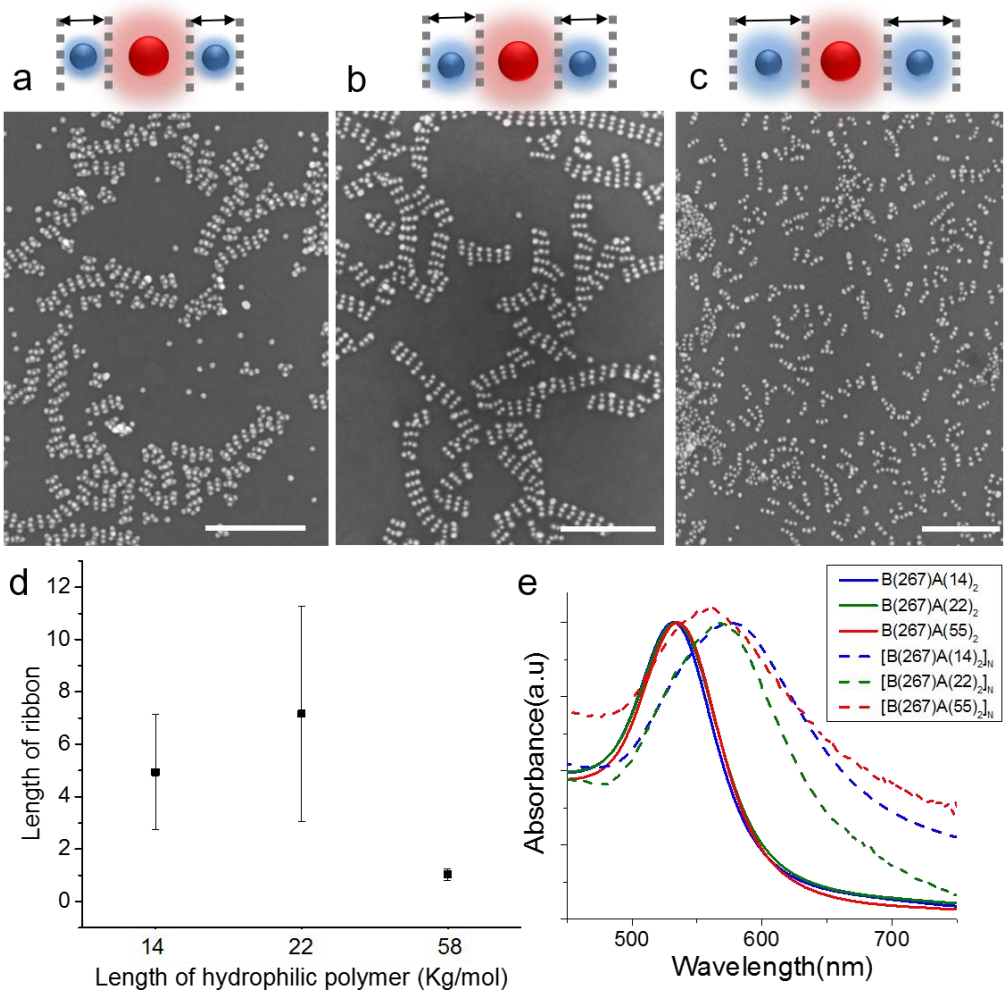

Figure 4.7 Tune the interaction of trimers by changing the length of the hydrophilic polymer. (a-c) SEM images of interfacial assembly of **ABA** formed by **A(14)**, **A(22)**, **A(55)** and **B(267)** from a to c, respectively. Scale bar: 500 nm. (d) Average length of the ribbon formed by trimers in sample a-c. (f) UV-Vis spectrum for trimers **ABA** and the corresponding ensembles formed by **A** tethered with different lengths of hydrophilic polymer.

The polymer bending toward gaps of NPs proposed above was further confirmed by our control experiment. When the length of the hydrophilic polymer on **A** is fixed to be the longest (i.e., 55 Kg/mol), increasing the size of **B** in trimers led to the transition from non-ribbon to ribbon formation (Figure 4.8). This is because the larger **B** particles carry more BCPs and hence Lewis acid groups, which leaves more residual hydrophobic chains unbent and left in the center to provide enough of a driving hydrophobic force.

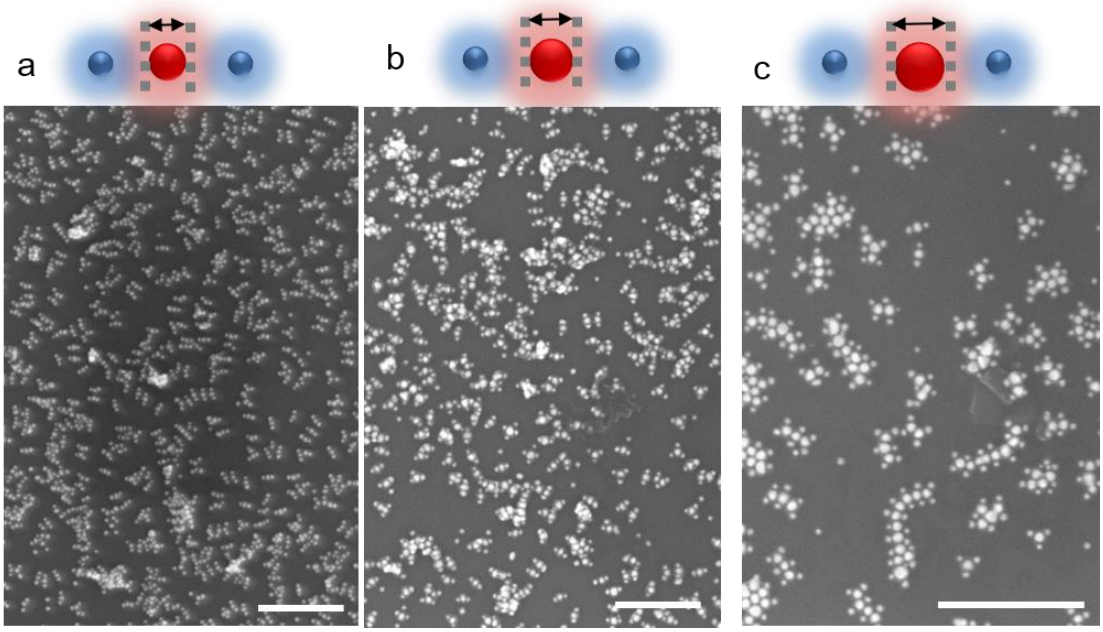

Figure 4.8 Tune the interaction of trimers by changing the size of **B** particle. (a-c) SEM images of interfacial assembly of **ABA** formed by **A(58)** and 24nm (a), 30 nm (b), 36 nm (c) Au NPs tethered with PS_{267}-*b*-$P(AA_{0.32}$-*r*-$St_{0.68})_{318}$ respectively. Scale bar: 500 nm.

4.3.5 Product diagram of ribbon formation

The length effect of BCPs on the assembly of supracolloidal trimers is summarized in a product diagram in Figure 4.9 (see SEM images for each point in Figure 4.S5, 4.S8, and 4.S9). For instance, when the shortest hydrophilic polymer is

used (the column of **A(14)**), all the obtained trimers stack to form ribbons. Capping a longer hydrophilic polymer for **A** led to a transition from non-ribbon to ribbon forming from bottom to top with increasing length of hydrophobic block on **B** (column of **A(22)**). However, when the longest hydrophilic polymer is used in the column of **A(55)**, none of the obtained trimers can further assemble into ribbons.

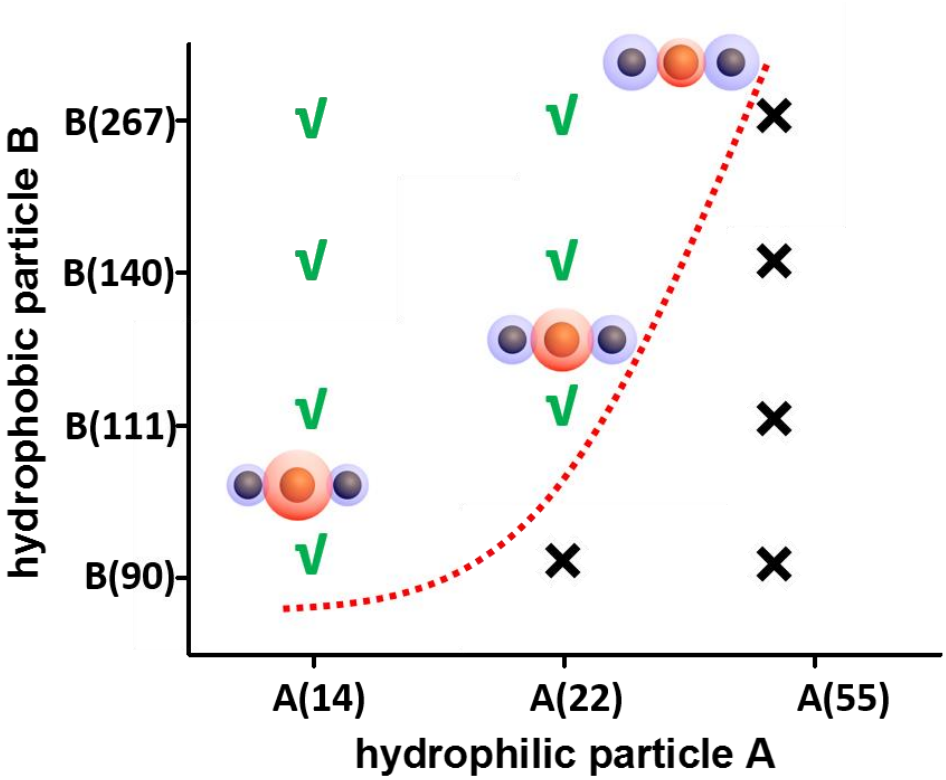

Figure 4.9 Product diagram of ribbon formation dependent on the length of hydrophobic and hydrophilic polymer.

4.4 Conclusion

In summary, we systematically studied the effect of length of BCP tethers on **A** and **B** particle, in order to understanding of the mechanism of ribbon formation. A product diagram was generated to summarize ribbon formation or lack thereof with

varying polymer length on **A** and **B**. Our results suggest that the hydrophobic brushes in the central particle function are the major driving force for ribbon assembly. Moreover, the redistribution of the hydrophobic brushes from polymer bending toward the gap of NPs also plays an important role in the ribbon formation, due to the associated change in the hydrophobicity of central **B** particle. The self-assembled ribbon structures show tunable plasmonic coupling, which may find applications in nanophotonics. This strategy can be extended to the assembly of amphiphilic supracolloids with different valences and symmetry.

Chapter 5: pH effect on the interfacial assembly of amphiphilic supracolloidal trimers

Overview. In previous chapters, we have introduced the design and interfacial assembly of amphiphilic supracolloids and explored the effect of NP size and BCP length on assembly. This chapter focuses on understanding the pH effect of the aqueous phase on the interfacial assembly of amphiphilic trimers. Depending on the pH value, the assembly of the same type of trimers were found to associate in different modes (i.e., side-by-side stacking or end-to-end association) to form either ribbons or linear chains.

A manuscript based on this chapter is in preparation to be submitted to ACS *Nano*.

5.1 Introduction

Controllable synthesis and association of materials in response to external stimuli, as one of the essential biological functions, has been a driving inspiration in designing responsive systems in nano-science.[112] The application of this process in the self-assembly of nanomaterials can result in programmable assembly or disassembly of building blocks with response to external stimuli. Toward this goal, various interactions have been explored to for responsive self-assembly, including complimentary bonding of DNA, antibody-antigen recognition, conjugating proteins, and stimuli-responsive polymers.[113]

Among different ligands, polymers that are responsive to stimuli (e.g., temperature, light, chemicals and biomolecules)[114] have been used drive the reversible assembly of NPs due to their diversity in composition, functionality, and mesoscopic structure.[115] Grafting of inorganic NPs with responsive polymer brushes

enables the design of assembly and/or disassembly of polymer tethered NP in response to external stimuli. For example, plasmonic vesicles can be designed to be responsive to pH by assembling Au NPs tethered with binary polymer brushes.[116] The hydrophobic to hydrophilic transition of the hydrophobic brushes in acidic environments triggers the dissociation of plasmonic vesicles to release encapsulated therapeutic agents. However, to realize diverse assembly morphologies and hierarchical assembly behavior in response to one type of stimuli is still the challenge on in the stimuli responsive assembly of hairy NPs.

Here we systematically investigated the pH effect of the bottom aqueous phase on the interfacial assembly of amphiphilic **BAB** supracolloids. The supracolloids consist of a hydrophilic center symmetrically bonded with two hydrophobic ends at both poles. In acidic condition, the hydrophobic domains of trimers associated in end-to-end mode to assemble into linear chains at the interface. The chains started to form branches when the pH decrease, due to strengthened hydrophobicity and weakened electrostatic repulsion on **B** particles. In contrast, in basic condition, the protonation of the residue –COOH on the terminal hydrophilic NPs and –N(Me)2 on the central hydrophobic NPs caused the decrease in the relative amphiphilicity of the **BAB**, inducing the side-by-side association of trimers to form stacked ribbons (Figure 5.1).

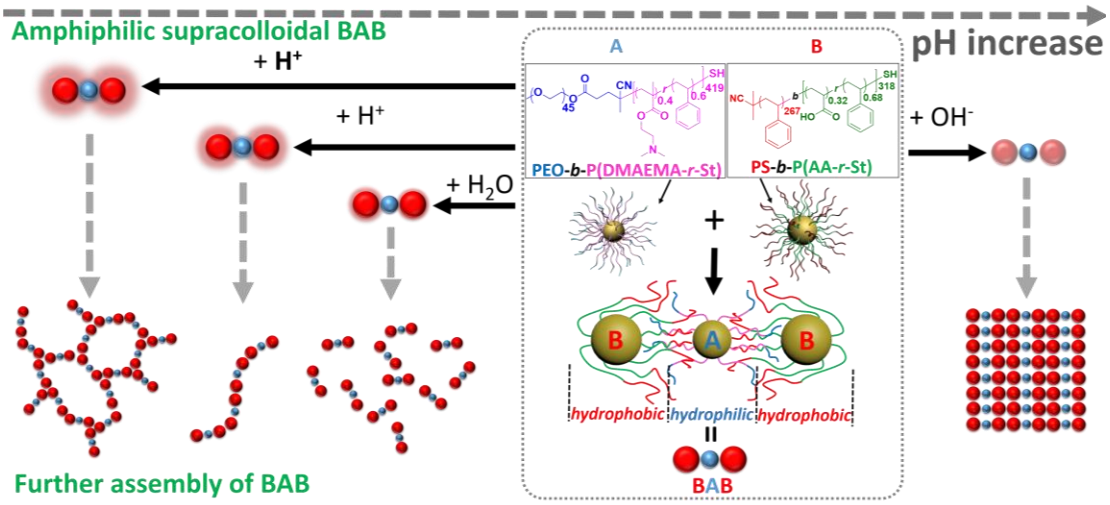

Figure 5.1 Scheme of pH responsive assembly of amphiphilic trimer **BAB**.

5.2 Experiments

5.2.1 Materials

The BCPs, thiol-terminated PEO-*b*-P(DMAEMA-*r*-St)-SH and PS-*b*-P(AA-*r*-St)-SH, and Au NPs with diameter of 20 nm and 24 nm were synthesized by the same method described in experimental section in Chapter 2. See Table 2.1 for the parameter and symbol of PEO-*b*-P(DMAEMA-*r*-St)-SH and PS-*b*-P(AA-*r*-St)-SH with different lengths. Hydrochloric acid (36.5-38.0%), sodium hydroxide, sodium chloride were purchased from Sigma Aldrich and used as received unless otherwise noted. Deionized water (Millipore Milli-Q grade) with resistivity of 18.0 MΩ was used in all the experiments.

5.2.2 Building amphiphilic trimers by self-assembly of A and B

Amphiphilic trimers was obtained by co-assembly of BCP tethered Au NPs in THF, as described in Chapter 2. Taking the formation of **BAB** for example, 1 mL of

20 nm **A** NPs capped with polymer P3 (0.05 mg·mL^{-1}) were directly mix with 3.5 mL of 24 nm **B** NPs capped with polymer N4 (0.05 mg·mL^{-1}) in THF. The mixture was sonicated for 20 sec, and then incubated for 2 hr. The sample was imaged by SEM and TEM to statistically analyze the yield of supracolloids.

5.2.3 Liquid-liquid interfacial assembly of trimers

Hierarchical assembly of trimers was performed by liquid-liquid interfacial assembly. Briefly, 1 mL of **BAB** trimers dispersed in THF was added to a mixture of 4 mL of a saturated sodium chloride solution and a 1M HCl or NaOH aqueous solution of various volume. Consequently, an interface was formed between the two liquids due to the incompatibility of THF and the dense salt solution. Then the mixture was capped and incubated until all the THF was evaporated. Afterwards, the ensembles was left floating on the surface of the salt solution. The sample was imaged by SEM to analyze the structure of ensembles.

5.2.4 Sample preparation for characterizations

BCPs were characterized by ^{1}H NMR and GPC, the grafting density of BCPs on Au NPs was characterized by TGA, pH responsiveness of hybrid building blocks **A** and **B** was characterized by zeta potential, amphiphilic **ABA** trimers and the ribbons structures were studied by zeta potential measurement, DLS, UV-vis Absorption spectroscopy, SEM and TEM, the sample preparation was described in chapter 2 and 3.

5.3. Results and discussion

5.3.1 Generation of amphiphilic trimers BAB

The hybrid NPs used for forming **BAB** are **A**: 20 nm Au NPs tethered with polymer P3 and **B**: 24 nm Au NPs tethered with polymer N4. Amphiphilic **BAB** trimers were generated by mixing hybrid NPs **A** and **B** in THF. The SEM and TEM images in Figure 5.2 implies a linear morphology and individual dispersion of the trimers. The polymer shell both drives the colloidal reaction of **A** and **B** and stabilize the supracolloids as a protecting shell. Statistical analysis further shows a yield of 80%, as shown in Figure 5.2c. The formation of trimers was also characterized by change in hydrodynamic diameter from hybrid NPs to trimers. As shown in Figure 5.2d, the generation of **BAB** trimers was confirmed by the shift of peaks before and after the colloidal reaction. The zeta potential was also measured to track the assembly, as shown in Figure 5.S1. The zeta potential of **A** and **B** in THF is +5 and -58 meV respectively; however, after the formation of **BAB** trimers, the zeta potential falls to -20 meV due to the neutralization of the carboxylic and tertiary amino groups.

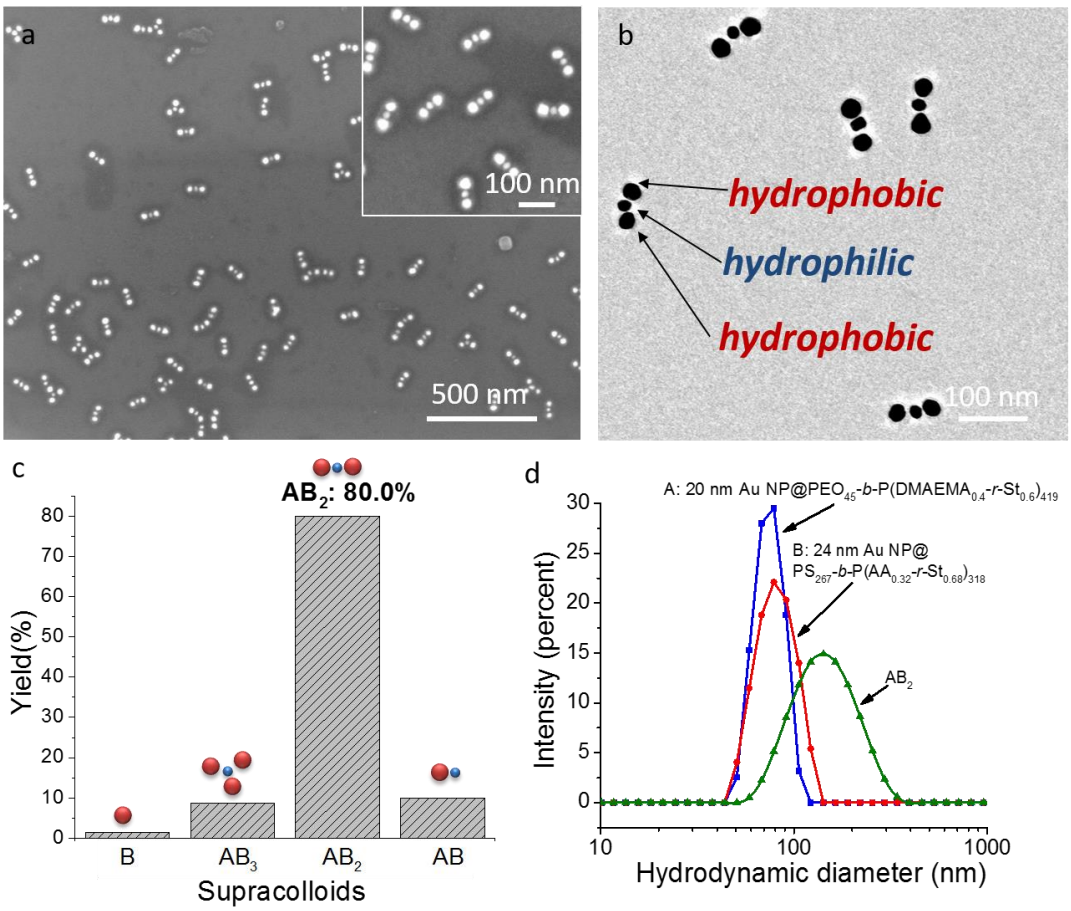

Figure 5.2 Characterization of amphiphilic trimers **BAB**. (a-b) SEM (a) and TEM (b) images of trimers **BAB**. (c) Yield distribution of supracolloids. (d) Hydrodynamic diameters of hybrid building block **A**, **B** and amphiphilic trimers **BAB**.

5.3.2 The pH effect on the assembly of amphiphilic BAB trimers

The obtained amphiphilic **BAB** trimers were used as building blocks to undergo interfacial assembly described in previous chapters. Before the placement of trimers in THF on top of water phase, predetermined amount of HCl and or NaOH were added into the salt-saturated solution to reach a varying $[H^+]$ or $[OH^-]$ in the range of 0~0.3M in aqueous phase. Then, **BAB** trimers in THF were placed on top of a saturated sodium chloride solution to trigger the hydrophobic assembly of trimers at

the interface. After the slow evaporation of THF, the ensembles floating on the aqueous phase was obtained, where accumulated with hierarchical assembly structures of **BAB**.

The zeta potential change of **A** and **B** in response to the addition of acid was studied in Chapter 3 (Fig 3.6), which reveals a gradual increase on zeta potential for both **A** and **B** with addition of acid. Here, the zeta potential change of the **A** and **B** NPs in response to addition of base is also studied, as shown in Figure 5.3, using triethylamine as the source of base. Adding triethylamine to the **A** particles didn't influence the zeta potential, which only fluctuated around the neutral state. Conversely, **B** particles which were negatively charged in pure THF and became more negative upon addition of base due to the deprotonation of the carboxyl groups.

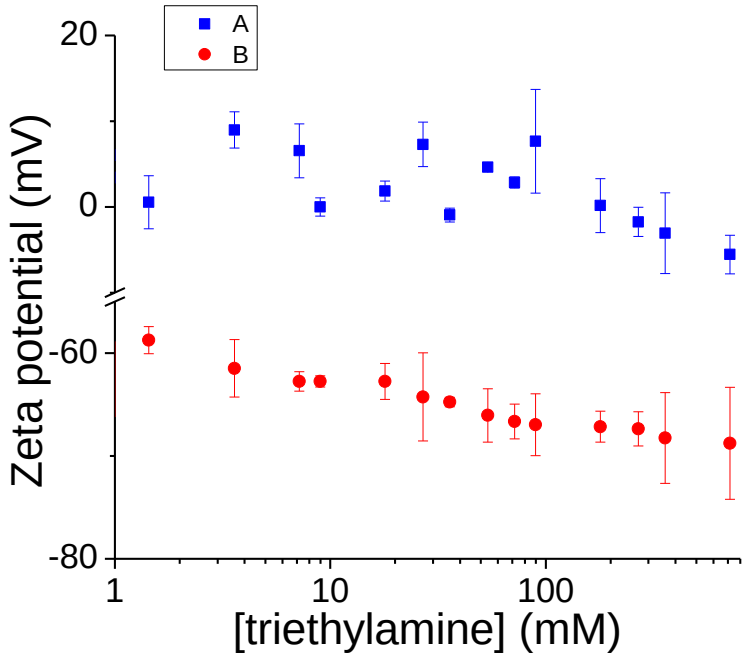

Figure 5.3 Zeta potential change of **A** and **B** particle with addition of base.

As reflected by the zeta potential change of **A** and **B** in response to acid/base, the addition of acid or base affects the ionization status of the residues of Lewis acid/base groups of BCPs within supracolloids. As a result, the hydrophobicity of corresponding hydrophilic/hydrophobic regions of the **BAB** trimers is varied, thus changing the association mode of supracolloids in the course of assembly. As shown in Figure 5.4a-e, the assembly structures of $\mathbf{(BAB)_N}$ exhibited a transition from ribbon stacking to chain formation and eventually branching network formation with decreasing pH (see large area SEM images in Figure 5.S2).

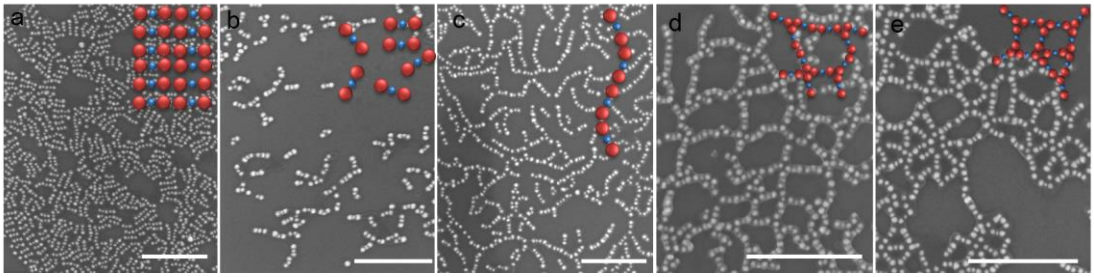

Figure 5.4 Tune the assembly of **BAB** by adding acid/base. (a-e) SEM images of interfacial assembly of **BAB**. The concentration of acid or base is $[OH^-]$=0.2M, $[H^+]$=0, $[H^+]$=0.2 M, $[H^+]$=0.3M from a to e, respectively. Scale bar: 500 nm.

In a basic environment, ionization of the residual carboxylic groups on hydrophobic particle **B** reduced the hydrophobicity of **B**, due to the presence of more surface charges. As a result, the amphiphilicity of **BAB** trimers was not sufficiently strong to induce the association of the **B** particles. Instead, the interactions between trimers became more isotropic, which stacked trimers into parallel ribbons (Figure 5.4a). In a neutral environment, the hydrophobic force became stronger; however, only a few **BAB** trimers were connected end-to-end to form short chains via hydrophobic poles (Figure 5.4b). Conversely, the addition of acid made the terminal

B particles more hydrophobic, due to the protonation of the carboxylic groups of **B**. In this case, the hydrophobic **B** particles became "stickier" to drive the formation of longer chain structures (Figure 5.4c). The further addition of more acid induced the branching of chains to form networks, because the hydrophobic force was strongly enough to cause aggregation of three or more **BAB** simultaneously (Figure 5.4d). The degree of branching was found to increase with increasing the amount of added acid (Figure 5.4e).

To statistically characterize the chain and network structures, we studied chain length (i.e., the number of **BAB** trimers between two intersections) in respond to addition of acid. As shown in Figure 5.5, the average chain length increased from ~1 to 3 with the addition of acid due to the effective chaining of **BAB** under acidic environment. With more acid added, the chain length actually decreased due to increased branching upon further addition of acid.

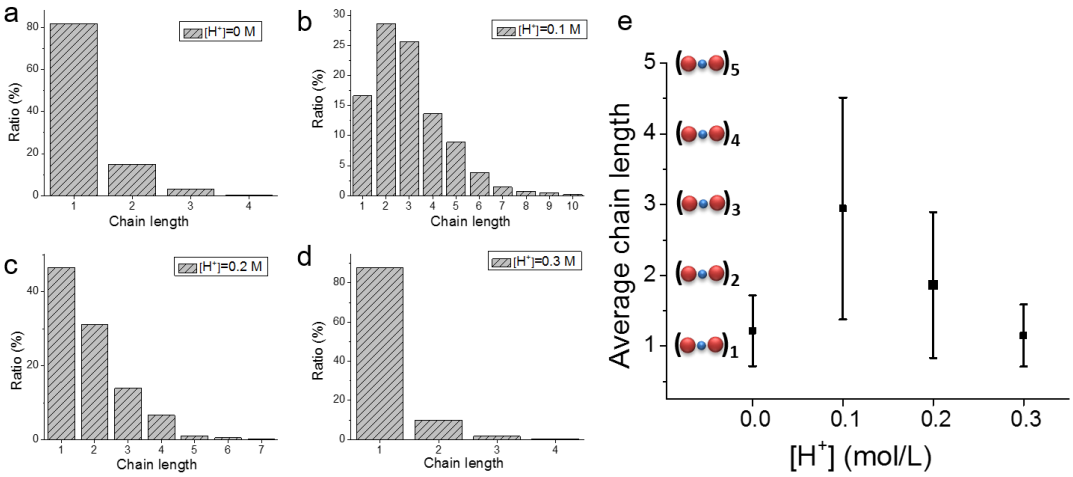

Figure 5.5 (a-d) Chain length distribution for $\mathbf{(BAB)_N}$ in response to different $[H^+]$. The concentration of acid or base is 0, $[H^+]$=0.1 M, $[H^+]$=0.2 M, $[H^+]$=0.3M from a to d, respectively. (e) Average chain length respond to the concentration of acid.

The branching of the chains is more obvious when we analyzed the degree of branching, α, which is defined as the number of **BAB** trimers gathered at every intersection in the network structure. Thus, α = 1, 2, 3 means no chaining of trimers, linear unbranched chains, and a branched networks. The average branch degree was found to increase with the increase of [H^+], reflecting a gradual increase in hydrophobic attraction of the **B** particles (Figure 5.6). The detailed distribution of branch degree can be found in Figure 5.6a-d.

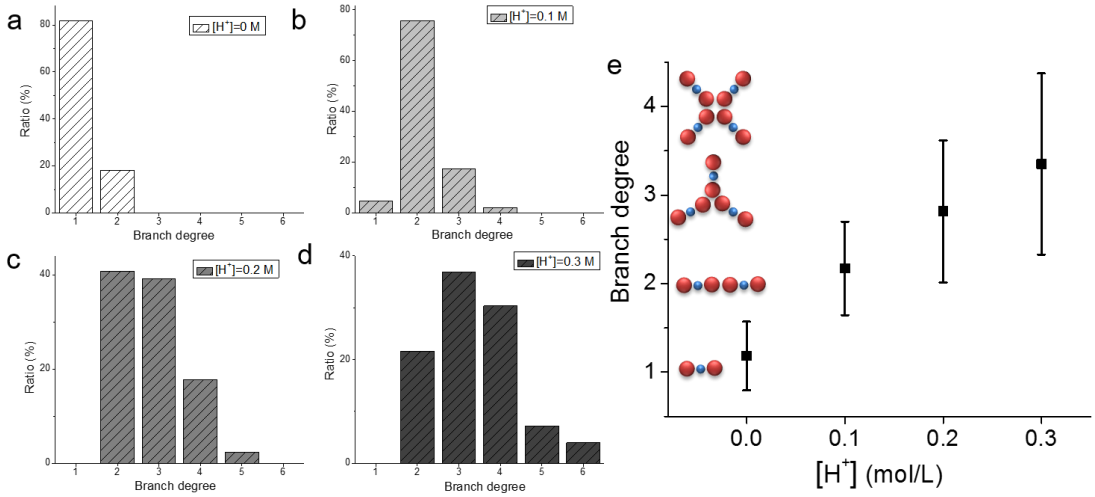

Figure 5.6 (a-d) Branch degree distribution for **(BAB)$_N$** in response to different [H^+]. The concentration of acid or base is 0, [H^+]=0.1 M, [H^+]=0.2 M, [H^+]=0.3M from a to d, respectively. (e) Average branch degree respond to the concentration of acid.

The different assembly morphologies give rise to different collective optical properties, as shown in Figure 5.7. The hierarchical assembly of **BAB** trimers exhibits a strong red shift compared to **BAB** trimers in THF. Increasing the [H^+] led to the stronger red-shift for **(BAB)$_N$**, The larger red-shift can be attributed to the combination effect of increased degree of branching (i.e., average aggregation number) and closer interparticle distance.

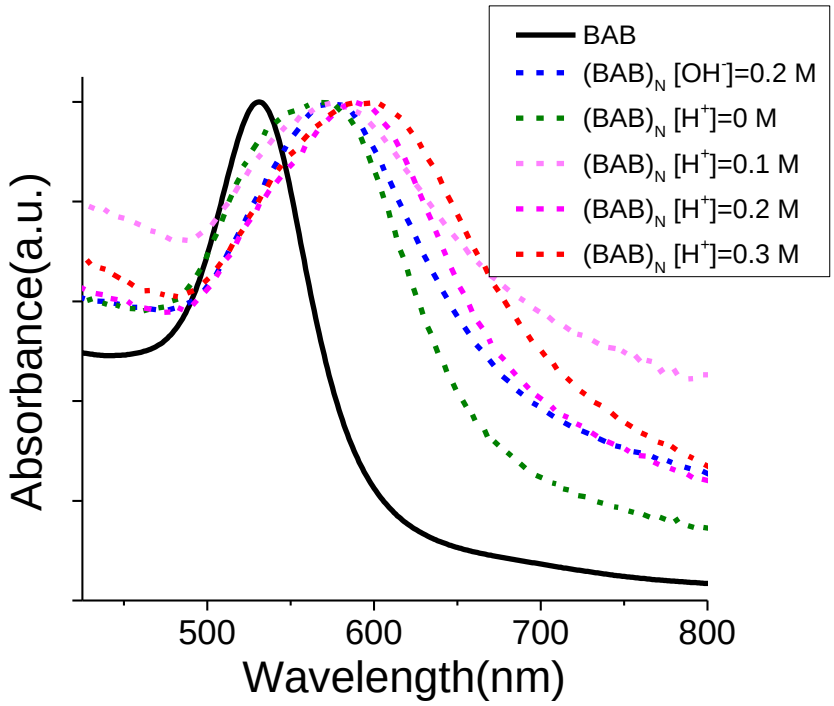

Figure 5.7 UV-vis spectrum of **BAB** and the interfacial assemblies **$(BAB)_N$** with different amount of acid/base added.

5.3.3 The pH responsive assembly of amphiphilic trimers ABA

ABA trimers with opposite hydrophobicity distribution were also used to study their responsive assembly under different pH. As shown in Figure 5.8, a high yield of **ABA** (78%) was achieved utilizing **A**: 20 nm Au NPs tethered with P2 and **B**: 24 nm Au NPs tethered with N2. The formation of **ABA** trimers was also confirmed by the measurement of the hydrodynamic diameter (Figure 5.8d) and zeta potentials (Figure 5.S3) of individual **A** and **B** particles and assembled supracolloids.

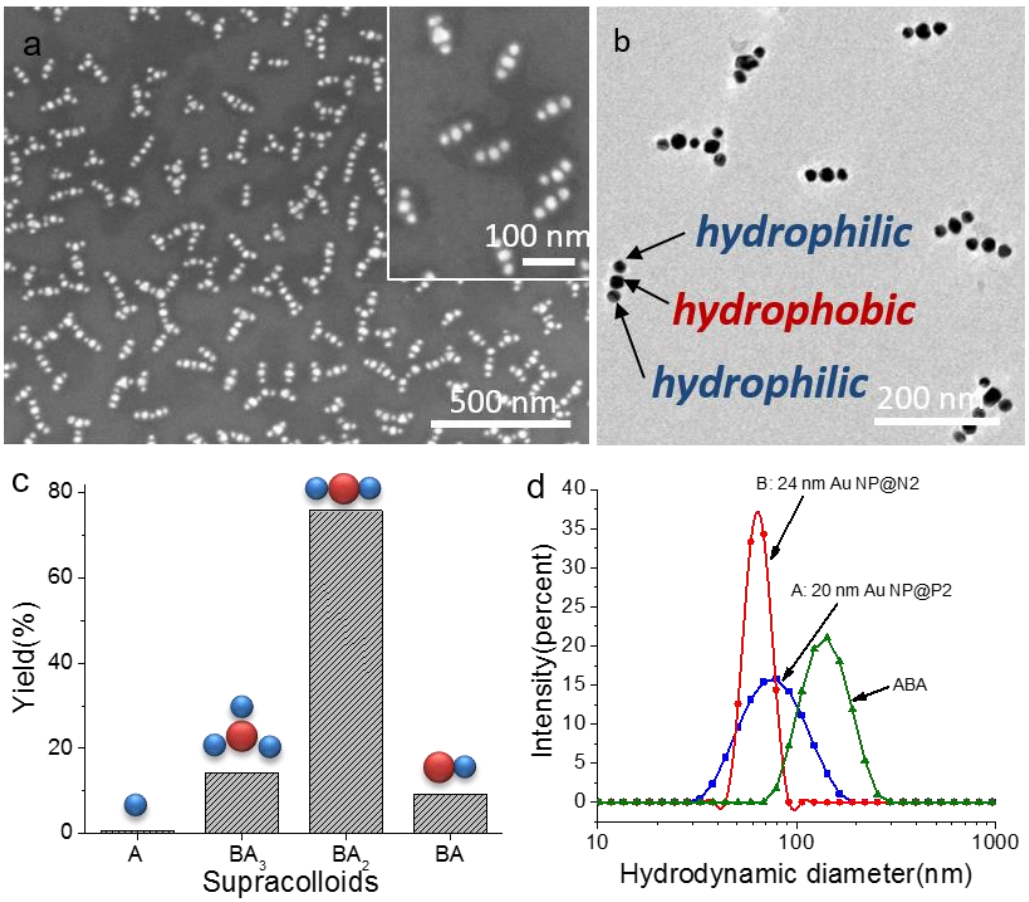

Figure 5.8 Characterization of amphiphilic **ABA** trimers. (a-b) SEM (a) and TEM (b) images of **ABA** trimers. (c) Yield distribution of supracolloids. (d) Hydrodynamic diameters of hybrid building block **A**, **B** and amphiphilic **ABA** trimers.

The interfacial assembly of **ABA** trimers exhibited a transition from ribbon formation to chain formation in response to the addition of acid or base (Figure 5.9a). Upon addition of acid, the hydrophobic center became stickier resulting in a side-by-side connection of trimers (Figure 5.9b), as described in previous chapters. When no acid was added, the hydrophobic interactions arisen from central **B** were not strong enough, leaving most trimers irregularly distributed (Figure 5.9c). Conversely, adding base largely improved the ionization of **B** particles via deprotonation of carboxyl group, thus reducing the hydrophobicity and increasing the repulsion of the **B**

particles due to the stronger negative charge. Consequently, repulsion between the **B** particles was strong enough to push the **B** particles away from each other, resulting in the end-to-end association of the trimers (Figure 5.9d). A control experiment of further **ABA** assembly by varying the length of polymer on **B** particles was conducted (Figure 5.S4). The reason for forming chain structures in basic environment was attributed the electrostatic repulsion prevails upon hydrophobic attraction on **B**, an increase in the length of the polystyrene block on the **B** particles gradually intensify the hydrophobic attraction, and thus lead to the loss of balance for end-to-end connections. As shown in Figures 5.S5b-c, when the length of polystyrene block was sufficient, the repulsion between **B** particles was not strong enough to separate trimers, so a disordered structure was formed.

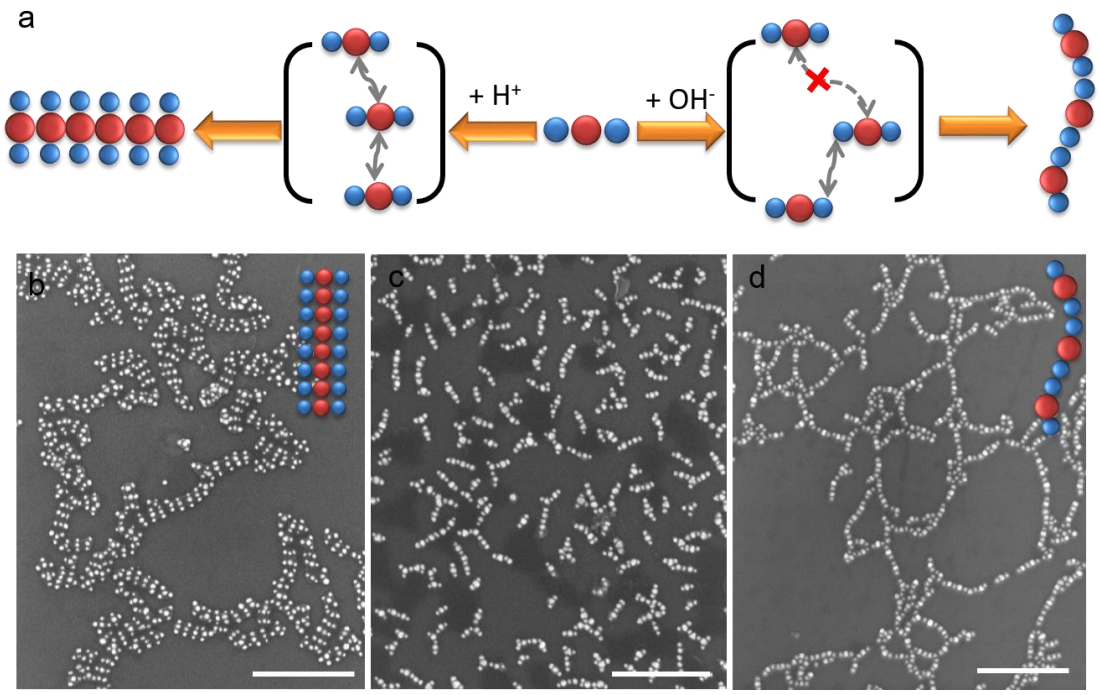

Figure 5.9 pH responsive assembly of amphiphilic trimers **ABA**. (a) Scheme of tuning the assembly of **ABA** by adding acid/base. (b-d) SEM images of interfacial assembly of **ABA** formed by **A**: 20 nm Au NPs tethered with P2 and **B**: 24 nm Au

NPs tethered with N2.The concentration of acid or base is [OH^-]=0.2M, 0, [H^+]=0.2 M from b to d, respectively. Scale bar: 500 nm.

A study on the aggregation number in both ribbon and chain structures is illustrated in the distribution in Figure 5.10. Ribbon/chain length is denoted as the number of **ABA** trimers in the ribbon or chain formed after the interfacial assembly. The average aggregation number in ribbon and chain structure were calculated to be 2.6 and 2.4 respectively based on the distribution in Figure 5.10a. The corresponding response in absorption for **ABA** and their hierarchical assembly structures is shown in Figure 5.10b, which reveals the red-shift for hierarchical structures. As shown, the red-shift for the ribbon structure is stronger than that of the chains due to the closer interparticle distance in the ribbon structure.

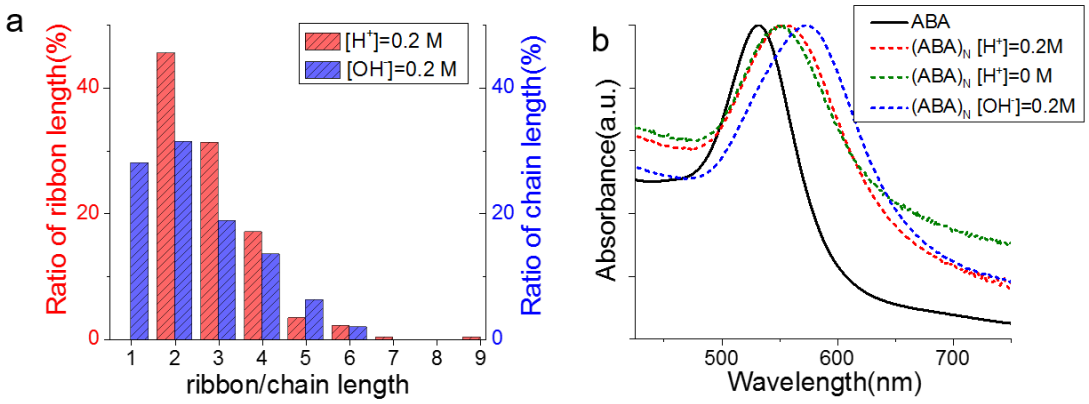

Figure 5.10 (a) Chain/ribbon length distribution of **$(ABA)_N$** with adding acid/base. (b) UV-vis spectrum of **ABA** and the interfacial assemblies of **ABA** with acid/base added.

5.4 Conclusion

In conclusion, we systematically studied the effect of adding acid/base to aqueous phase on the association manners of amphiphilic trimers during liquid-liquid interfacial assembly. More importantly, the trimers show pH-responsive assembly due to the amphiphilicity change in response to the addition of acid or base. The **BAB** trimers with hydrophobic ends undergo a transition from stacked ribbons to chains and networks with decreasing pH, and the **ABA** trimers with hydrophobic centers show the transition from chain to ribbon structures with decreasing pH. The new family of stimuli responsive anisotropic colloidal molecules paves an avenue for the fabrication of numerous hierarchical structures starting from the assembly of readily available spherical NPs.

Chapter 6: Conclusions and future work.

6.1 Conclusions

The objective of this dissertation was to develop an effective and robust method for constructing colloidal molecules with defined valences and region-selectively tunable surface chemistry, and for the further controllable assembly of such supracolloids into defined structures at the interface. First, we generated a series of supracolloids with controlled valence by co-assembly of binary NPs grafted with complementary BCPs. Combinations of Lewis acid and Lewis base-containing BCPs were designed to guide the co-assembly of binary NPs. The neutralization of reactive moieties on complementary BCP-grafted NPs drives their assembly to produce a range of supracolloids with defined valence in high yields, including dimers, trimers, tetramers, pentamers, and alternating chains. The supracolloids exhibit amphiphilic feature that is originated from the outer block of BCPs on the surface of NPs. The domain size and composition of NP subunits and valence in supracolloids can be tuned by varying the size and composition of NPs, as well as length and composition of BCP tethers. Second, we demonstrated the hierarchical assembly of the obtained supracolloids into a rich variety of structures at a higher hierarchy level. Amphiphilic dimers assembled into petal-like structures, where hydrophobic particles aggregate in the core, and hydrophilic particles face the outside. Trimers with hydrophobic ends and a hydrophilic center underwent end-to-end association to form chain structures, while trimers with a hydrophobic center and hydrophilic ends employed a side-by-side association to form ribbon structures. Third, we focused on understanding the formation mechanism of the ribbon structure by examining the effect of BCP lengths

on the assembly process. It was found that longer hydrophobic block on **B** particle and the shorter hydrophilic polymers on **A** particles would facilitate the stacking of trimers into ribbons. The result suggests that hydrophobic attraction arising from hydrophobic brushes on the central particle is the major of driving force for assembly, while the redistribution of polymer brushes in the gap between NPs impacts the relative hydrophobicity of central **B** particle and hence assembly behaviors of supracolloids. Fourth, we further studied the effect of pH on the responsive assembly of amphiphilic trimers by addition of acid or base to aqueous phase in liquid-liquid interfacial assembly. The assembly of trimers with hydrophobic ends undergo a transition from stacked ribbons to chains and networks with decreasing pH, and the assembly of trimers with hydrophobic centers show the transition from chain to ribbon structures with decreasing pH. The responsive assembly is due to the change of ionization state of polymer brushes upon adding acid/base, and the consequential change on the amphiphilicity of trimers. This research introduces an efficient and robust way to prepare a series colloidal molecules with well-defined valence in high yields. More importantly, the hierarchical assembly of the supracolloids generates a series of superstructures with tunable optical properties.

6.2 Future work

6.2.1 Interfacial assembly direction

As we discussed in previous chapters, tethering NPs with well-designed functional polymers offers a powerful strategy to assemble NPs into colloidal molecules that can further assemble in hierarchical level architectures. The supracolloids we used for 2nd-level assembly were mostly dimers and trimers which

have already led into diverse superstructures with higher complexity. This spontaneously inspires us that more sophisticated hierarchical structures might be obtained if the building blocks containing higher valances are used. In chapter 2, we have produced symmetric tetramers and pentamers with tunable surface amphiphilicity. Taking the further assembly of tetramers as an example, trigonal planar shaped tetramers with hydrophobic terminals and a hydrophilic core (**AB_3**) are expected to undergo end-to-end connections to form a close-packed film of ordered tetramers. Additionally, tetramers with a hydrophobic core and hydrophilic terminals (**BA_3**) might stack core-by-core to form a three dimensional ladder structure, as shown in Figure 6.1. The preliminary result for further assembly of **BA_3** tetramers was obtained (see Figure 6.S1), where the 3D stacking of tetramers was observed.

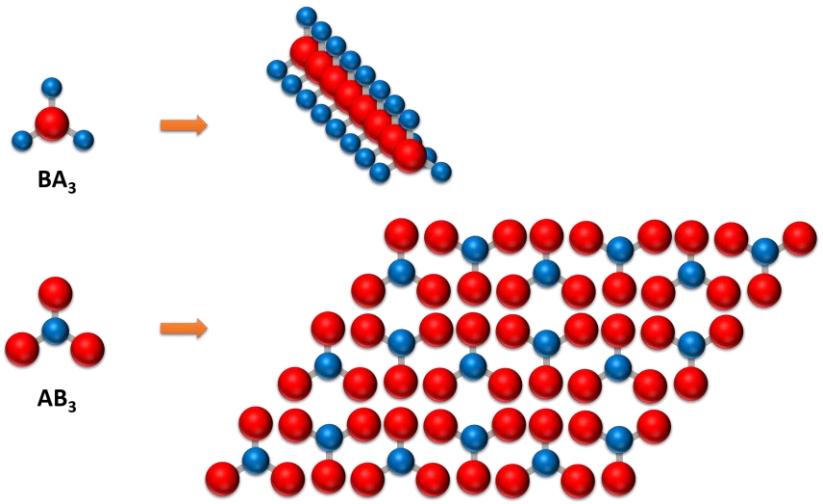

Figure 6.1 Scheme of further assembly of amphiphilic tetramers.

6.2.2 Solution phase assembly direction

The strategy we used for the second stage assembly is a liquid-liquid interfacial assembly, which gradually changed the solvent quality for supracolloids in organic phase. The interfacial assembly was demonstrated to be an effective way to trigger

the further assembly of amphiphilic supracolloids; however, it largely limits the assembly to only form two dimensional structures. A solution phase assembly presents a promising strategy for generating 3D superstructures or activating different association manners. First, the solution phase breaks the dimensional limit of the interface, which allows the construction of ensembles in larger space. Moreover, the interactions of supracolloids in aqueous solution are expected to be different from those at interface, owing to the much stronger ionization of the charged block and the collapse of the hydrophobic block. We already prove this concept by dialysis of the supracolloids against an aqueous solution, which gives rise to network structures with a tunable ratio of each NP, as shown in Figure 6.2.

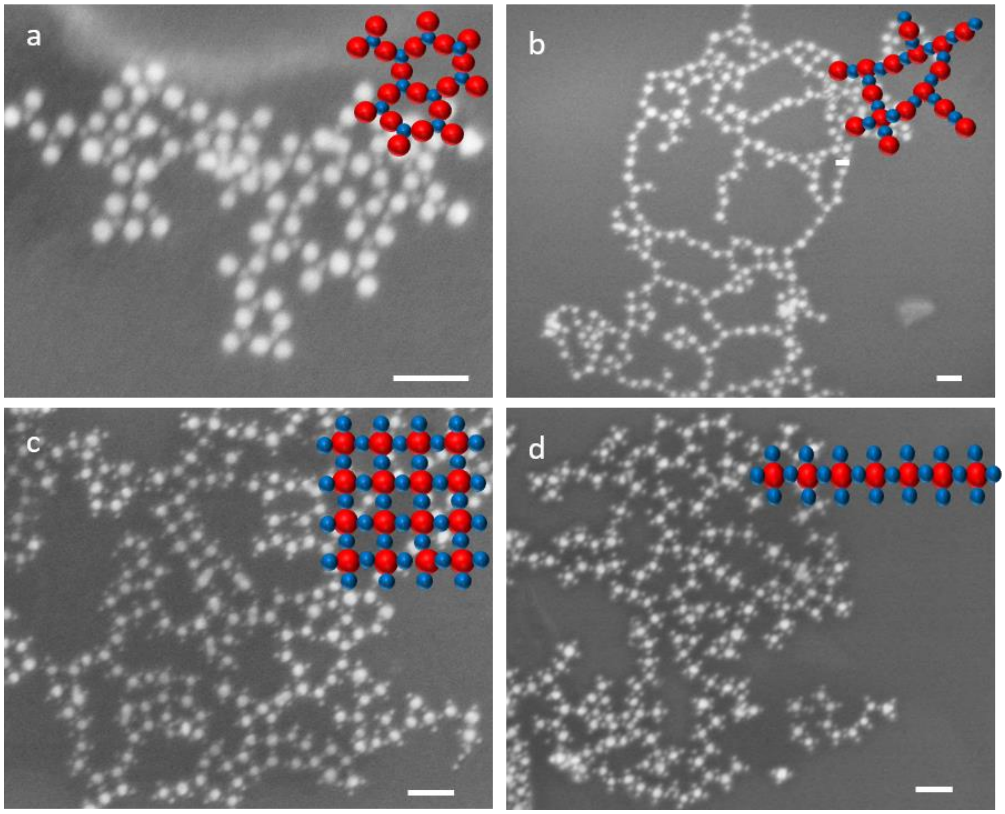

Figure 6.2 SEM image of network structure formed by dialysis supracolloids against sodium citrate solution (1/1000 mass ratio). The supracolloids were formed by self

assembly of **A**: 15 nm Au NP tethered with PEO_{45}-*b*-P($DMAEMA_{0.2}$-*r*-$St_{0.8}$)$_{400}$ and **B**: 24 nm Au NP tethered with PS_{111}-*b*-P($AA_{0.31}$-*r*-$St_{0.69}$)$_{289}$. From a to d, the feeding ratio of **A/B** is increasing.

6.2.3 External field assisted assembly direction

Our existing work utilizes Au NPs as a model system for demonstration of assembly strategies. Extraordinary optical properties have been observed in the resulting assemblies due to the plasmon coupling between NPs. When NPs with other compositions (e.g., Fe_3O_4 NP) are used, they are expected to give a much richer space for tuning interparticle forces, thus leading to more sophisticated or defined assembly structures. Singh *et al.* previously achieved helical structure from magnetic NCs under a magnetic field by the competition between shape anisotropy and magnetocrystalline anisotropy.[42] We have shown the successful preparation of heterogeneous dimers and trimers of Au and Fe_3O_4 NPs in chapter 2. When these heterogeneous supracolloids are used as building blocks, the application of magnetic field might give rise to complex superstructures that cannot be obtained by Au supracolloids, owing to the competition between magnetic, electrostatic, and hydrophobic forces.

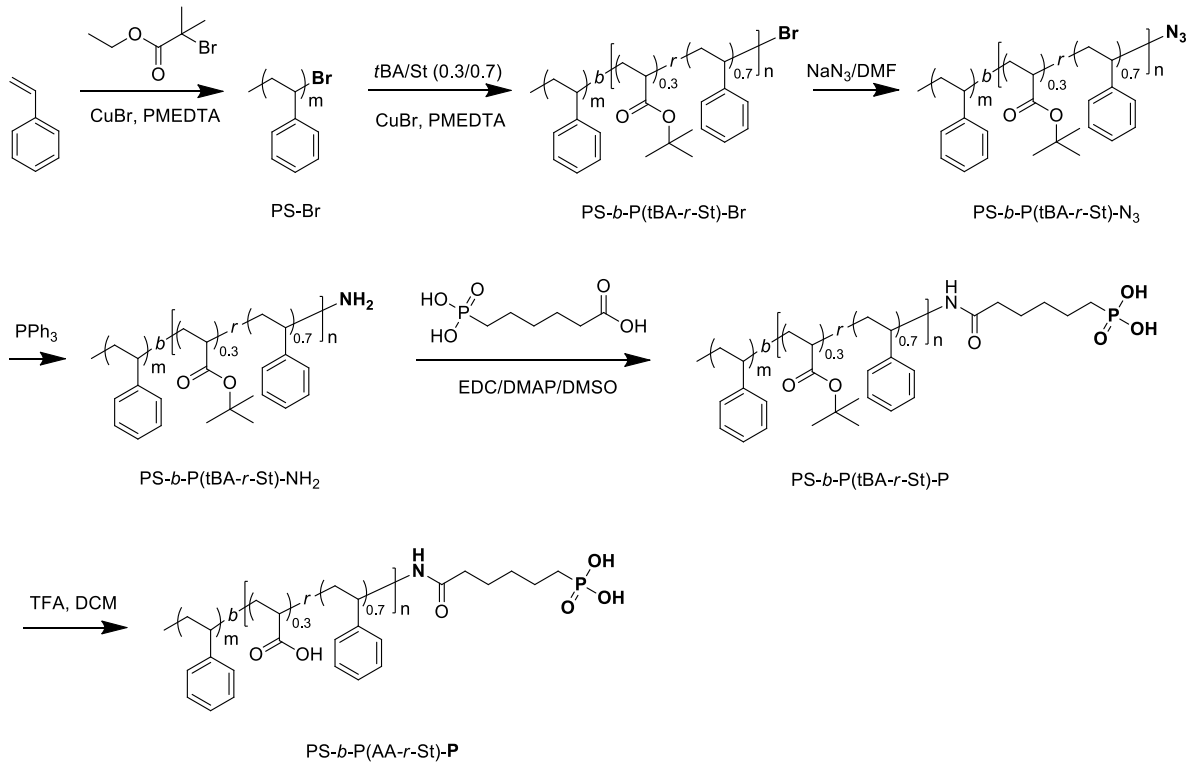

Figure 2.S1 The synthetic routes of phosphonate BCPs: PS-*b*-P(*t*BA-*b*-St)-P to modify Fe_3O_4 NPs.

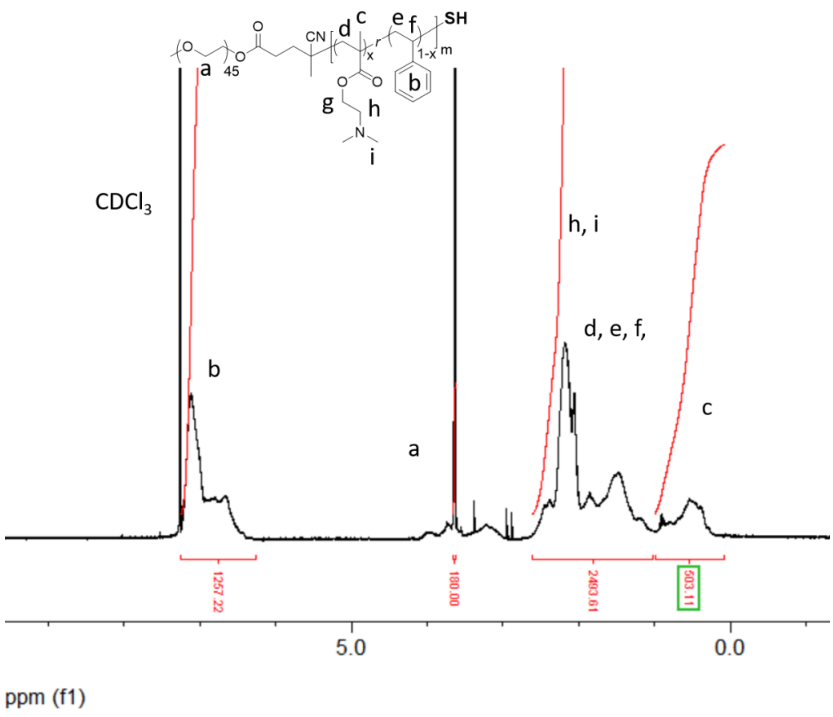

Figure 2.S2 1H NMR spectrum of PEO_{45}-*b*-P($DMAEMA_{0.40}$-*r*-$St_{0.60}$)$_{419}$-SH.

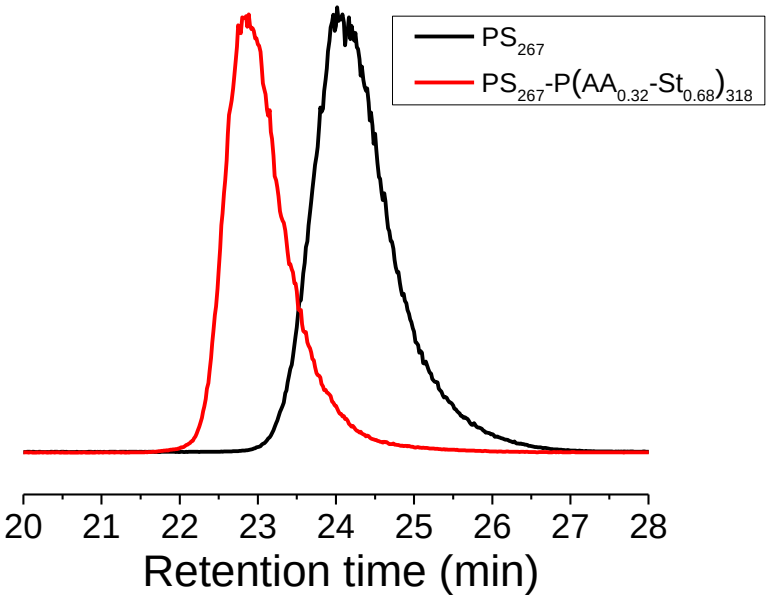

Figure 2.S3 GPC curve of PS_{267} and PS_{267}-*b*-P($AA_{0.32}$-*r*-$St_{0.68}$)$_{318}$. THF was used as an elution solvent, with PS as standards.

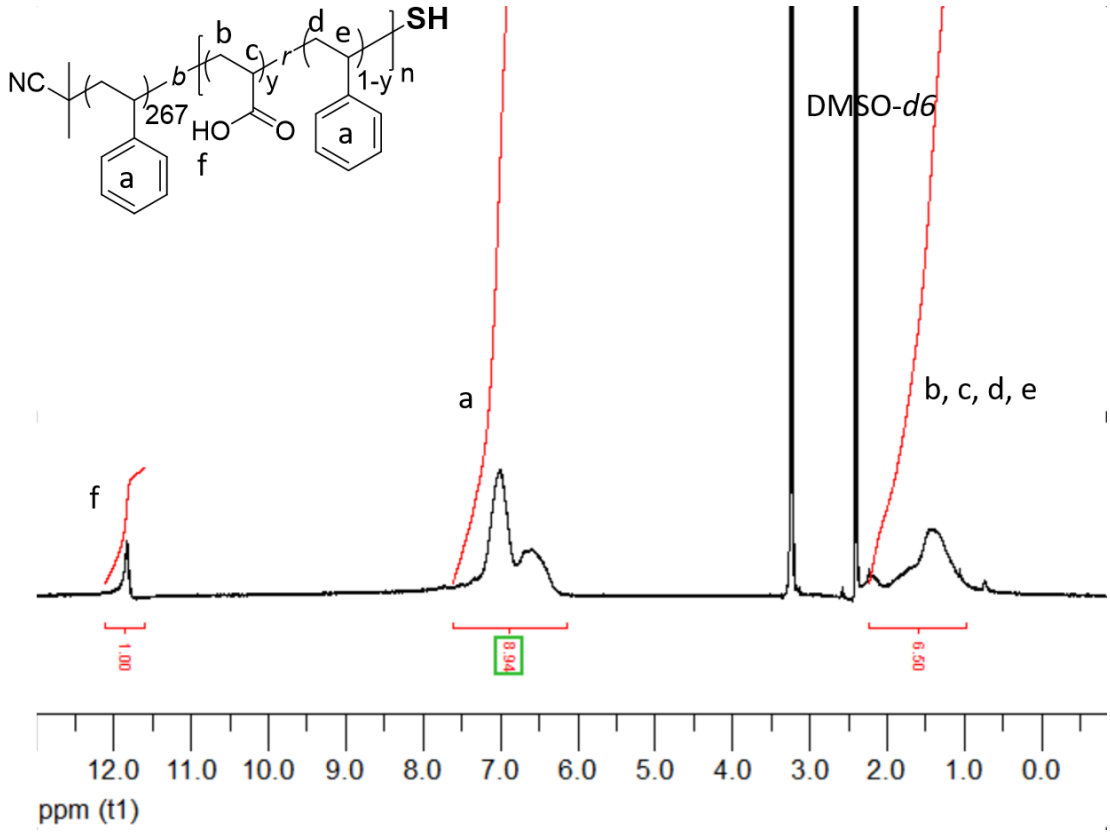

Figure 2.S4 ^{1}H NMR spectrum of the PS_{267}-*b*-P(AA_{y}-*r*-St_{1-y})$_{n}$-SH in DMSO-*d*6. The relationship of parameters y and n were determined by comparing the integrals of the resonance peaks of aromatic ring of PS block (6.4-7.3 ppm) with the integrals of resonance peaks of hydrogen from backbone (1.0-2.0 ppm) and that of hydrogen from carboxyl group (12 ppm). The actual length of negative polymer was determined to be PS_{267}-*b*-P($AA_{0.32}$-*r*-$St_{0.68}$)$_{318}$-SH together with the GPC data.

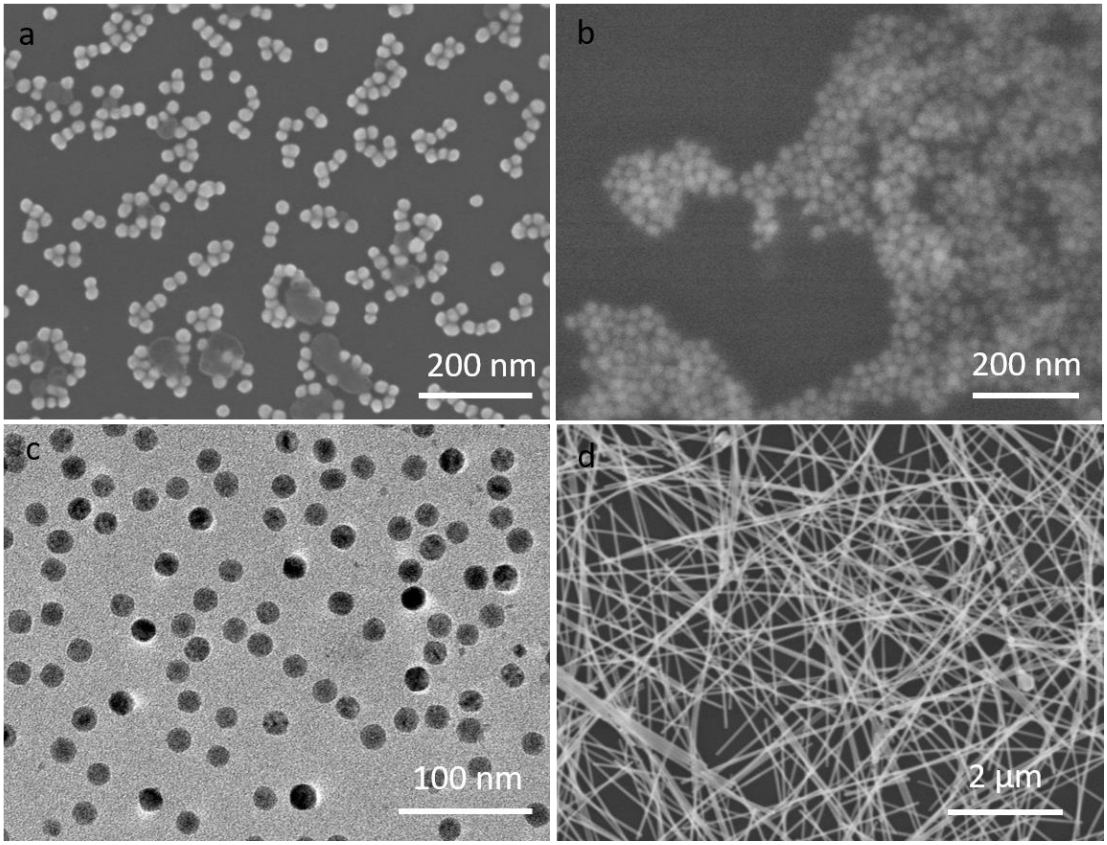

Figure 2.S5 SEM of Au NPs (a), Ag NPs (b), Fe_3O_4 NPs(c), and Ag NW (d).

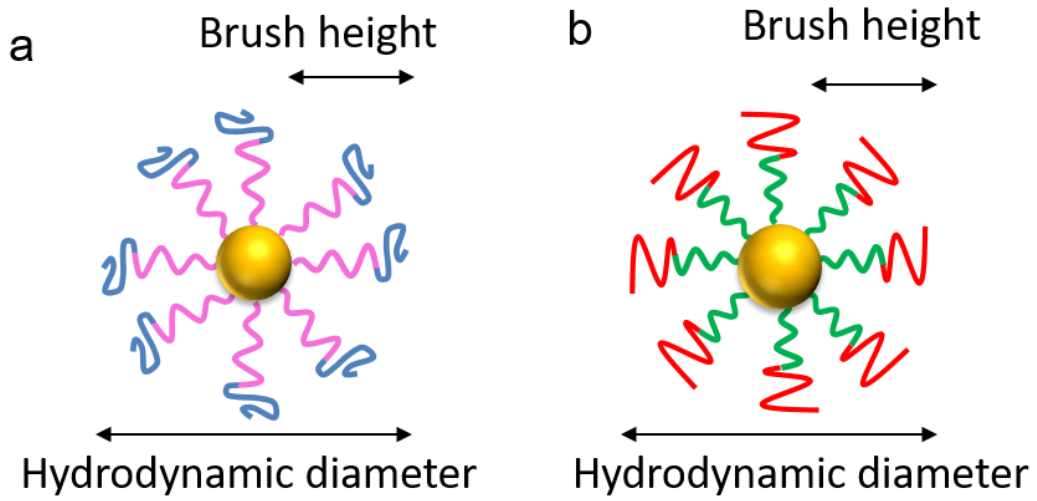

Figure 2.S6 Schematic illustration of Au NPs tethered with BCP brushes in good solvents: (a) $\mathbf{A_{20}}$: 20 nm Au NPs tethered with PEO_{45}-*b*-P($DMAEMA_{0.40}$-*r*-$St_{0.60}$)$_{419}$-SH. (b) $\mathbf{B_{24}}$: 24 nm Au NPs tethered with PS_{267}-*b*-P($AA_{0.32}$-*r*-$St_{0.68}$)$_{318}$.

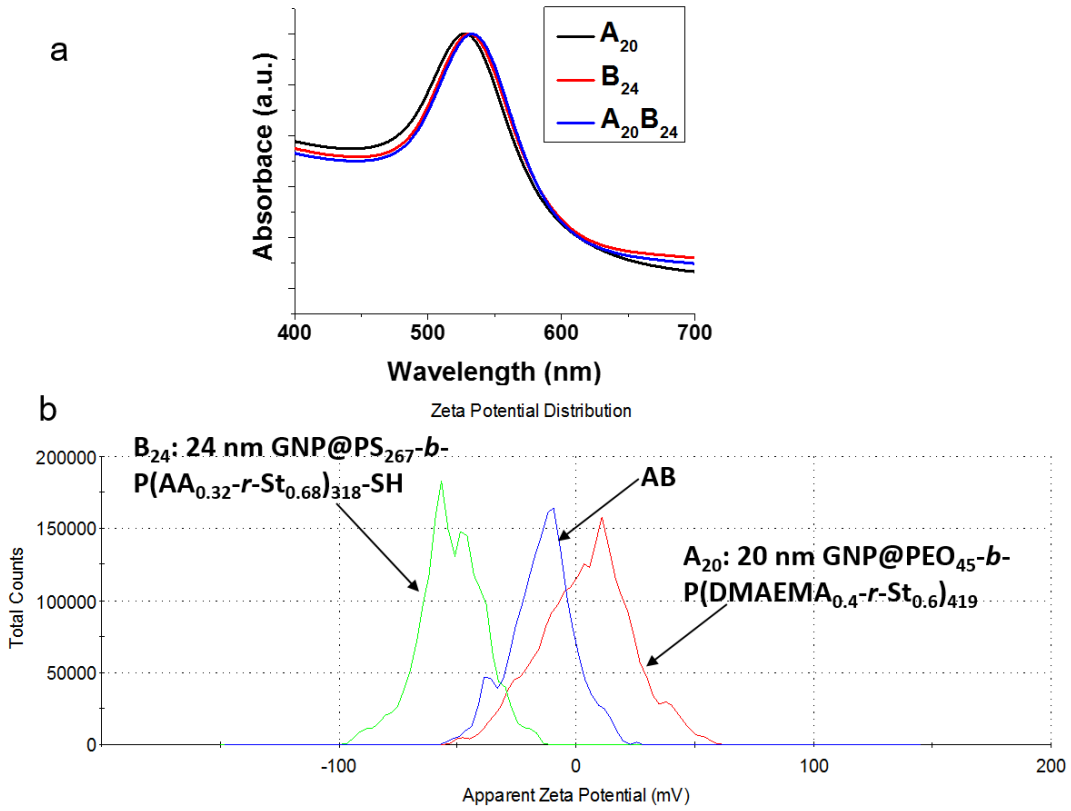

Figure 2.S7 UV-vis spectrum (a) and zeta potential (b) of dimer **AB** and individual building block **A** and **B** in THF.

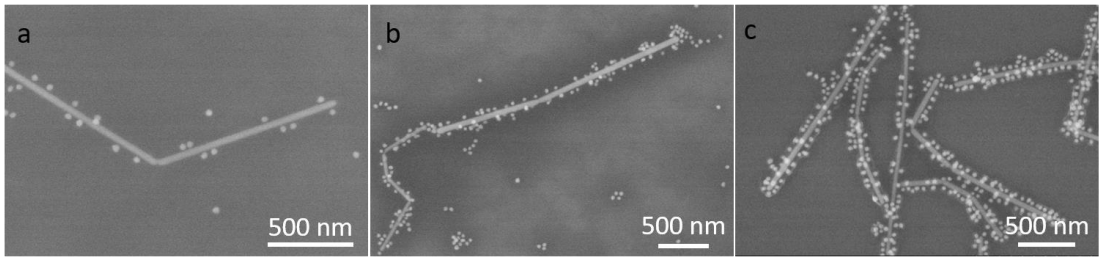

Figure 2.S8 SEM images of co-assembly of Au NP and Ag NW. The ratio of Au NPs/Ag NWs increase from a to c.

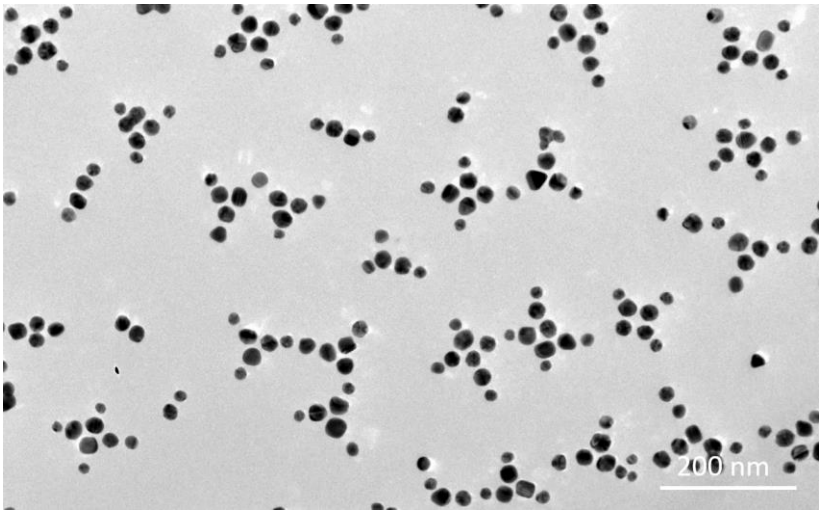

Figure 3.S1 TEM images of $\mathbf{(AB)_N}$ formed by $\mathbf{A_{20}B_{24}}$ in large area.

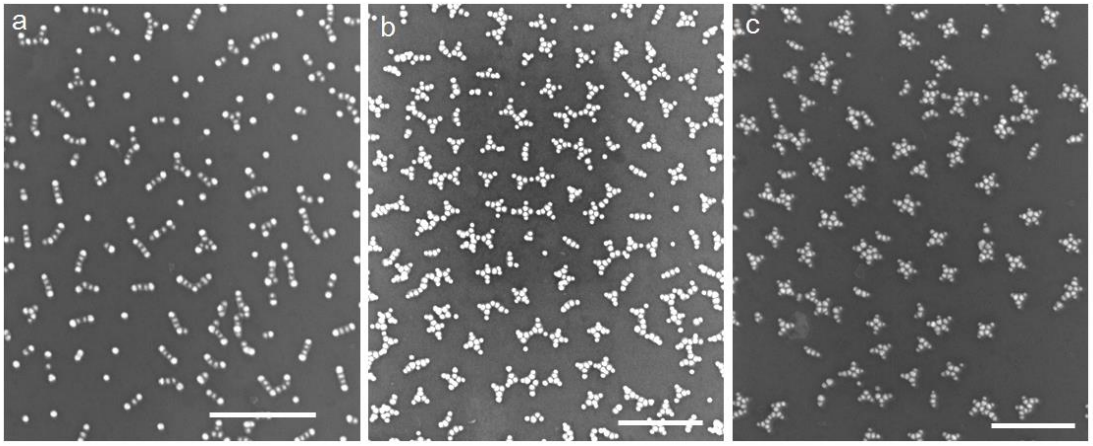

Figure 3.S2 (a-c) Large area SEM images of $\mathbf{(AB)_N}$ formed by $\mathbf{A_{25}B_{18}}$ (a), $\mathbf{A_{20}B_{24}}$ (b), and $\mathbf{A_{20}B_{30}}$ (c) in large area. Scale bar: 500 nm.

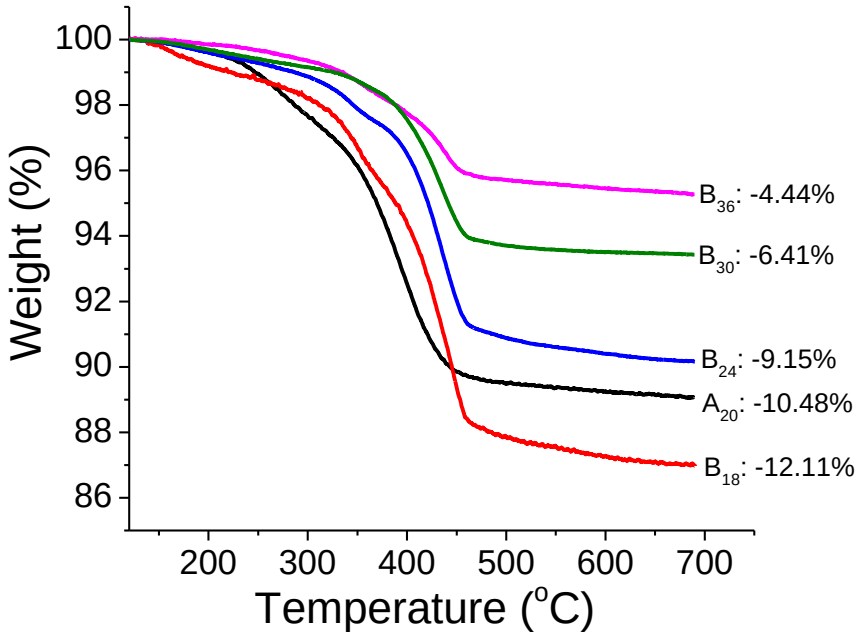

Figure 3.S3 TGA curves of the building block **A** and **B** with different size. The weight loss observed at elevated temperatures above 200 ℃ for **A** and 250 ℃ for **B** is originated from the thermal degradation of BCPs into volatile products.

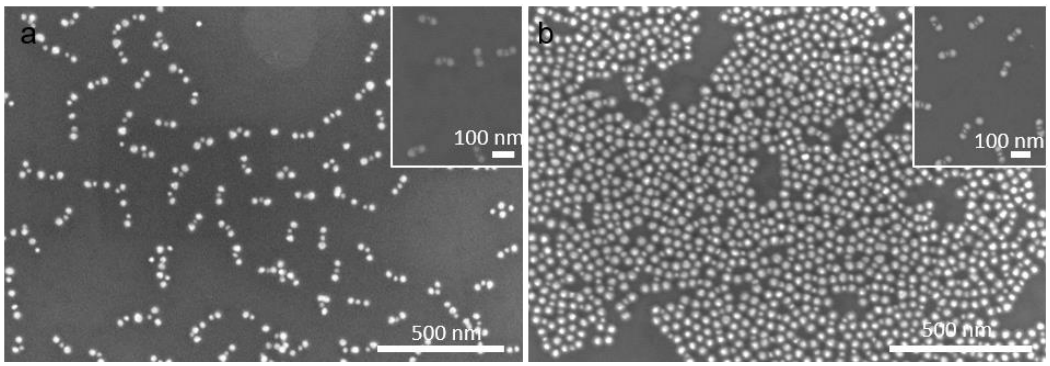

Figure 3.S4 Interfacial assembly of hydrophilic and hydrophobic **BAB**. (a) SEM image of individually dispersed **BAB** after interfacial assembly of hydrophilic **BAB**, the BCPs used for **A** and **B** are P3 and PEO_{45}-*b*-P($AA_{0.3}$-*r*-$St_{0.7}$)$_{328}$-SH. Inset: SEM image of hydrophilic **BAB**. (b) SEM image of disordered aggregation after interfacial

assembly of hydrophobic **BAB**, the BCPs used for **A** and **B** are PS_{173}-*b*-$P(DMAEMA_{0.3}$-*r*-$St_{0.7})_{300}$-SH and N4. Inset: SEM image of hydrophobic **BAB**.

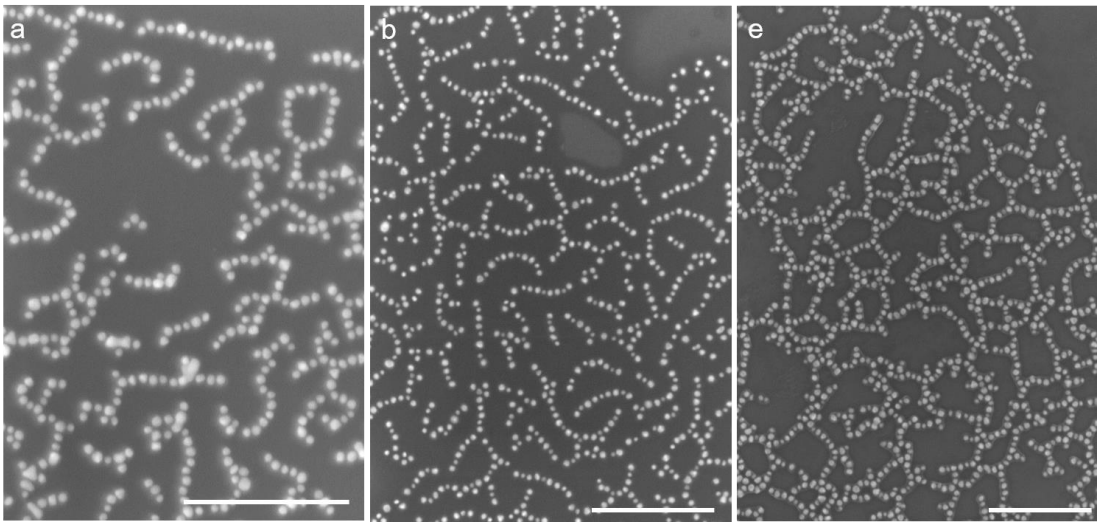

Figure 3.S5 Large area SEM images of chain structure $\mathbf{(BAB)_N}$ formed by $\mathbf{B_{24}A_{36}B_{24}}$ (a), $\mathbf{B_{24}A_{20}B_{24}}$ (b) and $\mathbf{B_{30}A_{20}B_{30}}$ (c) respectively. Scale bar: 500 nm.

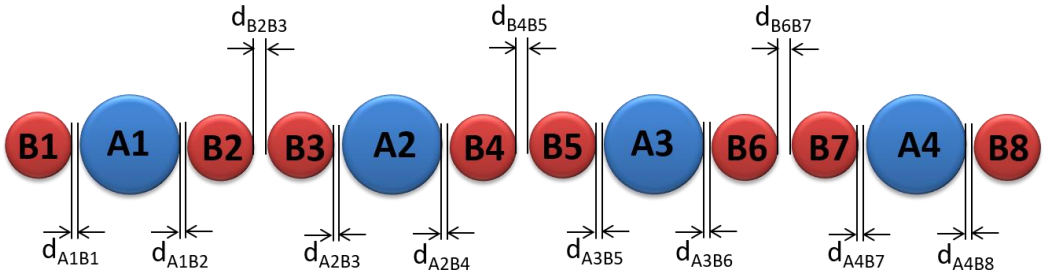

$$d_{AB}=(d_{A1B1}+d_{A1B2}+d_{A2B3}+d_{A2B4}+d_{A3B5}+d_{A3B6}+d_{A4B7}+d_{A4B8})/8$$
$$d_{BB}=(d_{B2B3}+d_{B4B5}+d_{B6B7})/3$$

Figure 3.S6 Scheme of interparticle distance of $\mathbf{(BAB)_N}$ and calculation of d_{AB} and d_{BB}.

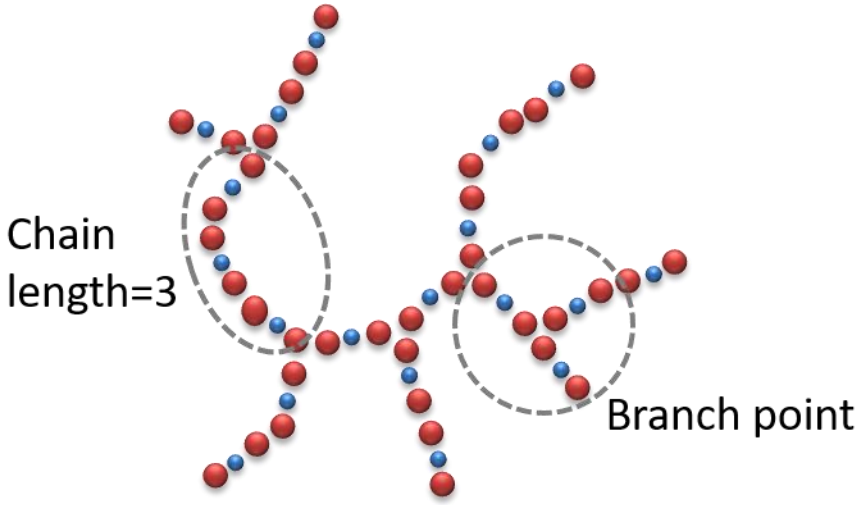

Figure 3.S7 Scheme of chain length and branch point of chain structure formed from trimers **BAB**.

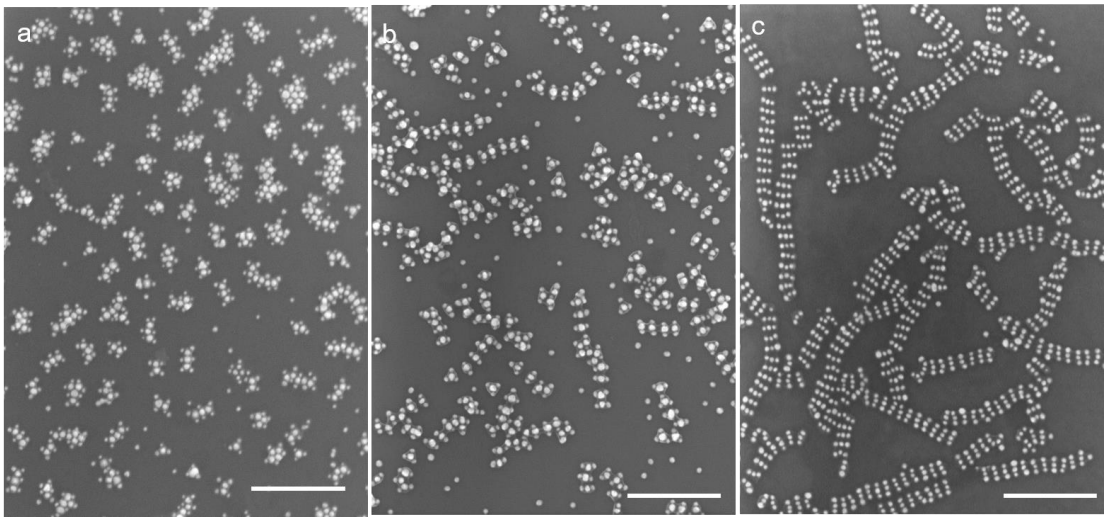

Figure 3.S8 Large area SEM images of **$(ABA)_N$** formed by **$A_{20}B_{36}A_{20}$** (a), **$A_{20}B_{30}A_{20}$** (b), and **$A_{20}B_{24}A_{20}$** (c), respectively. Scale bar: 500 nm.

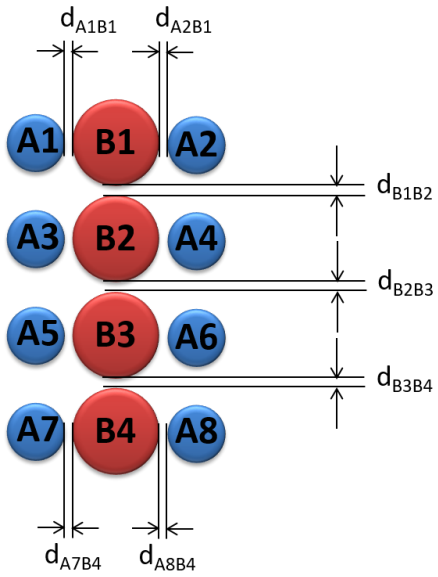

$$d_{AB}=(d_{A1B1}+d_{A2B1}+d_{A3B2}+d_{A4B2}+d_{A5B3}+d_{A6B3}+d_{A7B4}+d_{A8B4})/8$$

$$d_{BB}=(d_{B1B2}+d_{B2B3}+d_{B3B4})/3$$

Figure 3.S9 Scheme of interparticle distance of $\mathbf{(ABA)_N}$ and calculation of d_{AB} and d_{BB}.

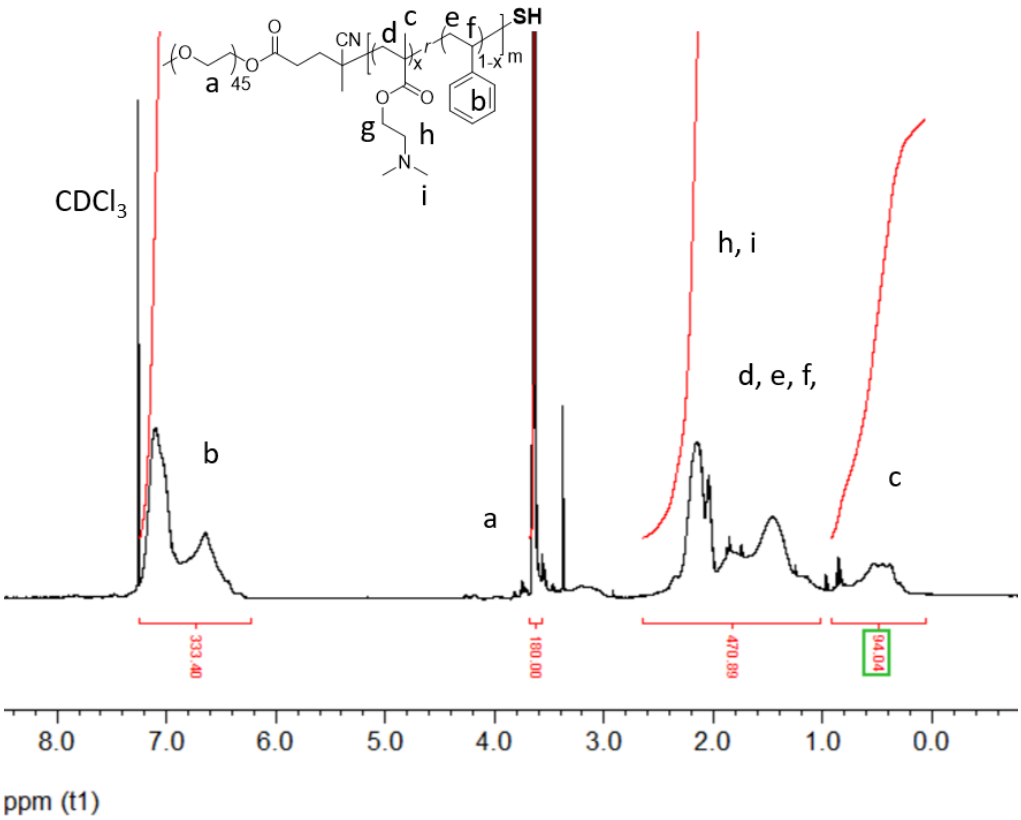

Figure 4.S1 ^{1}H NMR spectrum of PEO_{45}-*b*-$P(DMAEMA_{0.32}$-*r*-$St_{0.68})_{98}$-SH.

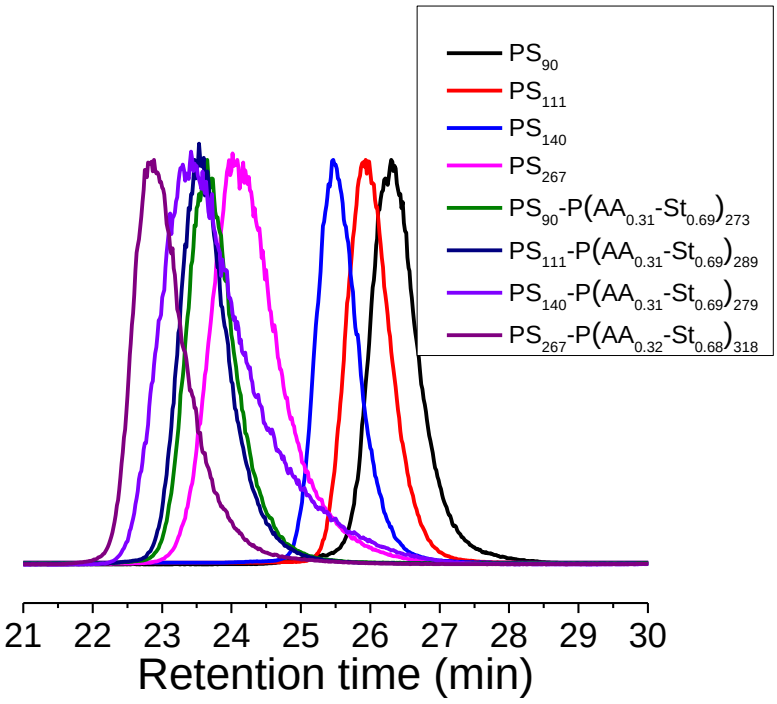

Figure 4.S2 GPC curve of PS-CTA and PS-*b*-P(AA-*r*-St)-SH with different lengths. THF was used as an elution solvent with PS as standards.

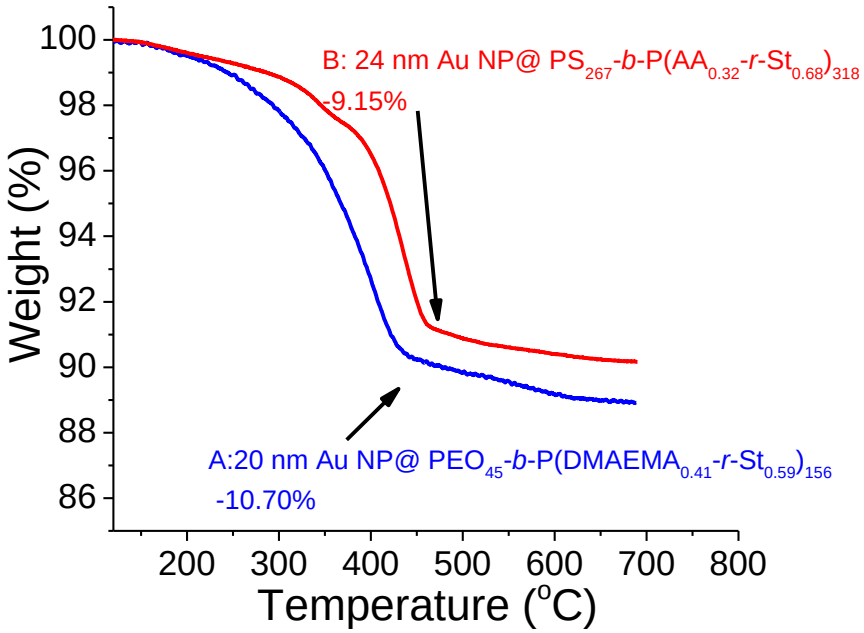

Figure 4.S3 TGA curves of hybrid building block **A(22)** and **B(267)**.

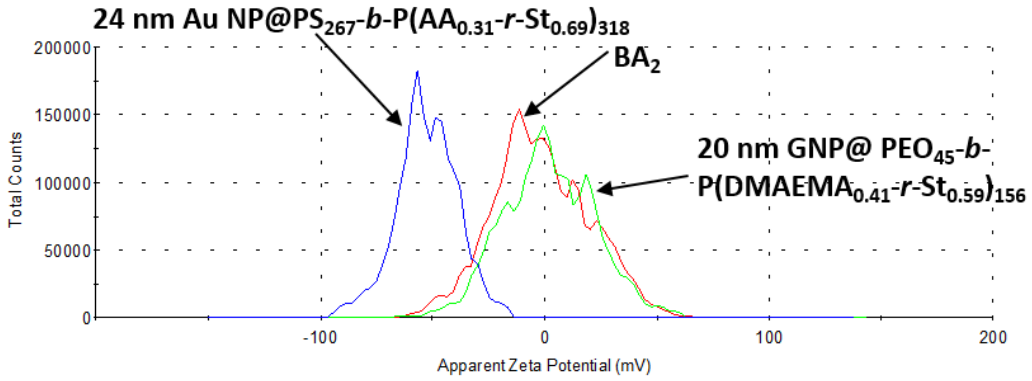

Figure 4.S4 Zeta potential of hybrid building block **A(22)**, **B(267)** and the trimers **A(22)B(267)A(22)**.

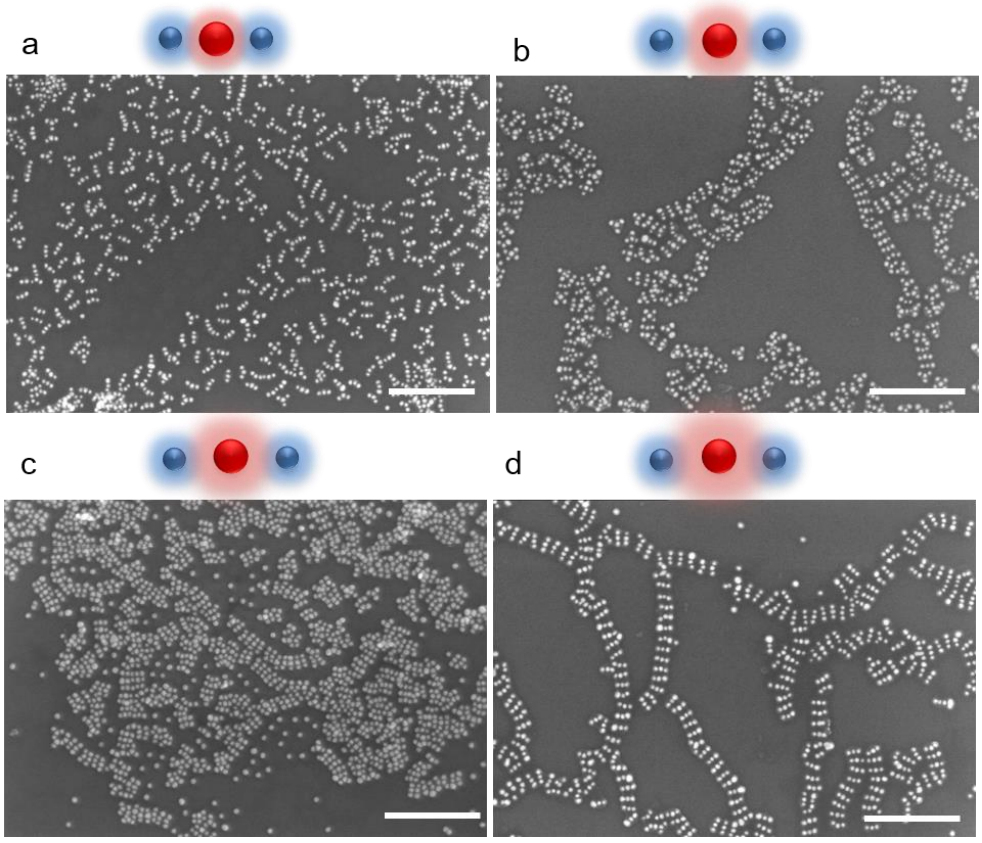

Figure 4.S5 (a-d) Large area SEM images of interfacial assembly of **ABA** formed by **A(22)** and **B(90)**, **B(111)**, **B(140)**, **B(267)**, respectively. Scale bar: 500 nm.

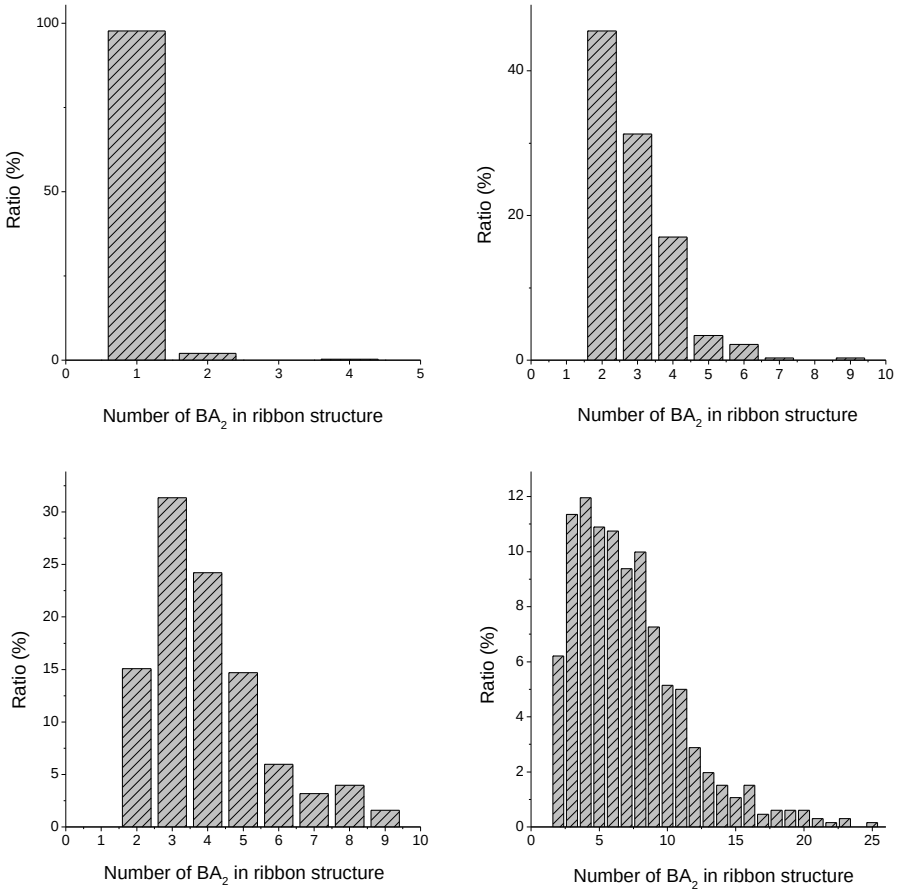

Figure 4.S6 Ribbon length distribution for interfacial assembly of **ABA** formed by **A(22)** and **B(90)**, **B(111)**, **B(140)**, **B(267)**, respectively.

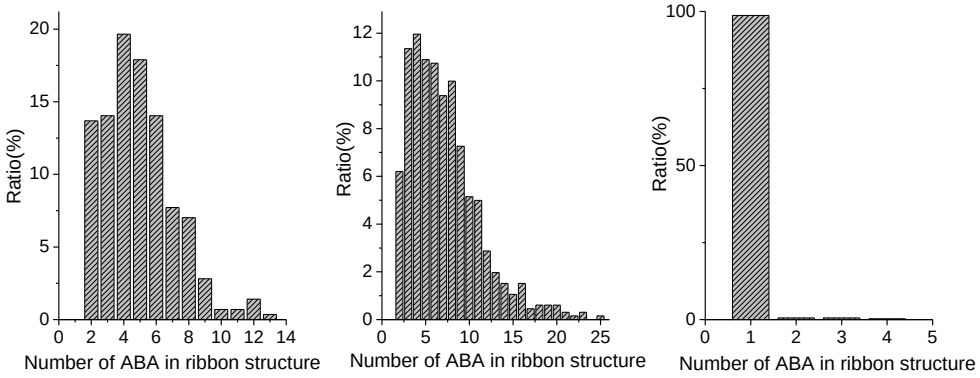

Figure 4.S7 Ribbon length distribution for interfacial assembly of **ABA** formed by **A(14)**, **A(22)**, **A(55)** and **B(267)**, respectively.

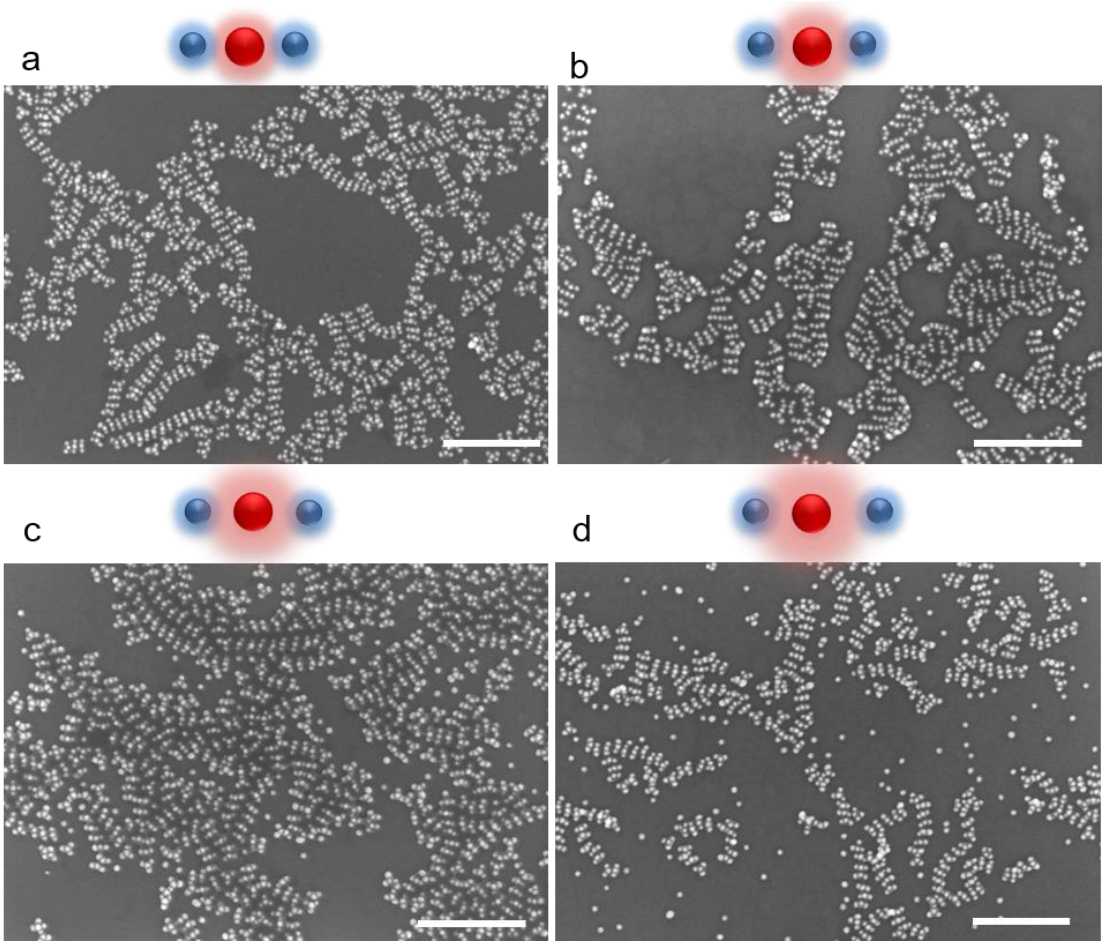

Figure 4.S8 (a-d) Large area SEM images of interfacial assembly of **ABA** formed by **A(14)** and **B(90)**, **B(111)**, **B(140)**, **B(267)**, respectively. Scale bar: 500 nm.

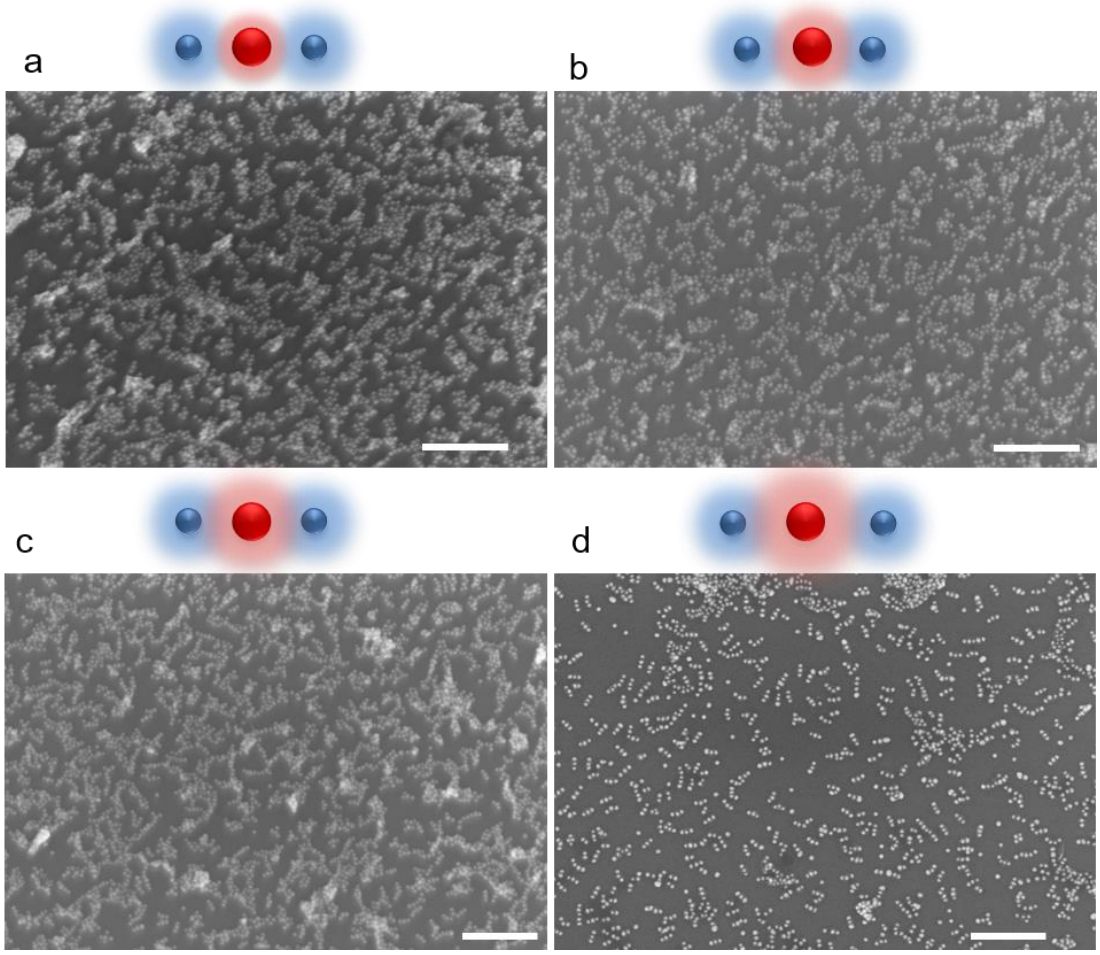

Figure 4.S9 (a-d) Large area SEM images of interfacial assembly of **ABA** formed by **A(55)** and **B(90)**, **B(111)**, **B(140)**, **B(267)**, respectively. Scale bar: 500 nm.

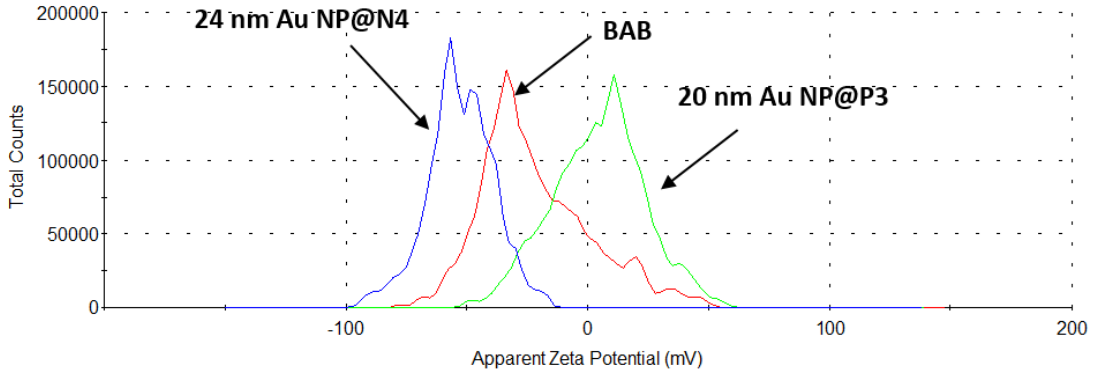

Figure 5.S1 Zeta potential of hybrid building block **A**: 20 nm Au NP tethered with P3

and **B**: 24 nm Au NP tethered with N4 and the trimers **BAB** formed by self-assembly of **A** and **B**.

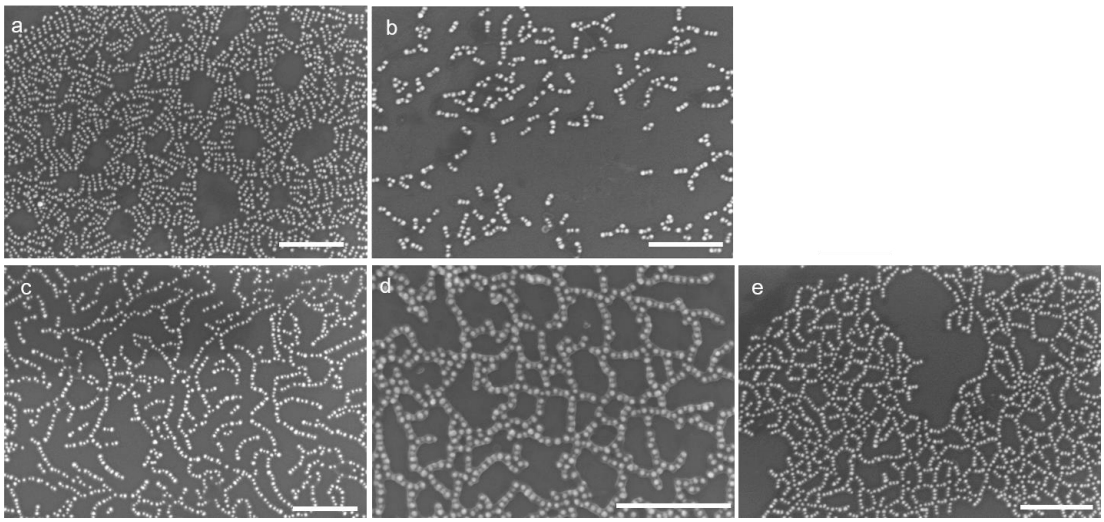

Figure 5.S2 (a-e) Large area SEM images of interfacial assembly of **BAB** with concentration of acid or base in aqueous as $[OH^-]$=0.2M, $[H^+]$=0, $[H^+]$=0.2 M, $[H^+]$=0.3M from a to e, respectively. Scale bar: 500 nm.

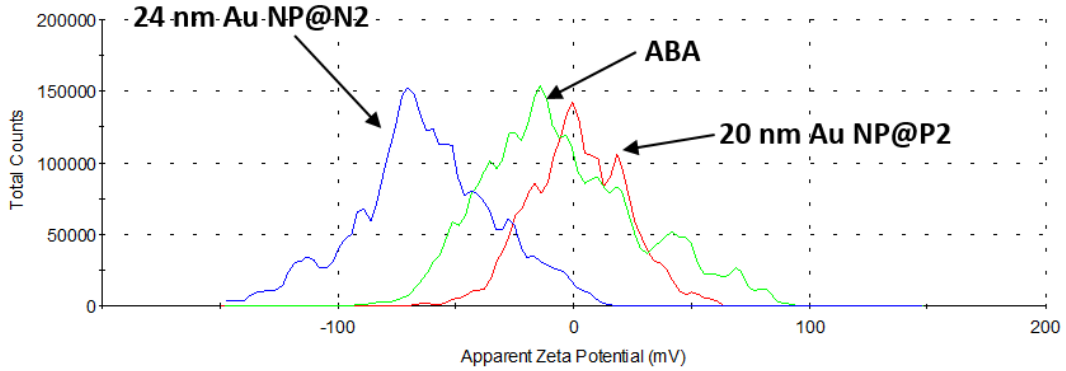

Figure 5.S3 Zeta potential of hybrid building block **A**: 20 nm Au NP tethered with P2 and **B**: 24 nm Au NP tethered with N2 and the trimers **ABA** formed by self-assembly of **A** and **B**.

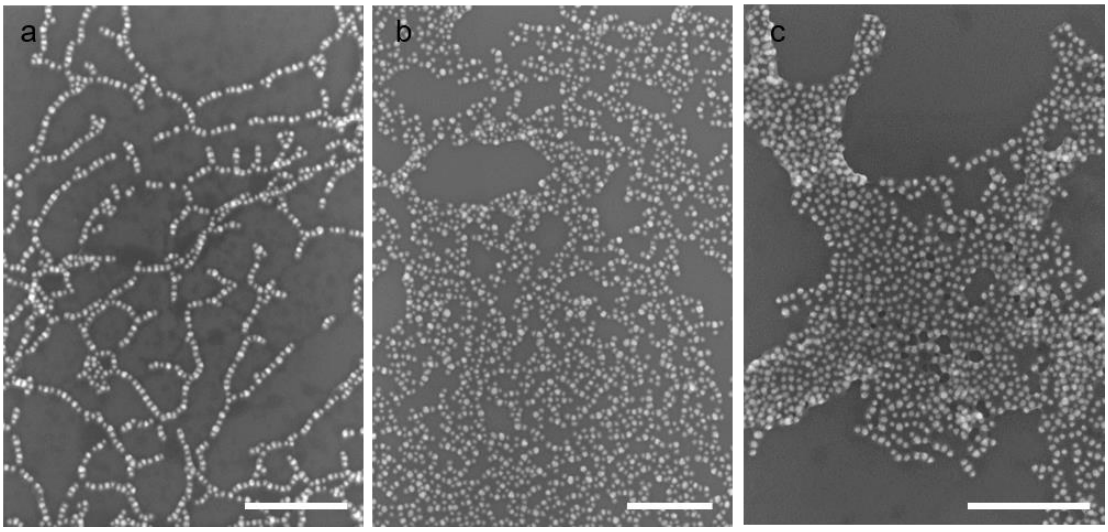

Figure 5.S4 (a-c) SEM images of interfacial assembly of **ABA** formed by **A**: 20 nm Au NP tethered with P2 and **B**: 24 nm Au NPs tethered with N1 (a), N3 (b), N4 (c), respectively. The concentration of base is $[OH^-]$=0.2M. Scale bar: 500 nm.

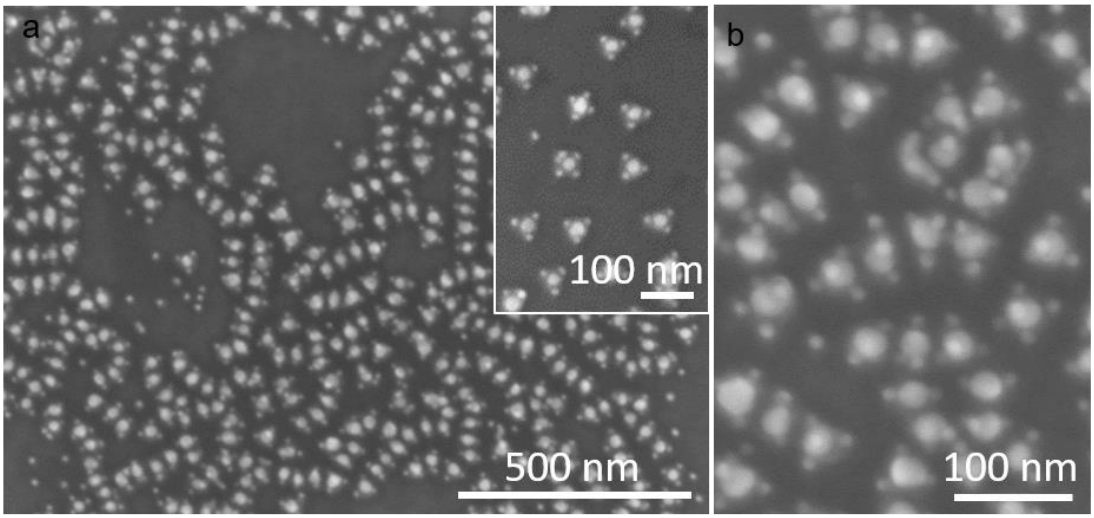

Figure 6.S1 Preliminary result of further assembly of amphiphilic tetramers $\mathbf{BA_3}$. (a, b) SEM images of stack of $\mathbf{BA_3}$ formed by interfacial assembly of $\mathbf{BA_3}$, in which A is 15 nm Au NPs tethered with PEO_{45}-*b*-$P(DMAEMA_{0.41}$-*r*-$St_{0.59})_{156}$ and **B**: 24 nm Au NPs tethered with PS_{267}-*b*-$P(AA_{0.31}$-*r*-$St_{0.69})_{318}$. The inset in figure a is the $\mathbf{BA_3}$ formed in first stage assembly. In figure b, the 3D stack of $\mathbf{BA_3}$ was observed.

Table 2.S1 The parameters of the building blocks in Figure chapter 2.

Figure #	Sample #	Supracolloids	building blocks	***BCP***
Figure 2.8	a	**AB_3**	**A_{20}**	P3
			B_{25}	N3
	b	**AB_4**	**A_{20}**	P3
			B_{25}	N2
	c	**BA_3**	**A_{20}**	P2
			B_{25}	N3
	d	**BA_4**	**A_{20}**	P1
			B_{25}	N3
Figure 2.10	a and b	**$(AB)_N$**	**A_{20}**	P4
			B_{24}	N3
Figure 2.11	a	**$(AB)_N$**	**A_{40}**	P4
			B_{25}	N3
Figure 2.S8	a-c	**Au_xAg**	**Ag NW**	P3
			Au_{35}	N1

Table 3.S1 The parameters of BCPs for the building blocks in Chapter 3.

supracolloids	Figure	Sample No.	building blocks	***BCP***
AB	Figure 3.8	a	A_{25}	P3
			B_{18}	N4
		b	A_{20}	P3
			B_{24}	N4
		c	A_{20}	P3
			B_{30}	N4
AB_2	Figure 3.12	d	A_{36}	P3
			B_{24}	N4
		e	A_{20}	P3
			B_{24}	N4
		f	A_{20}	P3
			B_{30}	N4
BA_2	Figure 3.14	g	A_{20}	P3
			B_{36}	N4
		h	A_{20}	P2
			B_{30}	N4
		i	A_{20}	P2
			B_{24}	N4

Table 3.S2 Interparticle distance of **$(AB)_N$** with different petal number and different size of Au NPs.

$(AB)_N$					
$(AB)_2$	d_{AB}	d_{BB}	$(AB)_3$	d_{AB}	d_{BB}
$A_{25}B_{18}$	9.94±2.42 nm	10.95±2.44 nm	$A_{25}B_{18}$	10.78±2.82 nm	12.04±2.36 nm
$A_{20}B_{24}$	8.59±1.67 nm	7.66±0.97 nm	$A_{20}B_{24}$	8.13±2.37 nm	7.43±2.01 nm
$A_{20}B_{30}$	7.44±1.45 nm	6.62±1.27 nm	$A_{20}B_{30}$	7.35±2.09 nm	6.44±1.37 nm
$(AB)_4$	d_{AB}	d_{BB}	$(AB)_5$	d_{AB}	d_{BB}
$A_{25}B_{18}$	11.26±3 nm	12.67±2.69 nm	$A_{25}B_{18}$	11.72±3.12 nm	13.74±2.74 nm
$A_{20}B_{24}$	7.91±2.06 nm	7.19±1.53 nm	$A_{20}B_{24}$	7.83±1.93 nm	7.2±1.99 nm
$A_{20}B_{30}$	7.23±1.48 nm	6.32±1.45 nm	$A_{20}B_{30}$	7.15±1.67 nm	6.38±1.57 nm
$(AB)_6$	d_{AB}	d_{BB}			
$A_{25}B_{18}$	11.96±3.28 nm	14.18±2.84 nm			
$A_{20}B_{24}$	7.13±1.52 nm	6.61±1.38 nm			
$A_{20}B_{30}$	6.49±1.61 nm	5.91±1.29 nm			

List of my publications

1. Jianwei Liu, Shaoyi Zhang, Hao Qi, Wucheng Wen, Shuhong Yu*, A General Strategy for Macroscopic-Scale Self-Assembly of Nanosized Building Blocks on Liquid-Liquid Interface , *Small*, **2012**,*8(15)*, 2412-2420.

2. Shaoyi Zhang, Jianwei Liu, Chuanling Zhang, Shuhong Yu*, Co-Assembled Thin Films of Ag Nanowires and Functional Nanoparticles at Liquid-Liquid Interface by Shaking, *Nanoscale*, **2013**, *5*, 4223-4229.

3. Chenglin Yi, Shaoyi Zhang, Kyle Thomas Webb, Zhihong Nie*, Anisotropic self-assembly of hairy inorganic nanoparticles, *Accounts of Chemical Research*, **2017**, *50 (1)*, 12–21.

4. Shaoyi Zhang, Yang Yang, Zhihong Nie*, Controllable Self-assembly of One-dimensional Nanocrystals, book chapter from: Functional Organic and Hybrid Nanostructured Materials: Fabrication, Properties and Applications; In book: *Functional Organic and Hybrid Nanostructured Materials: Fabrication, Properties, and Applications*, **2018**, DOI: 10.1002/9783527807369.ch1 pp.1-38.

5. Shaoyi Zhang, Jie He, Chelsey Lamar, Wan Kyu Oh, Zhihong Nie*, Self-assembly of polymer/inorganic nanoparticle hybrids with biomedical applications, 2018, to be submitted.

6. Chenglin Yi, Shaoyi Zhang, Jie He, Yijing Liu, Zhiqi Huang, Hongyu Guo, Kuikun Yang, Zhongyuan Lv and Zhihong Nie*, Building Nanoscale Supracolloids with Valence and Patches via Nanoparticle Reaction, 2018, to be submitted.

7. Shaoyi Zhang, Chenglin Yi, Yang Yang, Zhihong Nie*, Hierarchical assembly of amphiphilic supracolloids with tunable domains, 2018, to be submitted.

8. Shaoyi Zhang, Chenglin Yi, Xizheng Wang, Zhihong Nie*, Colloidal ribbons from anisotropic supracolloidal trimers with tunable amphiphilic surface, 2018, to be submitted.

9. Shaoyi Zhang, Chenglin Yi, Yang Yang, Zhihong Nie*, pH-responsive hierarchical self-assembly of amphiphilic trimers, 2017, to be submitted.

Reference.

1. (a) Whitesides, G. M.; Grzybowski, B., Self-assembly at all scales. *Science* **2002,** *295* (5564), 2418-2421; (b) Li, F.; Josephson, D. P.; Stein, A., Colloidal Assembly: The Road from Particles to Colloidal Molecules and Crystals. *Angew Chem Int Edit* **2011,** *50* (2), 360-388.
2. Halas, N. J.; Lal, S.; Chang, W. S.; Link, S.; Nordlander, P., Plasmons in Strongly Coupled Metallic Nanostructures. *Chem Rev* **2011,** *111* (6), 3913-3961.
3. (a) Tao, A. R.; Habas, S.; Yang, P., Shape control of colloidal metal nanocrystals. *Small* **2008,** *4* (3), 310-325; (b) Murray, C. B.; Kagan, C.; Bawendi, M., Synthesis and characterization of monodisperse nanocrystals and close-packed nanocrystal assemblies. *Annual Review of Materials Science* **2000,** *30* (1), 545-610.
4. Nie, Z.; Kumacheva, E., Patterning surfaces with functional polymers. *Nature materials* **2008,** *7* (4), 277-290.
5. Jones, M. R.; Osberg, K. D.; Macfarlane, R. J.; Langille, M. R.; Mirkin, C. A., Templated Techniques for the Synthesis and Assembly of Plasmonic Nanostructures. *Chem Rev* **2011,** *111* (6), 3736-3827.
6. Geissler, M.; Xia, Y., Patterning: Principles and some new developments. *Adv Mater* **2004,** *16* (15), 1249-1269.
7. vanBlaaderen, A.; Ruel, R.; Wiltzius, P., Template-directed colloidal crystallization. *Nature* **1997,** *385* (6614), 321-324.
8. Yin, Y.; Lu, Y.; Gates, B.; Xia, Y., Template-assisted self-assembly: a practical route to complex aggregates of monodispersed colloids with well-defined sizes, shapes, and structures. *J Am Chem Soc* **2001,** *123* (36), 8718-8729.
9. Kuemin, C.; Nowack, L.; Bozano, L.; Spencer, N. D.; Wolf, H., Oriented Assembly of Gold Nanorods on the Single-Particle Level. *Adv Funct Mater* **2012,** *22* (4), 702-708.
10. Flauraud, V.; Mastrangeli, M.; Bernasconi, G. D.; Butet, J.; Alexander, D. T. L.; Shahrabi, E.; Martin, O. J. F.; Brugger, J., Nanoscale topographical control of capillary assembly of nanoparticles. *Nature Nanotechnology* **2017,** *12* (1), 73-80.
11. Hamon, C.; Postic, M.; Mazari, E.; Bizien, T.; Dupuis, C.; Even-Hernandez, P.; Jimenez, A.; Courbin, L.; Gosse, C.; Artzner, F.; Marchi-Artzner, V., Three-Dimensional Self-Assembling of Gold Nanorods with Controlled Macroscopic Shape and Local Smectic B Order. *Acs Nano* **2012,** *6* (5), 4137-4146.
12. Ahmed, S.; Ryan, K. M., Self-assembly of vertically aligned nanorod supercrystals using highly oriented pyrolytic graphite. *Nano Lett* **2007,** *7* (8), 2480-2485.
13. Lahav, M.; Sehayek, T.; Vaskevich, A.; Rubinstein, I., Nanoparticle nanotubes. *Angew Chem Int Edit* **2003,** *42* (45), 5575-5579.
14. (a) Liu, Q.; Senyuk, B.; Tang, J.; Lee, T.; Qian, J.; He, S.; Smalyukh, I. I., Plasmonic complex fluids of nematiclike and helicoidal self-assemblies of gold nanorods with a negative order parameter. *Physical review letters* **2012,** *109* (8), 088301; (b) Liu, Q.; Campbell, M. G.; Evans, J. S.; Smalyukh, I. I., Orientationally Ordered Colloidal Co‐Dispersions of Gold Nanorods and Cellulose Nanocrystals. *Adv Mater* **2014,** *26* (42), 7178-7184.

15. Liu, Q. K.; Cui, Y. X.; Gardner, D.; Li, X.; He, S. L.; Smalyukh, I. I., Self-Alignment of Plasmonic Gold Nanorods in Reconfigurable Anisotropic Fluids for Tunable Bulk Metamaterial Applications. *Nano Lett* **2010,** *10* (4), 1347-1353.
16. Wang, L.; Li, Q., Stimuli‐Directing Self‐Organized 3D Liquid‐Crystalline Nanostructures: From Materials Design to Photonic Applications. *Adv Funct Mater* **2016,** *26* (1), 10-28.
17. Gharbi, M. A.; Manet, S.; Lhermitte, J.; Brown, S.; Milette, J.; Toader, V.; Sutton, M.; Reven, L., Reversible Nanoparticle Cubic Lattices in Blue Phase Liquid Crystals. *Acs Nano* **2016,** *10* (3), 3410-3415.
18. Fullam, S.; Cottell, D.; Rensmo, H.; Fitzmaurice, D., Carbon nanotube templated self-assembly and thermal processing of gold nanowires. *Adv Mater* **2000,** *12* (19), 1430-1432.
19. Correa-Duarte, M. A.; Perez-Juste, J.; Sanchez-Iglesias, A.; Giersig, M.; Liz-Marzan, L. M., Aligning an nanorods by using carbon nanotubes as templates. *Angew Chem Int Edit* **2005,** *44* (28), 4375-4378.
20. Merg, A. D.; Boatz, J. C.; Mandal, A.; Zhao, G.; Mokashi-Punekar, S.; Liu, C.; Wang, X.; Zhang, P.; van der Wel, P. C.; Rosi, N. L., Peptide-Directed Assembly of Single-Helical Gold Nanoparticle Superstructures Exhibiting Intense Chiroptical Activity. *J Am Chem Soc* **2016,** *138* (41), 13655-13663.
21. Hore, M. J.; Composto, R. J., Functional polymer nanocomposites enhanced by nanorods. *Macromolecules* **2013,** *47* (3), 875-887.
22. (a) Ferrier Jr, R. C.; Koski, J.; Riggleman, R. A.; Composto, R. J., Engineering the Assembly of Gold Nanorods in Polymer Matrices. *Macromolecules* **2016,** *49* (3), 1002-1015; (b) Hore, M. J.; Composto, R. J., Nanorod self-assembly for tuning optical absorption. *Acs Nano* **2010,** *4* (11), 6941-6949.
23. Deshmukh, R. D.; Liu, Y.; Composto, R. J., Two-dimensional confinement of nanorods in block copolymer domains. *Nano Lett* **2007,** *7* (12), 3662-3668.
24. Chan, Y. N. C.; Schrock, R. R.; Cohen, R. E., Synthesis of Single Silver Nanoclusters within Spherical Microdomains in Block Copolymer Films. *J Am Chem Soc* **1992,** *114* (18), 7295-7296.
25. Bockstaller, M. R.; Lapetnikov, Y.; Margel, S.; Thomas, E. L., Size-selective organization of enthalpic compatibilized nanocrystals in ternary block copolymer/particle mixtures. *Journal of the American Chemical Society* **2003,** *125* (18), 5276-5277.
26. Zhang, Q. L.; Gupta, S.; Emrick, T.; Russell, T. P., Surface-functionalized CdSe nanorods for assembly in diblock copolymer templates. *Journal of the American Chemical Society* **2006,** *128* (12), 3898-3899.
27. (a) Ploshnik, E.; Salant, A.; Banin, U.; Shenhar, R., Hierarchical Surface Patterns of Nanorods Obtained by Co-Assembly with Block Copolymers in Ultrathin Films. *Adv Mater* **2010,** *22* (25), 2774-+; (b) Liu, Z. C.; Huang, H. Y.; He, T. B., Large-Area 2D Gold Nanorod Arrays Assembled on Block Copolymer Templates. *Small* **2013,** *9* (4), 505-510; (c) Thorkelsson, K.; Nelson, J. H.; Alivisatos, A. P.; Xu, T., End-to-end alignment of nanorods in thin films. *Nano Lett* **2013,** *13* (10), 4908-13; (d) Nepal, D.; Onses, M. S.; Park, K.; Jespersen, M.; Thode, C. J.; Nealey, P. F.; Vaia, R. A., Control over Position, Orientation, and Spacing of Arrays of Gold

Nanorods Using Chemically Nanopatterned Surfaces and Tailored Particle-Particle-Surface Interactions. *Acs Nano* **2012,** *6* (6), 5693-5701.
28. Grzelczak, M.; Vermant, J.; Furst, E. M.; Liz-Marzán, L. M., Directed self-assembly of nanoparticles. *Acs Nano* **2010,** *4* (7), 3591-3605.
29. van der Zande, B. M.; Koper, G. J.; Lekkerkerker, H. N., Alignment of rod-shaped gold particles by electric fields. *The Journal of Physical Chemistry B* **1999,** *103* (28), 5754-5760.
30. Smith, P. A.; Nordquist, C. D.; Jackson, T. N.; Mayer, T. S.; Martin, B. R.; Mbindyo, J.; Mallouk, T. E., Electric-field assisted assembly and alignment of metallic nanowires. *Applied Physics Letters* **2000,** *77* (9), 1399.
31. Hermanson, K. D.; Lumsdon, S. O.; Williams, J. P.; Kaler, E. W.; Velev, O. D., Dielectrophoretic assembly of electrically functional microwires from nanoparticle suspensions. *Science* **2001,** *294* (5544), 1082-1086.
32. Lumsdon, S. O.; Kaler, E. W.; Velev, O. D., Two-dimensional crystallization of microspheres by a coplanar AC electric field. *Langmuir* **2004,** *20* (6), 2108-2116.
33. Bharti, B.; Findenegg, G. H.; Velev, O. D., Co-Assembly of Oppositely Charged Particles into Linear Clusters and Chains of Controllable Length. *Sci Rep-Uk* **2012,** *2*.
34. Hu, Z.; Fischbein, M. D.; Querner, C.; Drndic, M., Electric-field-driven accumulation and alignment of CdSe and CdTe nanorods in nanoscale devices. *Nano Lett* **2006,** *6* (11), 2585-2591.
35. Li, L.-s.; Alivisatos, A. P., Origin and scaling of the permanent dipole moment in CdSe nanorods. *Physical review letters* **2003,** *90* (9), 097402.
36. Ryan, K. M.; Mastroianni, A.; Stancil, K. A.; Liu, H.; Alivisatos, A., Electric-field-assisted assembly of perpendicularly oriented nanorod superlattices. *Nano Lett* **2006,** *6* (7), 1479-1482.
37. Wang, M.; He, L.; Yin, Y., Magnetic field guided colloidal assembly. *Materials Today* **2013,** *16* (4), 110-116.
38. Lalatonne, Y.; Richardi, J.; Pileni, M. P., Van der Waals versus dipolar forces controlling mesoscopic organizations of magnetic nanocrystals. *Nature Materials* **2004,** *3* (2), 121-125.
39. Ahniyaz, A.; Sakamoto, Y.; Bergstrom, L., Magnetic field-induced assembly of oriented superlattices from maghemite nanocubes. *P Natl Acad Sci USA* **2007,** *104* (45), 17570-17574.
40. Anagnostopoulou, E.; Grindi, B.; Lacroix, L.-M.; Ott, F.; Panagiotopoulos, I.; Viau, G., Dense arrays of cobalt nanorods as rare-earth free permanent magnets. *Nanoscale* **2016,** *8* (7), 4020-4029.
41. Ding, T.; Song, K.; Clays, K.; Tung, C. H., Fabrication of 3D Photonic Crystals of Ellipsoids: Convective Self‐Assembly in Magnetic Field. *Adv Mater* **2009,** *21* (19), 1936-1940.
42. Singh, G.; Chan, H.; Baskin, A.; Gelman, E.; Repnin, N.; Kral, P.; Klajn, R., Self-assembly of magnetite nanocubes into helical superstructures. *Science* **2014,** *345* (6201), 1149-1153.
43. Yan, J.; Chaudhary, K.; Bae, S. C.; Lewis, J. A.; Granick, S., Colloidal ribbons and rings from Janus magnetic rods. *Nature communications* **2013,** *4*, 1516.

44. (a) Chen, L. B.; Zukoski, C. F.; Ackerson, B. J.; Hanley, H. J. M.; Straty, G. C.; Barker, J.; Glinka, C. J., Structural-Changes and Orientational Order in a Sheared Colloidal Suspension. *Physical Review Letters* **1992,** *69* (4), 688-691; (b) Yan, Y. D.; Dhont, J. K. G.; Smits, C.; Lekkerkerker, H. N. W., Oscillatory-Shear-Induced Order in Nonaqueous Dispersions of Charged Colloidal Spheres. *Physica A* **1994,** *202* (1-2), 68-80.
45. Huang, Y.; Duan, X.; Wei, Q.; Lieber, C. M., Directed assembly of one-dimensional nanostructures into functional networks. *Science* **2001,** *291* (5504), 630-633.
46. (a) Kuhn, P.; Puigmartí-Luis, J.; Imaz, I.; Maspoch, D.; Dittrich, P. S., Controlling the length and location of in situ formed nanowires by means of microfluidic tools. *Lab on a Chip* **2011,** *11* (4), 753-757; (b) Zhou, H.; Heyer, P.; Kim, H.-J.; Song, J.-H.; Piao, L.; Kim, S.-H., Reversible macroscopic alignment of Ag nanowires. *Chemistry of Materials* **2011,** *23* (16), 3622-3627.
47. Wang, L.; Liu, Y.; He, J.; Hourwitz, M. J.; Yang, Y.; Fourkas, J. T.; Han, X.; Nie, Z., Continuous Microfluidic Self‐Assembly of Hybrid Janus‐Like Vesicular Motors: Autonomous Propulsion and Controlled Release. *Small* **2015,** *11* (31), 3762-3767.
48. (a) Pickering, S. U., CXCVI.—emulsions. *Journal of the Chemical Society, Transactions* **1907,** *91*, 2001-2021; (b) Ramsden, W., Separation of Solids in the Surface-Layers of Solutions and'Suspensions'(Observations on Surface-Membranes, Bubbles, Emulsions, and Mechanical Coagulation).--Preliminary Account. *Proceedings of the royal Society of London* **1903,** *72*, 156-164.
49. Pieranski, P., Two-dimensional interfacial colloidal crystals. *Physical review letters* **1980,** *45* (7), 569.
50. Lin, Y.; Skaff, H.; Emrick, T.; Dinsmore, A. D.; Russell, T. P., Nanoparticle assembly and transport at liquid-liquid interfaces. *Science* **2003,** *299* (5604), 226-229.
51. (a) Dong, L.; Johnson, D. T., Adsorption of acicular particles at liquid-fluid interfaces and the influence of the line tension. *Langmuir* **2005,** *21* (9), 3838-3849; (b) Basavaraj, M.; Fuller, G.; Fransaer, J.; Vermant, J., Packing, flipping, and buckling transitions in compressed monolayers of ellipsoidal latex particles. *Langmuir* **2006,** *22* (15), 6605-6612; (c) Lewandowski, E. P.; Searson, P. C.; Stebe, K. J., Orientation of a nanocylinder at a fluid interface. *The Journal of Physical Chemistry B* **2006,** *110* (9), 4283-4290.
52. Chen, M.; Pica, T.; Jiang, Y.-B.; Li, P.; Yano, K.; Liu, J. P.; Datye, A. K.; Fan, H., Synthesis and self-assembly of fcc phase FePt nanorods. *J Am Chem Soc* **2007,** *129* (20), 6348-6349.
53. (a) Carbone, L.; Nobile, C.; De Giorgi, M.; Sala, F. D.; Morello, G.; Pompa, P.; Hytch, M.; Snoeck, E.; Fiore, A.; Franchini, I. R., Synthesis and micrometer-scale assembly of colloidal CdSe/CdS nanorods prepared by a seeded growth approach. *Nano Lett* **2007,** *7* (10), 2942-2950; (b) Rizzo, A.; Nobile, C.; Mazzeo, M.; Giorgi, M. D.; Fiore, A.; Carbone, L.; Cingolani, R.; Manna, L.; Gigli, G., Polarized light emitting diode by long-range nanorod self-assembling on a water surface. *Acs Nano* **2009,** *3* (6), 1506-1512.
54. Sánchez-Iglesias, A.; Rivas-Murias, B.; Grzelczak, M.; Pérez-Juste, J.; Liz-Marzán, L. M.; Rivadulla, F.; Correa-Duarte, M. A., Highly transparent and

conductive films of densely aligned ultrathin Au nanowire monolayers. *Nano Lett* **2012,** *12* (12), 6066-6070.
55. Sánchez‐Iglesias, A.; Grzelczak, M.; Pérez‐Juste, J.; Liz‐Marzán, L. M., Binary Self‐Assembly of Gold Nanowires with Nanospheres and Nanorods. *Angewandte Chemie International Edition* **2010,** *49* (51), 9985-9989.
56. Khanal, B. P.; Zubarev, E. R., Rings of nanorods. *Angewandte Chemie International Edition* **2007,** *46* (13), 2195-2198.
57. (a) Tao, A. R.; Huang, J.; Yang, P., Langmuir−Blodgettry of nanocrystals and nanowires. *Accounts of chemical research* **2008,** *41* (12), 1662-1673; (b) Kim, F.; Kwan, S.; Akana, J.; Yang, P., Langmuir-Blodgett nanorod assembly. *J Am Chem Soc* **2001,** *123* (18), 4360-4361; (c) Acharya, S.; Panda, A. B.; Belman, N.; Efrima, S.; Golan, Y., A Semiconductor‐Nanowire Assembly of Ultrahigh Junction Density by the Langmuir‐Blodgett Technique. *Adv Mater* **2006,** *18* (2), 210-213; (d) Tao, A.; Kim, F.; Hess, C.; Goldberger, J.; He, R.; Sun, Y.; Xia, Y.; Yang, P., Langmuir-Blodgett silver nanowire monolayers for molecular sensing using surface-enhanced Raman spectroscopy. *Nano Lett* **2003,** *3* (9), 1229-1233.
58. (a) Whang, D.; Jin, S.; Wu, Y.; Lieber, C. M., Large-scale hierarchical organization of nanowire arrays for integrated nanosystems. *Nano Lett* **2003,** *3* (9), 1255-1259; (b) Liu, J.-W.; Zhu, J.-H.; Zhang, C.-L.; Liang, H.-W.; Yu, S.-H., Mesostructured assemblies of ultrathin superlong tellurium nanowires and their photoconductivity. *J Am Chem Soc* **2010,** *132* (26), 8945-8952.
59. (a) Yang, P.; Kim, F., Langmuir‐Blodgett Assembly of One‐Dimensional Nanostructures. *ChemPhysChem* **2002,** *3* (6), 503-506; (b) Böker, A.; He, J.; Emrick, T.; Russell, T. P., Self-assembly of nanoparticles at interfaces. *Soft Matter* **2007,** *3* (10), 1231-1248.
60. Singh, A.; Gunning, R. D.; Ahmed, S.; Barrett, C. A.; English, N. J.; Garate, J.-A.; Ryan, K. M., Controlled semiconductor nanorod assembly from solution: influence of concentration, charge and solvent nature. *Journal of Materials Chemistry* **2012,** *22* (4), 1562-1569.
61. Ming, T.; Kou, X.; Chen, H.; Wang, T.; Tam, H. L.; Cheah, K. W.; Chen, J. Y.; Wang, J., Ordered gold nanostructure assemblies formed by droplet evaporation. *Angewandte Chemie* **2008,** *120* (50), 9831-9836.
62. Ghezelbash, A.; Koo, B.; Korgel, B. A., Self-assembled stripe patterns of CdS nanorods. *Nano Lett* **2006,** *6* (8), 1832-1836.
63. Koster, L. J. A.; Khodabakhsh, S.; Greenham, N. C., Controlling the assembly of CdS nanorods via solvent and acidity. *Soft Matter* **2014,** *10* (34), 6485-6490.
64. (a) Zanella, M.; Gomes, R.; Povia, M.; Giannini, C.; Zhang, Y.; Riskin, A.; Van Bael, M.; Hens, Z.; Manna, L., Self‐Assembled Multilayers of Vertically Aligned Semiconductor Nanorods on Device‐Scale Areas. *Adv Mater* **2011,** *23* (19), 2205-2209; (b) Baker, J. L.; Widmer-Cooper, A.; Toney, M. F.; Geissler, P. L.; Alivisatos, A. P., Device-scale perpendicular alignment of colloidal nanorods. *Nano Lett* **2009,** *10* (1), 195-201.
65. (a) Novak, J. P.; Feldheim, D. L., Assembly of phenylacetylene-bridged silver and gold nanoparticle arrays. *J Am Chem Soc* **2000,** *122* (16), 3979-3980; (b) Shibu Joseph, S.; Ipe, B. I.; Pramod, P.; Thomas, K. G., Gold nanorods to nanochains: mechanistic investigations on their longitudinal assembly using α, ω-alkanedithiols

and interplasmon coupling. *The Journal of Physical Chemistry B* **2006,** *110* (1), 150-157; (c) Thomas, K. G.; Barazzouk, S.; Ipe, B. I.; Joseph, S. S.; Kamat, P. V., Uniaxial plasmon coupling through longitudinal self-assembly of gold nanorods. *The Journal of Physical Chemistry B* **2004,** *108* (35), 13066-13068; (d) Sudeep, P.; Joseph, S. S.; Thomas, K. G., Selective detection of cysteine and glutathione using gold nanorods. *J Am Chem Soc* **2005,** *127* (18), 6516-6517; (e) Sun, Z.; Ni, W.; Yang, Z.; Kou, X.; Li, L.; Wang, J., pH‐Controlled Reversible Assembly and Disassembly of Gold Nanorods. *Small* **2008,** *4* (9), 1287-1292; (f) Wessels, J. M.; Nothofer, H. G.; Ford, W. E.; von Wrochem, F.; Scholz, F.; Vossmeyer, T.; Schroedter, A.; Weller, H.; Yasuda, A., Optical and electrical properties of three-dimensional interlinked gold nanoparticle assemblies. *J Am Chem Soc* **2004,** *126* (10), 3349-3356; (g) Mayer, C. R.; Neveu, S.; Cabuil, V., 3D hybrid nanonetworks from gold-functionalized nanoparticles. *Adv Mater* **2002,** *14* (8), 595-597.

66. Wang, Y.; DePrince III, A. E.; K. Gray, S.; Lin, X.-M.; Pelton, M., Solvent-mediated end-to-end assembly of gold nanorods. *The Journal of Physical Chemistry Letters* **2010,** *1* (18), 2692-2698.

67. Chan, Y. T.; Li, S.; Moorefield, C. N.; Wang, P.; Shreiner, C. D.; Newkome, G. R., Self‐Assembly, Disassembly, and Reassembly of Gold Nanorods Mediated by Bis (terpyridine)‐Metal Connectivity. *Chemistry–A European Journal* **2010,** *16* (14), 4164-4168.

68. Park, H.-S.; Agarwal, A.; Kotov, N. A.; Lavrentovich, O. D., Controllable side-by-side and end-to-end assembly of Au nanorods by lyotropic chromonic materials. *Langmuir* **2008,** *24* (24), 13833-13837.

69. (a) Huang, H.-C.; Koria, P.; Parker, S. M.; Selby, L.; Megeed, Z.; Rege, K., Optically Responsive Gold Nanorod− Polypeptide Assemblies. *Langmuir* **2008,** *24* (24), 14139-14144; (b) González-Rubio, G.; González-Izquierdo, J.; Bañares, L.; Tardajos, G.; Rivera, A.; Altantzis, T.; Bals, S.; Peña-Rodríguez, O.; Guerrero-Martínez, A.; Liz-Marzán, L. M., Femtosecond laser-controlled tip-to-tip assembly and welding of gold nanorods. *Nano Lett* **2015,** *15* (12), 8282-8288.

70. (a) Asakura, S.; Oosawa, F., Interaction between Particles Suspended in Solutions of Macromolecules. *J Polym Sci* **1958,** *33* (126), 183-192; (b) Wang, T.; Zhuang, J.; Lynch, J.; Chen, O.; Wang, Z.; Wang, X.; LaMontagne, D.; Wu, H.; Wang, Z.; Cao, Y. C., Self-assembled colloidal superparticles from nanorods. *Science* **2012,** *338* (6105), 358-363; (c) Baranov, D.; Fiore, A.; van Huis, M.; Giannini, C.; Falqui, A.; Lafont, U.; Zandbergen, H.; Zanella, M.; Cingolani, R.; Manna, L., Assembly of colloidal semiconductor nanorods in solution by depletion attraction. *Nano Lett* **2010,** *10* (2), 743-749; (d) Talapin, D. V.; Shevchenko, E. V.; Murray, C. B.; Kornowski, A.; Förster, S.; Weller, H., CdSe and CdSe/CdS nanorod solids. *J Am Chem Soc* **2004,** *126* (40), 12984-12988.

71. (a) Taniguchi, Y.; Takishita, T.; Kawai, T.; Nakashima, T., End‐to‐End Self‐Assembly of Semiconductor Nanorods in Water by Using an Amphiphilic Surface Design. *Angewandte Chemie* **2016,** *128* (6), 2123-2126; (b) Kim, D.; Kim, W. D.; Kang, M. S.; Kim, S.-H.; Lee, D. C., Self-organization of nanorods into ultra-long range two-dimensional monolayer end-to-end network. *Nano Lett* **2014,** *15* (1), 714-720.

72. (a) He, L.; Zhang, L.; Ye, Y.; Liang, H., Solvent-induced self-assembly of polymer-tethered nanorods. *The Journal of Physical Chemistry B* **2010,** *114* (21), 7189-7200; (b) Liu, K.; Zhao, N.; Kumacheva, E., Self-assembly of inorganic nanorods. *Chemical Society Reviews* **2011,** *40* (2), 656-671; (c) Zhuang, J.; Shaller, A. D.; Lynch, J.; Wu, H.; Chen, O.; Li, A. D.; Cao, Y. C., Cylindrical superparticles from semiconductor nanorods. *J Am Chem Soc* **2009,** *131* (17), 6084-6085.
73. Ye, X. C.; Zhu, C. H.; Ercius, P.; Raja, S. N.; He, B.; Jones, M. R.; Hauwiller, M. R.; Liu, Y.; Xu, T.; Alivisatos, A. P., Structural diversity in binary superlattices self-assembled from polymer-grafted nanocrystals. *Nature Communications* **2015,** *6*.
74. (a) Zhang, Z.; Horsch, M. A.; Lamm, M. H.; Glotzer, S. C., Tethered nano building blocks: Toward a conceptual framework for nanoparticle self-assembly. *Nano Lett* **2003,** *3* (10), 1341-1346; (b) Marson, R. L.; Nguyen, T. D.; Glotzer, S. C., Rational design of nanomaterials from assembly and reconfigurability of polymer-tethered nanoparticles. *MRS Communications* **2015,** *5* (03), 397-406.
75. He, J.; Liu, Y. J.; Babu, T.; Wei, Z. J.; Nie, Z. H., Self-Assembly of Inorganic Nanoparticle Vesicles and Tubules Driven by Tethered Linear Block Copolymers. *J Am Chem Soc* **2012,** *134* (28), 11342-11345.
76. (a) Horsch, M. A.; Zhang, Z.; Glotzer, S. C., Self-assembly of polymer-tethered nanorods. *Physical review letters* **2005,** *95* (5), 056105; (b) Horsch, M. A.; Zhang, Z.; Glotzer, S. C., Simulation studies of self-assembly of end-tethered nanorods in solution and role of rod aspect ratio and tether length. *The Journal of chemical physics* **2006,** *125* (18), 184903; (c) Iacovella, C. R.; Horsch, M. A.; Glotzer, S. C., Local ordering of polymer-tethered nanospheres and nanorods and the stabilization of the double gyroid phase. *The Journal of chemical physics* **2008,** *129* (4), 044902; (d) Horsch, M. A.; Zhang, Z.; Glotzer, S. C., Self-assembly of end-tethered nanorods in a neat system and role of block fractions and aspect ratio. *Soft Matter* **2010,** *6* (5), 945-954.
77. (a) Horsch, M. A.; Zhang, Z.; Glotzer, S. C., Self-assembly of laterally-tethered nanorods. *Nano Lett* **2006,** *6* (11), 2406-2413; (b) Nguyen, T. D.; Glotzer, S. C., Switchable Helical Structures Formed by the Hierarchical Self‐Assembly of Laterally Tethered Nanorods. *Small* **2009,** *5* (18), 2092-2098; (c) Nguyen, T. D.; Glotzer, S. C., Reconfigurable assemblies of shape-changing nanorods. *Acs Nano* **2010,** *4* (5), 2585-2594.
78. Hu, J. M.; Wu, T.; Zhang, G. Y.; Liu, S. Y., Efficient Synthesis of Single Gold Nanoparticle Hybrid Amphiphilic Triblock Copolymers and Their Controlled Self-Assembly. *Journal of the American Chemical Society* **2012,** *134* (18), 7624-7627.
79. Nie, Z.; Fava, D.; Kumacheva, E.; Zou, S.; Walker, G. C.; Rubinstein, M., Self-assembly of metal–polymer analogues of amphiphilic triblock copolymers. *Nature materials* **2007,** *6* (8), 609-614.
80. (a) Cheng, W. L.; Campolongo, M. J.; Cha, J. J.; Tan, S. J.; Umbach, C. C.; Muller, D. A.; Luo, D., Free-standing nanoparticle superlattice sheets controlled by DNA. *Nature Materials* **2009,** *8* (6), 519-525; (b) Nykypanchuk, D.; Maye, M. M.; van der Lelie, D.; Gang, O., DNA-guided crystallization of colloidal nanoparticles. *Nature* **2008,** *451* (7178), 549-552; (c) Macfarlane, R. J.; Lee, B.; Jones, M. R.; Harris, N.; Schatz, G. C.; Mirkin, C. A., Nanoparticle superlattice engineering with

DNA. *Science* **2011,** *334* (6053), 204-208; (d) Leunissen, M. E.; Dreyfus, R.; Cheong, F. C.; Grier, D. G.; Sha, R.; Seeman, N. C.; Chaikin, P. M., Switchable self-protected attractions in DNA-functionalized colloids. *Nature materials* **2009,** *8* (7), 590-595; (e) Zhang, Y.; Lu, F.; Yager, K. G.; van der Lelie, D.; Gang, O., A general strategy for the DNA-mediated self-assembly of functional nanoparticles into heterogeneous systems. *Nature Nanotechnology* **2013,** *8* (11), 865-872; (f) Wang, Y.; Wang, Y.; Zheng, X.; Ducrot, É.; Yodh, J. S.; Weck, M.; Pine, D. J., Crystallization of DNA-coated colloids. *Nature communications* **2015,** *6*; (g) Zhang, Y.; Pal, S.; Srinivasan, B.; Vo, T.; Kumar, S.; Gang, O., Selective transformations between nanoparticle superlattices via the reprogramming of DNA-mediated interactions. *Nature materials* **2015,** *14* (8), 840-847.

81. Tikhomirov, G.; Hoogland, S.; Lee, P. E.; Fischer, A.; Sargent, E. H.; Kelley, S. O., DNA-based programming of quantum dot valency, self-assembly and luminescence. *Nature Nanotechnology* **2011,** *6* (8), 485-490.

82. Jones, M. R.; Macfarlane, R. J.; Lee, B.; Zhang, J.; Young, K. L.; Senesi, A. J.; Mirkin, C. A., DNA-nanoparticle superlattices formed from anisotropic building blocks. *Nature materials* **2010,** *9* (11), 913-917.

83. Geng, J. L.; Li, K.; Pu, K. Y.; Ding, D.; Liu, B., Conjugated Polymer and Gold Nanoparticle Co-loaded PLGA Nanocomposites with Eccentric Internal Nanostructure for Dual-modal Targeted Cellular Imaging. *Small* **2012,** *8* (15), 2421-2429.

84. Vial, S.; Nykypanchuk, D.; Yager, K. G.; Tkachenko, A. V.; Gang, O., Linear mesostructures in DNA–nanorod self-assembly. *Acs Nano* **2013,** *7* (6), 5437-5445.

85. (a) Tørring, T.; Voigt, N. V.; Nangreave, J.; Yan, H.; Gothelf, K. V., DNA origami: a quantum leap for self-assembly of complex structures. *Chemical Society Reviews* **2011,** *40* (12), 5636-5646; (b) Tian, Y.; Wang, T.; Liu, W.; Xin, H. L.; Li, H.; Ke, Y.; Shih, W. M.; Gang, O., Prescribed nanoparticle cluster architectures and low-dimensional arrays built using octahedral DNA origami frames. *Nature Nanotechnology* **2015,** *10* (7), 637-644; (c) Hung, A. M.; Micheel, C. M.; Bozano, L. D.; Osterbur, L. W.; Wallraff, G. M.; Cha, J. N., Large-area spatially ordered arrays of gold nanoparticles directed by lithographically confined DNA origami. *Nature Nanotechnology* **2010,** *5* (2), 121-126; (d) Wang, Z. G.; Ding, B. Q., Engineering DNA Self-Assemblies as Templates for Functional Nanostructures. *Accounts of Chemical Research* **2014,** *47* (6), 1654-1662.

86. (a) Lan, X.; Chen, Z.; Dai, G.; Lu, X.; Ni, W.; Wang, Q., Bifacial DNA origami-directed discrete, three-dimensional, anisotropic plasmonic nanoarchitectures with tailored optical chirality. *J Am Chem Soc* **2013,** *135* (31), 11441-11444; (b) Shen, C.; Lan, X.; Lu, X.; Ni, W.; Wang, Q., Tuning the structural asymmetries of three-dimensional gold nanorod assemblies. *Chemical Communications* **2015,** *51* (71), 13627-13629; (c) Rao, C.; Wang, Z.-G.; Li, N.; Zhang, W.; Xu, X.; Ding, B., Tunable optical activity of plasmonic dimers assembled by DNA origami. *Nanoscale* **2015,** *7* (20), 9147-9152; (d) Schreiber, R.; Luong, N.; Fan, Z.; Kuzyk, A.; Nickels, P. C.; Zhang, T.; Smith, D. M.; Yurke, B.; Kuang, W.; Govorov, A. O., Chiral plasmonic DNA nanostructures with switchable circular dichroism. *Nature communications* **2013,** *4*; (e) Pinheiro, A. V.; Han, D. R.; Shih, W. M.; Yan, H.,

Challenges and opportunities for structural DNA nanotechnology. *Nature Nanotechnology* **2011,** *6* (12), 763-772.
87. Kuzyk, A.; Schreiber, R.; Fan, Z. Y.; Pardatscher, G.; Roller, E. M.; Hogele, A.; Simmel, F. C.; Govorov, A. O.; Liedl, T., DNA-based self-assembly of chiral plasmonic nanostructures with tailored optical response. *Nature* **2012,** *483* (7389), 311-314.
88. (a) Jiang, Q.; Shi, Y.; Zhang, Q.; Li, N.; Zhan, P.; Song, L.; Dai, L.; Tian, J.; Du, Y.; Cheng, Z., A Self‐Assembled DNA Origami‐Gold Nanorod Complex for Cancer Theranostics. *Small* **2015,** *11* (38), 5134-5141; (b) Du, Y.; Jiang, Q.; Beziere, N.; Song, L.; Zhang, Q.; Peng, D.; Chi, C.; Yang, X.; Guo, H.; Diot, G., DNA‐Nanostructure–Gold‐Nanorod Hybrids for Enhanced In Vivo Optoacoustic Imaging and Photothermal Therapy. *Adv Mater* **2016**.
89. Caswell, K.; Wilson, J. N.; Bunz, U. H.; Murphy, C. J., Preferential end-to-end assembly of gold nanorods by biotin-streptavidin connectors. *J Am Chem Soc* **2003,** *125* (46), 13914-13915.
90. Wang, L.; Zhu, Y.; Xu, L.; Chen, W.; Kuang, H.; Liu, L.; Agarwal, A.; Xu, C.; Kotov, N. A., Side‐by‐Side and End‐to‐End Gold Nanorod Assemblies for Environmental Toxin Sensing. *Angewandte Chemie International Edition* **2010,** *49* (32), 5472-5475.
91. Salant, A.; Amitay-Sadovsky, E.; Banin, U., Directed self-assembly of gold-tipped CdSe nanorods. *J Am Chem Soc* **2006,** *128* (31), 10006-10007.
92. Jain, P. K.; Huang, X.; El-Sayed, I. H.; El-Sayad, M. A., Review of some interesting surface plasmon resonance-enhanced properties of noble metal nanoparticles and their applications to biosystems. *Plasmonics* **2007,** *2* (3), 107-118.
93. Jain, P. K.; Huang, W.; El-Sayed, M. A., On the universal scaling behavior of the distance decay of plasmon coupling in metal nanoparticle pairs: a plasmon ruler equation. *Nano Lett* **2007,** *7* (7), 2080-2088.
94. Piner, R. D.; Zhu, J.; Xu, F.; Hong, S. H.; Mirkin, C. A., "Dip-pen" nanolithography. *Science* **1999,** *283* (5402), 661-663.
95. (a) Wang, Y. F.; Wang, Y.; Breed, D. R.; Manoharan, V. N.; Feng, L.; Hollingsworth, A. D.; Weck, M.; Pine, D. J., Colloids with valence and specific directional bonding. *Nature* **2012,** *491* (7422), 51-U61; (b) Park, S. Y.; Lytton-Jean, A. K. R.; Lee, B.; Weigand, S.; Schatz, G. C.; Mirkin, C. A., DNA-programmable nanoparticle crystallization. *Nature* **2008,** *451* (7178), 553-556.
96. Park, J.; An, K. J.; Hwang, Y. S.; Park, J. G.; Noh, H. J.; Kim, J. Y.; Park, J. H.; Hwang, N. M.; Hyeon, T., Ultra-large-scale syntheses of monodisperse nanocrystals. *Nature Materials* **2004,** *3* (12), 891-895.
97. Li, H. S.; Xia, H. B.; Ding, W. C.; Li, Y. J.; Shi, Q. R.; Wang, D. Y.; Tao, X. T., Synthesis of Monodisperse, Quasi-Spherical Silver Nanoparticles with Sizes Defined by the Nature of Silver Precursors. *Langmuir* **2014,** *30* (9), 2498-2504.
98. Sun, Y. G.; Xia, Y. N., Large-scale synthesis of uniform silver nanowires through a soft, self-seeding, polyol process. *Adv Mater* **2002,** *14* (11), 833-837.
99. (a) Dukes, D.; Li, Y.; Lewis, S.; Benicewicz, B.; Schadler, L.; Kumar, S. K., Conformational Transitions of Spherical Polymer Brushes: Synthesis, Characterization, and Theory. *Macromolecules* **2010,** *43* (3), 1564-1570; (b) Ohno, K.; Morinaga, T.; Takeno, S.; Tsujii, Y.; Fukuda, T., Suspensions of silica particles

grafted with concentrated polymer brush: Effects of graft chain length on brush layer thickness and colloidal crystallization. *Macromolecules* **2007,** *40* (25), 9143-9150.
100. (a) Sardar, R.; Heap, T. B.; Shumaker-Parry, J. S., Versatile Solid Phase Synthesis of Gold Nanoparticle Dimers Using an Asymmetric Functionalization Approach. *J Am Chem Soc* **2007,** *129* (17), 5356-5357; (b) Wang, X.; Li, G.; Chen, T.; Yang, M.; Zhang, Z.; Wu, T.; Chen, H., Polymer-Encapsulated Gold-Nanoparticle Dimers: Facile Preparation and Catalytical Application in Guided Growth of Dimeric ZnO-Nanowires. *Nano Lett* **2008,** *8* (9), 2643-2647; (c) Thacker, V. V.; Herrmann, L. O.; Sigle, D. O.; Zhang, T.; Liedl, T.; Baumberg, J. J.; Keyser, U. F., DNA origami based assembly of gold nanoparticle dimers for surface-enhanced Raman scattering. *Nature Communications* **2014,** *5*, 3448.
101. (a) Alegret, J.; Rindzevicius, T.; Pakizeh, T.; Alaverdyan, Y.; Gunnarsson, L.; Kall, M., Plasmonic properties of silver trimers with trigonal symmetry fabricated by electron-beam lithography. *J Phys Chem C* **2008,** *112* (37), 14313-14317; (b) Roller, E.-M.; Besteiro, L. V.; Pupp, C.; Khorashad, L. K.; Govorov, A. O.; Liedl, T., Hotspot-mediated non-dissipative and ultrafast plasmon passage. *Nature Physics* **2017,** *13*, 761.
102. Urzhumov, Y. A.; Shvets, G.; Fan, J.; Capasso, F.; Brandl, D.; Nordlander, P., Plasmonic nanoclusters: a path towards negative-index metafluids. *Opt Express* **2007,** *15* (21), 14129-14145.
103. Studart, A. R., Towards High-Performance Bioinspired Composites. *Adv Mater* **2012,** *24* (37), 5024-5044.
104. Groschel, A. H.; Walther, A.; Lobling, T. I.; Schacher, F. H.; Schmalz, H.; Muller, A. H. E., Guided hierarchical co-assembly of soft patchy nanoparticles. *Nature* **2013,** *503* (7475), 247-+.
105. Groot, R. D.; Warren, P. B., Dissipative particle dynamics: Bridging the gap between atomistic and mesoscopic simulation. *J Chem Phys* **1997,** *107* (11), 4423-4435.
106. Espanol, P.; Warren, P., Statistical-Mechanics of Dissipative Particle Dynamics. *Europhys Lett* **1995,** *30* (4), 191-196.
107. Nguyen, T. D.; Phillips, C. L.; Anderson, J. A.; Glotzer, S. C., Rigid body constraints realized in massively-parallel molecular dynamics on graphics processing units. *Comput Phys Commun* **2011,** *182* (11), 2307-2313.
108. (a) Zhu, Y. L.; Liu, H.; Li, Z. W.; Qian, H. J.; Milano, G.; Lu, Z. Y., GALAMOST: GPU-accelerated large-scale molecular simulation toolkit. *Journal of Computational Chemistry* **2013,** *34* (25), 2197-2211; (b) Yang, S. C.; Wang, Y. L.; Jiao, G. S.; Qian, H. J.; Lu, Z. Y., Accelerating electrostatic interaction calculations with graphical processing units based on new developments of ewald method using non-uniform fast fourier transform. *Journal of Computational Chemistry* **2016,** *37* (3), 378-387.
109. Liu, Y. J.; Li, Y. C.; He, J.; Duelge, K. J.; Lu, Z. Y.; Nie, Z. H., Entropy-Driven Pattern Formation of Hybrid Vesicular Assemblies Made from Molecular and Nanoparticle Amphiphiles. *Journal of the American Chemical Society* **2014,** *136* (6), 2602-2610.

110. Murphy, C. J.; San, T. K.; Gole, A. M.; Orendorff, C. J.; Gao, J. X.; Gou, L.; Hunyadi, S. E.; Li, T., Anisotropic metal nanoparticles: Synthesis, assembly, and optical applications. *J Phys Chem B* **2005,** *109* (29), 13857-13870.
111. Walther, A.; Muller, A. H. E., Janus Particles: Synthesis, Self-Assembly, Physical Properties, and Applications. *Chemical Reviews* **2013,** *113* (7), 5194-5261.
112. (a) Luzinov, I.; Minko, S.; Tsukruk, V. V., Responsive brush layers: from tailored gradients to reversibly assembled nanoparticles. *Soft Matter* **2008,** *4* (4), 714-725; (b) Zhuang, J. M.; Gordon, M. R.; Ventura, J.; Li, L. Y.; Thayumanavan, S., Multi-stimuli responsive macromolecules and their assemblies. *Chemical Society Reviews* **2013,** *42* (17), 7421-7435.
113. Motornov, M.; Roiter, Y.; Tokarev, I.; Minko, S., Stimuli-responsive nanoparticles, nanogels and capsules for integrated multifunctional intelligent systems. *Prog Polym Sci* **2010,** *35* (1-2), 174-211.
114. Stuart, M. A. C.; Huck, W. T. S.; Genzer, J.; Muller, M.; Ober, C.; Stamm, M.; Sukhorukov, G. B.; Szleifer, I.; Tsukruk, V. V.; Urban, M.; Winnik, F.; Zauscher, S.; Luzinov, I.; Minko, S., Emerging applications of stimuli-responsive polymer materials. *Nature Materials* **2010,** *9* (2), 101-113.
115. (a) She, W. C.; Luo, K.; Zhang, C. Y.; Wang, G.; Geng, Y. Y.; Li, L.; He, B.; Gu, Z. W., The potential of self-assembled, pH-responsive nanoparticles of mPEGylated peptide dendron-doxorubicin conjugates for cancer therapy. *Biomaterials* **2013,** *34* (5), 1613-1623; (b) Isojima, T.; Lattuada, M.; Vander Sande, J. B.; Hatton, T. A., Reversible clustering of pH- and temperature-responsive Janus magnetic nanoparticles. *Acs Nano* **2008,** *2* (9), 1799-1806.
116. Song, J. B.; Zhou, J. J.; Duan, H. W., Self-Assembled Plasmonic Vesicles of SERS-Encoded Amphiphilic Gold Nanoparticles for Cancer Cell Targeting and Traceable Intracellular Drug Delivery. *J Am Chem Soc* **2012,** *134* (32), 13458-13469.